CRANFIELD UNIVERSITY

GARETH FRAZER

DECEPTION JAMMING AGAINST ANTI-SHIP MISSILES WHICH USE DOPPLER BEAM SHARPENING MODES

SCHOOL OF CRANFIELD DEFENCE AND SECURITY
Centre For Electronic Warfare, Information and Cyber

PhD
Academic Year: 2016–2020

Supervisor: Dr Alessio Balleri
February 2020

CRANFIELD UNIVERSITY

SCHOOL OF CRANFIELD DEFENCE AND SECURITY
Centre For Electronic Warfare, Information and Cyber

PhD

Academic Year: 2016–2020

GARETH FRAZER

Deception Jamming Against Anti-Ship Missiles Which Use Doppler Beam Sharpening Modes

Supervisor: Dr Alessio Balleri
February 2020

This thesis is submitted in partial fulfilment of the requirements for the degree of PhD.

Abstract

Missile seekers are becoming increasingly more capable of using Doppler Beam Sharpening (DBS) modes as part of the homing cycle, which requires new countermeasures against this mode. One type of countermeasure, is to create false targets within the seeker DBS image. This thesis presents two implementation methods to insert false targets into DBS images. Both methods are used to create false targets at a precise location within a seeker DBS image, but are implemented in different ways. The first method proposes repeat jamming with a time-varying delay, whilst the second proposes a fixed delay and adding a specific Doppler shift to received waveforms. The effects of tracking errors on the position of the false target are analysed, both analytically and with simulations and used to assess the practical implementation of the jamming scheme. An experimental DBS system was built to test the effectiveness of the jamming scheme against a platform moving in steps and assess errors caused by incorrectly estimating the seeker trajectory. The overall result of the thesis is that using the derived jamming methods, false targets can be created at specific locations in the DBS image of the victim radar, providing the trajectory of the victim radar is known.

Contents

List of Figures

List of Tables

List of Abbreviations

AESA	Active Electronically Scanned Array
ASM	Anti-Ship Missile
BBC	British Broadcasting Corporation
CEJ	Cross-Eye Jamming
CIWS	Close-In Weapon System
COTS	Commercial Off-The-Shelf
DBS	Doppler Beam Sharpening
DRFM	Digital Radio Frequency Memory
ECM	Electronic Counter Measures
ECCM	Electronic Counter Counter Measures
HMS	Her/His Majesty's Ship
HMT	Her/His Majesty's Tug
HOJ	Home-On-Jam
ISA	International Standard Atmosphere
LDEW	Laser Directed Energy Weapons
LFM	Linear Frequency Modulation
PLL	Phase Locked Loop
PRI	Pulse Repetition Interval
PRF	Pulse Repetition Frequency
PSD	Power Spectral Density
PWM	Pulse Width Modulation

RADAR	RAdio Detection And Ranging
RAF	Royal Air Force
RCS	Radar Cross Section
RF	Radio Frequency
SONAR	SOund NAvigation And Ranging
SAR	Synthetic Aperture Radar
SDR	Software Defined Radio
SNR	Signal to Noise Ratio
US	United States
USRP	Universal Software Radio Peripheral
USS	United States Ship
VNA	Vector Network Analyser
WGN	White Gaussian Noise
WSS	Wide-Sense Stationary
WWII	World War Two

List of Symbols

α	Jammer Modifier
α_ε	Jammer Modifier With Errors
A_e	Antenna Aperture
B	Bandwidth
β	Phase Term of Jammer Position
β_j	Phase Term of False Target Position
c	Speed of Light
d	Array Element Spacing
δ_x	Additional Cross-Range Position
δ_R	Additional Down-Range Position
Δ_{CR}	Cross-Range Resolution
$\Delta\theta$	Maximum Steering Angle
Δ_x	Step Distance
f_c	Carrier Frequency
f_d	Doppler Shift
F_n	Radar Noise Figure
F_s	Sample Rate
G	Gain of Antenna

γ	Chirp Rate
γ_J	Jammer Gain Factor
γ_R	Attenuation Factor
$\hat{\gamma}_R$	Attenuation Factor & Phase Terms
h	Height
I_{R_L}	Current Across Noiseless Resistor
I_{TH}	Current Across Thévenin's Circuit
k	Boltzmann's Constant
λ	Wavelength
M	Number of Pulses
μ_n	Mean of Random Process
N_0	Noise Power Spectral Density
P_n	Noise Power
P_r	Received Power
P_t	Transmitted Power
R	Range
R_ε	Down-Range Error Factor
R_L	Noiseless Resistor
R_n	Noisy Resistor
R_0	Jammer Position in Down-Range
σ	Radar Cross Section (RCS)
${\sigma_n}^2$	Noise Variance
s_{ro}	Received Signal Sample
t	Time
T	Effective Temperature
T_0	Reference Temperature
τ	Pulse Width
τ_j	Jammer Delay Time

T_{dwell}	Dwell Time
τ_d	Echo Delay Time
θ_{3dB}	3 dB Beamwidth
V	Velocity
V_ε	Velocity Error Factor
V_{R_L}	Voltage Across Noiseless Resistor
V_{TH}	Voltage Across Thévenin's Circuit
w	Width
$\hat{x}$	Cross-Range Position of False Target
x_0	Jammer Position in Cross-Range
x_ε	Cross-Range Error Factor

Acknowledgements

First and foremost I would like to thank my supervisor, Dr. Alessio Balleri for his unyielding support and guidance during the PhD studies. Throughout the PhD studies, he has consistently gone above and beyond his statutory duties as a PhD supervisor and I am incredibly grateful for all of his dedication and advice on a wide-range of topics from technical to personal. I could not have asked for a better supervisor and mentor.

I would also like to express my thanks to my supervisory committee: Prof. Mark Richardson, Prof. Nabil Aouf, Dr. Ata Khalid and Dr. David James for their insightful questions and constructive feedback during the reviews throughout the PhD studies. I am also grateful to my examiners Prof. Hugh Griffiths and Dr. Daniel Andre for reviewing this thesis.

My sincere thanks goes to George S. Jacob from Defence Science Technology Laboratory (Dstl) for suggesting the PhD topic in the first place and for his continued support and guidance over the last four years. I would also like to thank the Above Water Maritime Survivability Team in Dstl for an interesting and challenging PhD placement and for their support during the PhD studies. Special thanks goes to the Engineering Physical Sciences Research Council (EPSRC) and Dstl for funding this PhD research.

I would like to thank my family for their love and support over the last four years. In particular, my father and grandparents who encouraged and nurtured my fondness of engineering from an early age. Finally, my wonderful wife, Cheryl, has been the bedrock of stability upon which I have been able to pursue the PhD award and her sacrifices made it possible to research my passions and complete this thesis. For this, amongst many things, I am eternally grateful.

Chapter 1

Introduction

In the context of evolution and natural selection, deception is often an advantageous trait for survival. Biologically speaking, deception is to falsely communicate information in a way that tends to benefit the communicator [Mitchell & Thompson, 1986]. This deception could be in the form of mimicry, where a species tries to appear like another species to lure prey or avoid predators. For example, the North American Monarch Butterfly is toxic and has a colourful warning which birds recognise as it being inedible. However, the Viceroy Butterfly is edible to birds, but displays the same warnings as the North American Butterfly to avoid predation [Bond & Robinson, 1988].

Deception could be in the form of false alarm calls to gain food or access to the opposite sex for mating. For example, the Fork-Tailed Drongo (a bird found south of the Sahara Desert) acts as a sentinel for Meerkats to help them avoid predators. However, the Drongo also issues false-alarm calls when the meerkats find food which causes them to abandon their catch to avoid predators. The bird then swoops in and steals the meal [Flower, 2011].

Deception in everyday human life is common and used for a variety of reasons. When looking for a sexual partner, humans often change their behaviour to try to appear more desirable to the person they are interested in. For example, humans might try to appear more socially outgoing , fun, better groomed, more fashionable, or perhaps try to make anatomical features appear more desirable. Deception in sport is actively encouraged and

often a vital part of winning, such as feigning to go one direction but actually going another, performing a 'dummy' pass in ball games like football or rugby, etc.

Humans might use deception to throw surprise parties for friends and loved ones or hide the identity of a gift to maintain surprise for the recipient. Deception is also a vital part of nefarious activities such as committing crimes and trying to evade arrest by law enforcers, by removing evidence or links to the perpetrator. Regardless of whether there was conscious intent to deceive or if the deception was selected due to a unique advantage over competitors, it is a trait that can often mean the difference between life and death to many creatures found on Earth.

It is widely known that bats use SONAR (SOund NAvigation and Ranging) to avoid obstacles and hunt for food. Their target recognition in clutterous environments is so sophisticated, that humans have studied their echolocation calls with a view to improve our own wireless systems [Balleri et al., 2009]. However, by relying on this method for navigation and hunting, bats have been made vulnerable to jamming from their prey. Some species of Tiger Moth have developed tymbal organs, which can be used to produce a series of clicks capable of decreasing the effectiveness of the bat's hunting [Corcoran et al., 2010]. Nature and the process of natural selection have shown that deception is a necessary part of organic life, especially in conflict. For humans, conflict can be a daily occurrence, lying within a spectrum of severity ranging from minor traffic violations to nuclear war. In order to win any war, deception is a fundamental necessity.

When deception of any form is used so commonly in nature and humans, it is inevitable that deception would also be used in war. So much so that if a side did not use deception of any forms, they would most likely lose the war they were fighting. To quote the famous general, Sun Tzu, 'All warfare is based on deception' [Sunzi & Clavell, 1981]. Deception in battle has been used ever since battles were fought. Famous examples of this being the Trojan horse in The Trojan War around 1200 BC, or Operation Fortitude which the Allies used in World War II. Operation Fortitude was a large scale plan to try to make the Germans think the Normandy invasions were going to happen at Norway (Fortitude

North) and Pas de Calais (Fortitude South) instead of Normandy [Barbier, 2007].

The ability to communicate with each other during war is a vital commodity and so it is unsurprising that wireless communications were used in war just a few years after being experimentally tested for the first time. The Italian engineer Gugliemo Marconi (1874 - 1937) is considered by many to be the pioneer of radio communications and it was his designs that were first used in war. After successfully proving the principle of wireless communication, he moved to England in 1896. In the same year, he demonstrated his system on the Salisbury plains in Wiltshire [Corazza, 1998]. Then in 1897, he transmitted and received messages between Lavernock, Vale of Glammorgan (Wales) and the Isle of Flatholm (Bristol Channel), which is approximately 15 km in distance. He was supported by Welshman Sir William Preece, Chief Engineer for the Post Office, who enabled Marconi's experiments by securing funding and giving Marconi access to the Post Office's Equipment [Institution of Civil Engineers (Great Britain), 1914]. Once he had the equipment, Marconi moved quickly and in 1898 he fitted his communication systems to a number of ships including the 'Osborne', which Queen Victoria used to communicate with the Prince of Wales from Osborne House in the Isle of Wight. This gave rise to possibly the first radio SOS distress signal in 1899 which was transmitted by the lightship 'East Goodwin' when she collided with a steamboat in fog [Corazza, 1998].

During 1899, the Royal Navy successfully demonstrated radio communication at a maximum range of approximately 136 km aboard the HMS Alexandra, HMS Europa and HMS Juno, with Marconi himself aboard the Juno [Austin, 1995]. It was after these successful tests that the British decided to send radio sets and six engineers from Marconi's company to help fight the Boer War which was the first war to use wireless communications [Austin, 1995]. The military benefits of wireless beyond visual range communication was revolutionary and the British military used this technology in war just three years after Marconi demonstrated a basic prototype.

Since radio communication conception, the concept of electronic warfare was created. One of the first recorded cases of deliberate radio jamming was in 1901, where an Ameri-

can telecomms company deliberately jammed their competitor's broadcast transmissions, so only they could report the status of the Americas Cup Yacht race instead of the competition [R. Schroer, 2003]. This refers back to the previous points about the use of deception in nature and by humans. In order to gain an advantage for survival, which in this case was for monetary gain, deception was used to ensure victory for the telecomms company in terms of gaining the reporting rights to the race.

Radar is an Acronym which stands for RAdio Detection And Ranging and the term was coined by the US Navy in 1940 [Gebhard, 1979]. The first radar ever built was the 'Telemobiloskop', which was developed by Christian Hülsmeyer in 1903 and publicly demonstrated in 1904 in Köln, Germany [Griffiths et al., 2019]. The demonstration successfully detected a barge located several hundred metres in range. However, the device was much more capable than that and also successfully detected ships at a range of 3000 m, with a wavelength around 40-50 cm [Swords, 1986] on a different test. This working prototype gained no further funding and [Griffiths et al., 2019] postulated that this may be due to the advances in radiotelegraphy by Marconi or partially due a shipping industry recession. Only after after a speech by Marconi at the American Institute of Electrical Engineers in 1922, was the idea of detecting objects by transmitting electromagnetic waves revisited [James, 1989].

Prior to the start of World War II in 1935, the German Luftwaffe had thousands of state-of-the-art aircraft which dwarfed the Royal Air Force (RAF) both in terms of size and capability. This led to the first meeting of the 'Committee for the Scientific Survey of Air Defence' which was chaired by Sir Henry Tizard. The committee tasked Sir Robert Watson-Watt to research if it was possible to incapacitate approaching German pilots or render the aircraft useless before they took off. Early in 1935, Watson-Watt produced a memorandum dismissing the idea of a 'Death Ray'. His reckoning was that to heat a 75 kg man with a cross-sectional area of 1 m^2, it would require a transmitter with 5 GW of power and was therefore not a feasible option [Austin, 1999]. To give a scale of this power, Hinkley point C, a modern nuclear power station scheduled to be operational in

2025, will have a capacity of 3.2 GW [Department for Business, 2018].

This research gave the idea that the highly reflective metallic aircraft could be used to reflect sufficient incident energy back towards a receiver to detect it. This led to Watson-Watt's second memorandum 'Detection and Location of Aircraft by Radio Methods', which was delivered to the Air Ministry on 12th February 1935 [Brown, 1994] and gave birth to Britain's first radar system.

The committee moved quickly and on the 26th February 1935, the famous 'Daventry Experiment' was undertaken. This was a bistatic radar system, using the British Broadcasting Corporation (BBC) transmitter tower as the transmitter of opportunity and an aircraft flying back and fourth as the target [Griffiths, 2016]. The first large-scale radar in Britain was the 'Chain Home' system, which was built by the British and became operational in 1939 [Martin, 1988]. Chain Home was a network of air defence radars scattered across the South and East of the English coastline and played a vital role in securing victory for the Royal Air Force in the Battle of Britain. Such is the nature of warfare, the Germans developed a bistatic radar, 'Klein Heidelberg', which used the Chain Home system as its transmitter [Griffiths, 2017]. Radar became such a vital part of the war that the British launched 'The Bruneval Raid' (Operation BITNG), to document and capture as much of a German radar as possible [Griffiths, 2014]. The radar in question was a Würzburg type which was primarily used as an air defence radar. The daring raid was conducted as the Allies needed to know more about German radar technology and to gain tactical insights which could be exploited, through what we now refer to as Electronic Counter Measures (ECM). Electronic Warfare was used extensively on D-Day (6th June 1944), to try to deceive the Germans into believing the landings were not going to the five intended beaches of Normandy (Omaha, Utah, Gold, Juno and Sword) but instead to Pas de Calais and Cap d'Antifer [Griffiths, 2015]. This was achieved using a combination of ingenious techniques. Examples being the use of using Filbert Balloons (which had large corner reflectors inside them to give the Radar Cross Section (RCS) of a 5000 Tonne ship), 'Moonshine' repeater jammers, chaff, stereo systems (to provide all the right sounds of

an incoming fleet) and attacks on specific German radar stations. The Moonshine jammer was a repeater jammer that downconverted the incoming signal to an intermediate frequency and passed the signal through a liquid acoustic delay cell [Griffiths, 2015]. The signals were then converted to acoustic and passed through an array of wires (to give the desired range delays) before conversion back to an electrical signal, upconversion to RF and then re-transmission.

Due to the World War II effort, radar was rapidly improved from all sides and cemented the use of radar in modern military and civilian tracking and guidance systems. As well as the significant radar development, WWII also saw the world's first radio-control guided missiles used in combat. Nikola Tesla's radio controlled vessel, which was demonstrated in New York, 1898, [Marincic & Budimir, 2008] paved the way for remotely controlled machines and this concept inevitably became a vital asset to militaries around the world. In July 1943, the Allies launched Operation 'Husky' which was an invasion of Sicily, Italy. During this invasion, the Germans successfully used Henschel HS 293 missiles to sink two ships, the 'Duchess of York' and the 'California'. The Henshel HS 293 was a radio-controlled jet-powered missile [Saxon, 2003], which required the weapon operators to maintain visual contact during the missile's entire flight time.

The radio-control system for the HS 293 was the Kehl/ Strassbourg system. It was designed to operate on any one of 18 pre-determined frequencies, separated by 100 kHz bands, between a carrier frequency of 48-50 MHz [Piccirillo, 1997]. The separation of operating frequencies enabled up to 18 missiles to be launched at the same time, but also reduced the effectiveness of the Allied jammers. The multiple frequencies were effective at defeating jammers on at least one occasion. On 26th November 1943, the Germans sank the British transport ship HMT Rohna. The jammers on board US destroyers USS Jones and USS Davies were unable to cope with the many different operating frequencies from the salvo of missiles launched, resulting in the jamming being unsuccessful [Piccirillo, 1997]. Since guided missiles debuted in World War II, they have been in continuous development and there is now a large suite of different types and guidance systems in use.

There are now many types of active missiles which can acquire targets using their own sensors, or semi-active which use a combination of the seeker sensor and another transmitter, to guide the missile to the target. There are also an increasing number of missile guidance systems which use infrared seekers to acquire and navigate to targets. All military systems in use inevitably require countermeasure development against the specific technique in question and this is not just limited to radar systems.

The defence company MBDA Ltd are currently testing a new infrared anti-ship missile 'Sea Venom' [MBDA, 2018]. Whilst this is a separate event and coincidental timing, the United States awarded a $3.1Billion infrared countermeasures contract to Northrop Grumman at a similar time [Northrop Grumman Corporation, 2018]. Regardless of the sensor a missile uses, militaries across the world will inevitably develop counter measures to missile threats. This created the field of Electronic Counter Measures (ECM) which in turn has given rise to the field of Electronic Counter Counter Measures (ECCM), to counter the counter measures. This shows there is an ongoing game of 'Cat and Mouse' for seeker system designers and ECM designers.

ECM is used with many types of systems, such as infrared, sonar and radar, but this thesis focuses on ECM specifically against a radar seeker system. Radar seeker jamming can be defined as transmitting electromagnetic radiation which in some way, reduces the ability of the seeker to guide the missile to its intended target. This can be achieved using a variety of different methods which could be used in unison or separately. The jamming waveform can be transmitted to deny the seeker the opportunity to detect a target by transmitting 'noisy' waveforms, which reduces the ability of the seeker to distinguish between background noise and valid echoes from targets. A jamming waveform can also be used to create false targets, reducing the probability of the seeker hitting the correct target. Alternatively, the waveform can be used to change the shape of an existing target so the seeker target recognition algorithm ignores it. There are many types of missile seeker, both in-service and in development by the British armed forces and defence industries. Advanced missiles can switch between different radar modes during the homing

cycles. Jamming some of these modes such as Monopulse radars whilst the seeker does an area search has been intensely studied. With increasingly superior hardware and target recognition algorithms, missile seekers are now capable of utilising radar imaging modes such as Synthetic Aperture Radar (SAR) and Doppler Beam Sharpening (DBS) which is a primitive, but time and processing efficient form of SAR [Stansfield, 2016].

Doppler Beam Sharpening (DBS) is a crude radar imaging technique that uses the relative motion between the target and the platform, to resolve targets or dominant scatterers within the same target in cross-range by exploiting the Doppler effect [Stimson et al., 2014]. Whilst it is quite an old technique (invented in 1951 by Carl Wiley [Wiley, 1985]) it is now being used in missiles [Stansfield, 2016], naval radars and in the automotive industry [Daniel et al., 2018]. Missile seekers benefit from using DBS, as it sufficiently improves azimuth resolution without being computationally expensive like Synthetic Aperture Radars (SAR). DBS images are typically much faster to obtain than SAR images and easier to analyse, whereas SAR tends to have a vastly superior azimuth resolution and focus. As a generic example, DBS can be performed with a dwell time in the order of tens of milliseconds, whereas SAR is in the order of whole seconds [Stimson et al., 2014]. DBS is sometimes referred to as an 'unfocused' SAR mode [Lacomme et al., 2001] and in this thesis, SAR is assumed to be focused. DBS uses short dwell times, resulting in approximations which enable non-linear Doppler terms to be neglected. This will be presented in Chapter 3. The result of these approximations is that for SAR, the cross-range resolution is independent of range, but for DBS, the cross-range resolution is a function of range.

It will be shown in Chapter 2 that there is a significant gap in the Electronic Counter Measures (ECM) against DBS techniques. Whilst the technique was developed in 1951, there is little if any unclassified literature about jamming such techniques. This thesis investigates how to insert a false target into a DBS image and what the effects and implications are of estimating various aspects of the scenario (e.g waveform, missile trajectory, etc.) incorrectly. This has been achieved by creating novel jamming schemes and testing these schemes through computer simulations and experiments in the laboratory.

1.1 Research Questions

This PhD studies how to jam a missile seeker which uses DBS modes and the effects and implications of not estimating seeker parameters correctly. There are a number of questions to answer and the order of these questions is as follows:

How to insert false targets into a DBS Image?

There is little if any unclassified literature detailing how to insert false targets into a DBS image. Chapter 5 presents an overview on how to insert false targets into a DBS image using repeat jamming when all parameters of the seeker (such as carrier frequency, PRF, bandwidth, velocity, trajectory, etc.) are known.

What are the effects of incorrect estimations of velocity and position?

In a real military scenario, the jammer could have little or no prior knowledge of the victim radar. It therefore must rely on real-time estimations of the victim parameters to effectively jam the seeker to cause a desired effect. Chapter 6 investigates the effects of incorrect parameter estimations on the images that the jammer is trying to interfere with. This is in terms of quality of the false target, location, Signal to Noise Ratio (SNR), etc.

How accurate do estimations need to be?

When the effects and implications of erroneous estimations are known, the next step is to understand which errors have the biggest impact on the desired outcome of the jammed DBS image, which is investigated in Chapter 6. This can help to make better decisions when trading off accuracy for real time speed in designing jamming systems.

What is the probability of the seeker accepting or rejecting a false target?

The work for this PhD award does not assess the probability of a seeker acquiring the correct target in the presence of jamming. Target classification algorithms are often highly

classified which makes them difficult to study, but it is also a field in its own right and therefore beyond the scope of this thesis. This could however be a natural progression of future work. Once a method for creating targets has been achieved and errors analysed, it is then a logical next step to assess how the targets would be perceived by a seeker and if errors in jamming increased or decreased the probability of a seeker accepting the target as valid.

1.2 Thesis Structure & Novel Contributions

CH. 1 - Introduction: This is a general introduction to radar and radar jamming from a historical and philospohical perspective, to give a broader context of electronic warfare and radars in general.

CH. 2 - Literature Survey: This literature survey covers general jamming against tracking radars and research into Digital Radio Frequency Memory (DRFM) jamming systems. The main focus of the survey is inserting false targets into Synthetic Aperture Radar (SAR) and how DBS is being used in civilian and military applications.

CH. 3 - Background Theory: The background theory of how a general purpose radar is presented, as well as basic jamming principles. The chapter then specifically details why DBS is used, how it is used and how to take a DBS image, from first principles.

CH. 4 - Experimental Setup: In order to take DBS images, platform motion is required to create the desired Doppler shifts. A linear rail was constructed to slide an antenna across an aperture, to both take DBS images and jam them. The chapter details how the rail was constructed, tested and validated to take measurements for the thesis. This chapter formed part of the novel contributions of this thesis, as it was main experimental setup for the results obtained in Chapters 5 and 6.

CH. 5 - Inserting False Targets into a DBS Image: The chapter details two methods of implementation to insert false targets into DBS images. The first method proposes repeat jamming with a time-varying delay, the second details how to create false targets at a precise location within a seeker DBS image, by both delaying and adding a Doppler shift to received waveforms. The first method is tested with simulations and the second was tested with both simulations and measurements with the DBS system detailed in Chapter 4.

CH. 6 - Effects of Errors in Trajectory Estimation: Chapter 5 details the required parameters about the seeker trajectory to insert a false target into the seeker DBS image. This chapter describes the effects of tracking errors on the position of the false target. This is analysed analytically, with simulations and with experimental results. The results are used to assess the practical implementation of the second jamming scheme.

CH. 7 General Conclusion and Future Work: Whilst each chapter will be concluded and summarised, this short chapter draws an overall conclusion and details where the thesis stands in the broader context of jamming scenarios. It also details what research the thesis did not cover and what needs to studied to build on the thesis.

1.3 Published Research

1.3.1 Conference Papers

Sensor Signal Processing for Defence 2017

Frazer, G., Balleri, A., and Jacob, G. (2017). "Simulations of Repeat Jamming against Anti-Ship Missile Seekers Which Use Doppler Beam Sharpening Modes". In 2017 Sensor Signal Processing for Defence Conference (SSPD) (pp. 1–5). London: IEEE. [Frazer et al., 2017].

Presented at the 2017 Sensor Signal Processing for Defence Conference (SSPD), London (UK). This paper detailed the first implementation method to create false targets in DBS images and is explained in Section 5.3.1.

IEEE Radar Conference 2019

Frazer, G., Balleri, A., and Jacob, G. S. (2019). "Deception Jamming Against Doppler Beam Sharpening Radars". In 2019 IEEE Radar Conference (Radar- Conf) (pp. 1–6). Boston: IEEE. [Frazer et al., 2019]

Presented at the 2019 IEEE Radar Conference, Boston (USA). This paper detailed the second implementation method to create false targets in DBS images and is explained in Sections 5.3.2 and 5.4.

1.3.2 IEEE Access Journal

G. Frazer, A. Balleri and G. Jacob, "Deception Jamming Against Doppler Beam Sharpening Radars," in IEEE Access, vol. 8, pp. 32792-32801, 2020. [Frazer et al., 2020]

Accepted to the IEEE Access journal in February 2020. This paper detailed a rigourous mathematical detail of the second implementation method to create false target in a DBS Image. The content of the paper can be found in sections 5.3.2, 5.5 and all of Chapter 6.

Chapter 2

Literature Review

2.1 Introduction

This PhD studies jamming novel Radio Frequency (RF) missile seekers which use DBS as part of the homing cycle.

This can be achieved in several ways. One method is noise jamming, which aims to increase the noise power in the victim radar system. If the noise power is sufficiently high enough, the jammer will have denied the victim radar the opportunity to detect any targets through the noise. A jamming waveform can also be used to create multiple false targets to reduce the probability of the seeker hitting the correct target. Alternatively, the waveform can be used to cause angular displacement in the seeker. Angular displacement refers to the jamming waveform causing the seeker to track a target which is in a different location to where it actually is, therefore saving the target from destruction.

This literature survey reviews existing jamming techniques against tracking and imaging radars and applications of DBS to military and civilian scenarios. It will be shown that deception jamming against SAR radars has been studied in part, but there is a distinct gap in the literature investigating how to jam DBS radars.

2.2 Countering a Missile Threat

Hard Kill

Instead of using decoys or electronic warfare to counter the missile threat, navies around the world have the option of physically destroying the missile by shooting at it with missiles (e.g. Sea Viper, Sea Ceptor), projectile weapons (e.g. Phalanx CIWS) or by using Laser Directed Energy Weapons (LDEW) (e.g. UK Dragonfire). Sea Viper (fitted to Type 45 Destroyers) and Sea Ceptor (Type 26 Frigates) are long range anti-air missile systems, designed to destroy incoming high velocity targets. These missiles are examples of systems that the Royal Navy has to defend ships against missile threats but their characteristics are beyond the scope of this thesis. Should a long range kill option fail, the close range ($\approx$2 km) Gatling guns are also effective against incoming threats. Raytheon's Phalanx Close-In Weapon System (CIWS) is a radar controlled Gatling gun which is designed to engage and destroy multiple threats such as missiles, drones, etc [Navy, 2017].

Soft Kill

If hard kill options are not successful or available to a defending ship, decoys offer a soft kill option. Soft kill means that the missile threat is destroyed by allowing it to hit a low value target such as a decoy. Two types of expendable decoys are Lockheed Martin's 'Nulka' and Leonardo's 'BriteCloud'. The Nulka is a ship-launched active decoy that is designed to replicate a ship's Radar Cross Section (RCS) and provide a larger, more appealing target than the platform it is trying to protect [Lockheed Martin, 2017]. Britecloud is a small and lightweight active expendable decoy that is launched from fast jet and fixed winged aircraft. It is a Digital Radio Frequency Memory (DRFM) based jammer, that is used to steer the missile away from the protected platform [LEONARDO, 2017]. With this being an off-board decoy, it removes the problem of 'Home-On-Jam' (HOJ) mode, which on-board jammers are at risk of. HOJ mode means that the jammer has been detected by the seeker and the seeker passively homes onto the jamming signal

instead of actively transmitting its own waveforms to locate the target.

Electronic Countermeasures (ECM)

ECM is a broad term covering both attack and defence but is used primarily to reduce the effectiveness of an enemy's weapon system [Neri, 2001b]. This is not just with RF frequencies as the term ECM covers all other spectrums from SONAR through to infra-red. This thesis is concerned with the ECM method of countering a missile threat, as detailed by the research questions in the previous section.

Manoeuvring

Given enough time, ships can orientate themselves to present the missile seeker with the smallest possible RCS, to help to deny the missile the opportunity to destroy its target. However, as missiles become increasingly faster and more advanced, the feasibility of this option is diminishing. If near the coast, ships can stay close to the coastline or other natural radar clutter providers, to deceive the missile.

Sacrifice

Many naval forces around the globe typically arrange their fleets with high value targets, such as aircraft carriers, being surrounded by lower value targets such as destroyers, frigates and smaller vessels. The idea being that should an incoming missile survive the long and short range defence systems, it might hit a lower value target instead of a high value one. This is similar to a strategy in chess, sacrificing a lower value piece like a knight or a bishop, to protect the queen.

2.3 General Jamming

There are several methods to jam a monopulse radar which is a widely used tracking radar and is employed by many modern missile seekers. Neri [Neri, 2001a] summarises a few methods of anti-monopulse deception jamming techniques such as cross-eye jamming and the use of decoys.

In practice, there are two types of decoy: towed and expendable. The idea behind a towed decoy is similar to that of an air-to-air refuelling aircraft trailing a hose and drogue, except that the beacon is a lot smaller than the drogue and is capable of transmitting waveforms that would attract a missile. Typically, the beacons can either be transmitting RF or infra-red waves to attract either an RF seeker or heat seeking missile. The problem with beaconing systems is that due to the aircraft being ahead of them, they are not effective against oncoming missiles. If the aircraft manoeuvres to give the beaconing system sight of the oncoming missile, the effective RCS of the aircraft could be greatly increased and will therefore give the missile seeker a larger target to lock onto. This can make the beaconing system fairly useless in this situation [Neri, 2001a].

Cross-Eye Jamming (CEJ) aims to create 'worst-case' angular errors in monopulse radars due to glint [Liu et al., 2015]. The problem with cross-eye jamming is that it requires highly accurate estimation and replication of the seeker waveforms. Falk [Falk, 2007] discusses the principles of cross-eye jamming and explains how scattering of the jamming waveform by ocean waves can severely affect the performance of the jammer. The paper also explains that cross-eye can defeat Home-On-Jam (HOJ) mode by creating a false target for the seeker to home onto. This assumes denial jamming has been used prior to using cross-eye to trigger HOJ mode. One of the key points of the paper is that if implemented correctly, cross-eye jamming can be highly effective at creating false targets in the seeker's receiver.

A method of practically implementing cross-eye jamming is retrodirective cross-eye jamming which is demonstrated in [du Plessis, 2012] and an extended analysis of retrodirec-

tive cross-eye jamming is described in [du Plessis et al., 2009]. In order for cross-eye jamming to be implemented, the jammer and therefore the carrying platform needs to be illuminated by the victim radar. This means that there will also be a skin-return caused by the jammer platform alongside the jamming waveforms at the victim receiver which can reduce the performance of cross-eye jamming. A derivation of the cross-eye gain in the presence of skin-returns is presented in [du Plessis, 2019].

Paik et al [Paik et al., 2014, Paik et al., 2015, Paik et al., 2016] have undertaken several studies into noise jamming monopulse radars. They have investigated conditions in which 'break-lock' of phased locked loops (PLL) in the monopulse occurs, when tracking a target. These studies come under the denial jamming spectrum and do not investigate deception jamming by interrupting the PLL. They are essentially investigating how to interrupt the continuous tracking of a target in the angular domain. The PLL is used to track frequency and therefore the angle of the target. A PLL is a negative feedback system consisting of a voltage controlled oscillator, phase detector and loop filter to track frequency. There is a significant amount of literature through books and papers in using broadband and spot noise jamming against many types of radar. Therefore, broadband or narrowband noise jamming will not be investigated further in this thesis.

2.4 Doppler Beam Sharpening

Doppler Beam Sharpening (DBS) is a technique that uses the changing Doppler, caused by relative motion between a platform and a target, to synthetically narrow the main beam of the radar. Figure 2.1 and 2.2 show the basic principle of DBS. The main beam of the radar, will have poor cross-range resolution at a given range. With the movement of the platform, DBS synthetically narrows the beam, improving the cross-range resolution of the radar.

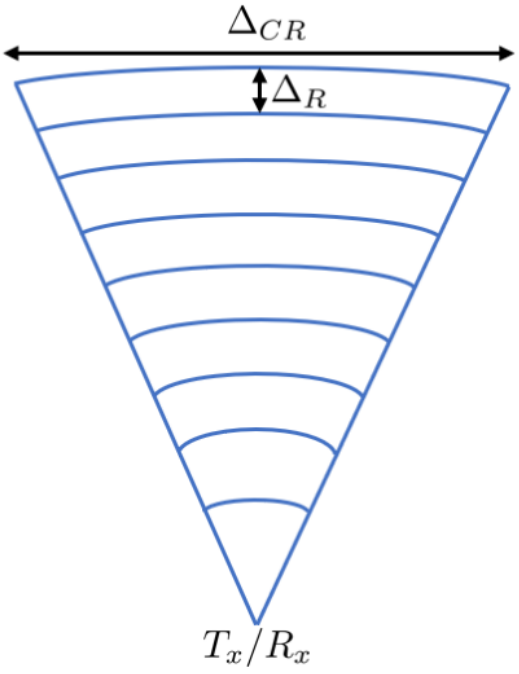

Figure 2.1: Range and Cross-Range Resolution for Real Beam

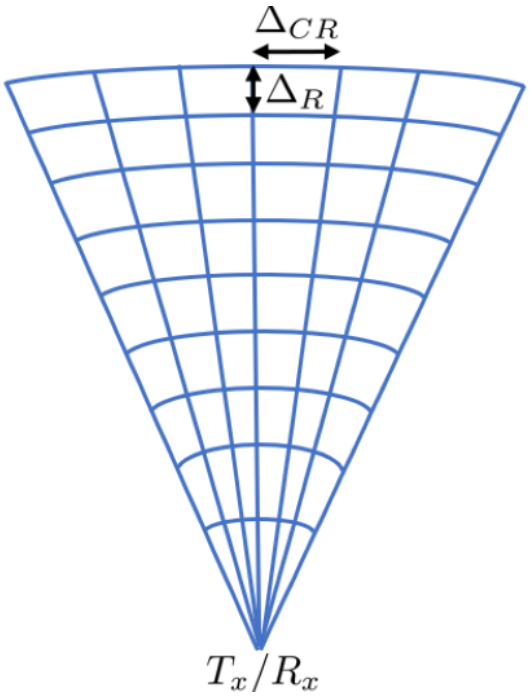

Figure 2.2: Range and Cross-Range Resolution for Doppler Beam Sharpened Beam

Generally, the larger the antenna, the narrower the beamwidth. For a linear phased array antenna to have a cross range resolution of 1m at a range of 20 km when using an operating frequency of 36 GHz, the required antenna diameter would be approximately 83 m based on general equations from [Skolnik, 2008]. This is simply not practical for most applications that require the use of radar. Imaging systems like DBS and Synthetic Aperture Radar (SAR) enable resolution to be drastically increased, when using an antenna that is constrained by the platform it serves.

The principal difference between DBS and SAR is that for SAR, the cross-range resolution is independent of range, but for DBS, the cross-range resolution is a function of range [Neri, 2006]. As DBS uses short dwell times, higher order phase terms can be neglected, resulting in the general theoretical equations for DBS. These approximations will be presented in in Chapter 3, section 3.4.3. Figure 2.3 shows the general principle of how the cross-range resolution for real-beam, DBS and SAR changes with increasing range. Generally, DBS has a better cross-range resolution than the real-beam and in turn, SAR has better cross-range resolution than DBS.

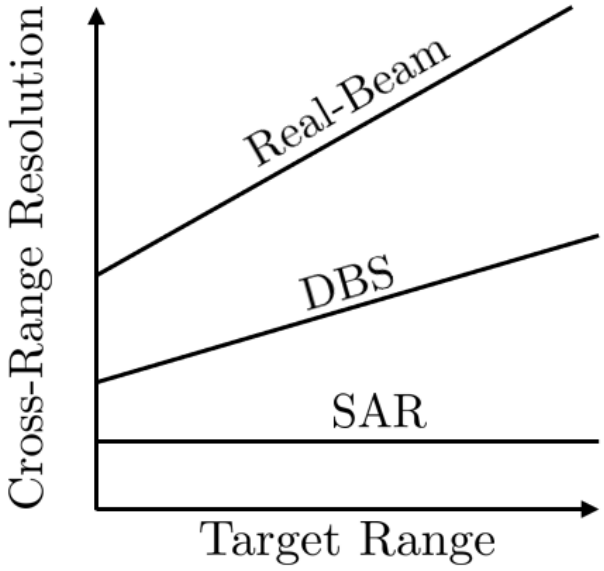

Figure 2.3: General Example of Cross-Range Resolution for the Real-Beam, DBS and SAR, with Increasing Range

There has been research from the automotive industry to use DBS to assist self parking in [Laribi et al., 2018] and resolving targets when using THz radar in [Daniel et al., 2018]. As with most applications, due to the platform which in these cases are cars, the antennas are smaller than desired. This is due to them having to be small enough to fit inside the vehicle in both a practical and aesthetic way, which results in smaller antennas and therefore wider beamwidths. Whilst designers can compensate for this using higher frequencies (e.g. 77 GHz in [Laribi et al., 2018] or low THz range in [Daniel et al., 2018]), DBS can improve resolution even further. For another civilian application, DBS can be used to differentiate between the coastline and reefs or rocks, which a conventional radar might not be able to resolve due to the superior resolution DBS provides [Kim et al., 2011].

Missile seekers also use relatively small antennas, as they are constrained by many factors such as the missile size, weight, operating platform, etc. Missile seekers benefit from using DBS, as it improves cross-range resolution without being computationally expensive like Synthetic Aperture Radars (SAR) and DBS images are generally much faster to obtain than SAR. As a generic example, DBS can be performed with a dwell time in the order of tens of milliseconds, whereas SAR is in the order of whole seconds [Stimson

et al., 2014]. DBS increases the cross-range resolution without being computationally intense, which means that it can be used in real time [G. Pietrzyk et al., 2004].

DBS can also be combined with waveform diversity to have simultaneous beams performing multiple functions. The research in [Newcombe & Balleri, 2014] demonstrates the idea of using up and down linear frequency modulated (LFM) 'chirps', to create orthogonal beams whilst performing DBS for both of the beams. Using multiple beams for a missile seeker is highly beneficial as it enables the seeker to perform multiple tasks. This could be to scan a larger area with improved coverage, scanning an area faster than before, or by scanning for targets with one beam and imaging the flight path with the other beam, which could be transmitted back to the missile firing platform for intelligence gathering.

DBS requires an offset angle between the moving platform and the target, in order to observe the changing Doppler shifts to obtain a DBS image. It is the changing Doppler shifts that create the phase history of a target, which enables the real beam of the radar to be sharpened; therefore DBS cannot be performed when heading directly towards a target. This creates a problem for missiles as they will have to use a different trajectory to perform DBS. If the offset angle is too large, the missile will have to make large turns and lose energy, but if the offset angle is too narrow, the effectiveness of DBS is reduced. There has been some unclassified research into optimising the trajectory of a missile specifically to perform DBS. Rollason et al in [Rollason et al., 2003] defined an expression of the cross-range resolution for a missile taking a DBS image, in terms of the scenario geometry, platform velocity and the dwell time of the scenario, which could be used for shaping a missile trajectory optimised to take DBS images. The work in [Farooq & N. Limebeer, 2002] optimised a missile trajectory for a seeker using DBS, which used a curved trajectory with a climb and dive manouvre, as shown in Figure 2.4.

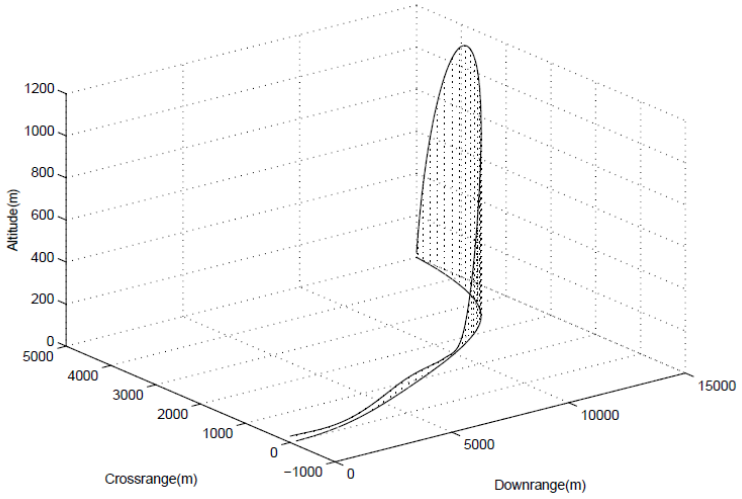

Figure 2.4: Optimised Trajectory for DBS [Farooq & N. Limebeer, 2002], © [2002] IEEE

These studies show that missiles can use DBS as a method of acquiring targets. As the signal processing for DBS is similar to that of a pulse-Doppler radar, it is difficult to know when the seeker is using this mode. However, the optimised trajectories also give a potential method of detecting when a seeker is using the DBS mode.

It is difficult to test jamming waveforms against different seeker systems, as it is difficult to obtain them from both allied and non-allied militaries, due to the strict classification of such information. In addition, if a military body has such a missile capability to test waveforms on, it is an expensive task to do this on a real-life/in-service system. It is also worth noting that the only way to test the waveforms on enemy seekers, is after they have been fired at the target which the jammer is trying to protect.

This leads to the fact that it is difficult to know if jamming has been successful, until it is too late to react. For example, if an anti-ship missile switches on its homing radar at a range of 25 km and flies at 0.8 Mach (272.2 m/s assuming International Standard Atmosphere (ISA) conditions), the jammer has approximately 92 seconds to respond before the missile reaches the target. These high speed scenarios require sophisticated jamming systems, otherwise the ship will be hit by the missile if the counter measures are not successful, as there may not be enough time to try a different method.

Due to the cost and complexity of active radar guided missiles, there are a finite number

of designs currently in operational use by the different militaries in the world at any one time. Logic would suggest that when a jammer is trying to jam a specific seeker of a specific missile, the best way to develop the jammer and test its success, is to test it on the actual seeker itself, i.e. test the waveforms on a fully built and serviceable system. However, this is near impossible due to such systems being classified and details of the systems being withheld from the public.

2.5 DRFM Jamming

The ability to create high fidelity copies of waveforms and modify them comes from the use of Digital Radio Frequency Memory (DRFM) systems. A DRFM can store and modify waveforms using high-speed sampling and digital memory [De Martino, 2018]. DRFMs generally work by recording an incoming waveform, storing it and then repeatedly transmit the waveform back towards the victim radar periodically. It will then undergo the listening/recording phase again and cycle through this loop.

The DRFM enables phase coherency which enables coherent radar modes to be jammed such as by creating false targets in SAR images. A brief overview on using a DRFM to create false targets in SAR images is found in [Zheng Shenghua, 2004]. The paper introduces how a DRFM can be used, by intercepting the victim radar waveform, sampling and modifying the waveform according to the desired errors and then re-transmitting the waveform back to the victim radar.

Due to the advancements of electronics in recent years, the idea of 'Commercially Off-The-Shelf' (COTS) DRFMS are becoming more feasible. Several research projects have been undertaken to construct high speed DRFMs with COTS equipment [Heagney, 2018, Zhang Peng, 2015, Min Xie et al., 2015]. All three papers used Field Programmable Gate Arrays (FPGA) to create a DRFM system. The FPGAs can utilise parallel processing, giving the ability to develop a high-speed DRFM systems. As FPGAs are generic by design, they can be highly customisable and are relatively inexpensive. For example, a

development board with the FPGA chip of the 'Xilinx Virtex7' series can be purchased for approximately £3k-£4k [Xilinx, 2019]. This chip is also a later model to the Virtex6 chips used in [Heagney, 2018] and [Min Xie et al., 2015]. There is a significant amount of research output from China into the use of of DRFMs and development of DRFM test rigs. As use of the DRFM is beoming more and more prevalent, there is also some research into countering DRFM false targets. As previously stated in the introduction, electronic warfare is a continous game of cat and mouse between ECM and ECCM designers. A general method for using a DRFM is to record the incoming waveform and repeat it as desired, before recording again and repeating the cycle in a loop. One method to counteract this type of DRFM use is to jitter the PRI as suggested in [Soumekh, 2006]. Pulse diversity can also be used to effectively counter this type of DRFM, such as phase shift keying or by varying the chirp rate or pulse width (whilst maintaining bandwidth for constant range resolution) which was proposed in [Wei et al., 2016].

There has been some active research for creating false targets in SAR images and [Da-hai et al., 2007] investigated how to create false targets in SAR, by modulating the received waveform for a generic scenario. As well as investigating narrow and broadband noise jamming (which is beyond the scope of this thesis), the research in [Harness & Budge, 2014] used a varying time delay method to create false targets in a SAR image. Using this method is problematic, as it requires extremely precise timings in hardware as well as knowing the transmission time ($t = 0$) of the scenario which is difficult to calculate precisely. A method to create false targets in a SAR image by modulating the received signal is shown for missile-borne SAR in [He et al., 2014] and space-borne SAR in [Sun et al., 2014]. Both methods require knowledge of the platform trajectory, as well as the ability to coherently modify the received waveform.

Instead of broadband or narrowband jamming, which requires higher jamming power due to the processing gains of coherent radars, another method is to use Doppler or 'phase noise' jamming. The research in [Bo Lv, 2010] presents this idea. Here, the jammer receives the seeker waveform and then multiplies that waveform by video noise, where the

phase is randomly distributed between 0 and 2π. The amplitude of the jamming signal varies with time and is constrained so that the noise in the seeker DBS image occupies a distinct band in the range bins and all of the Doppler bins. This can be used to mask the presence of a target. This method also reduces the required jammer power as there is some processing gain from the jamming waveform due to a partial correlation. In order to do this, a DRFM would have to be employed by the jammer in order to sample the seeker waveform at high speeds and store in memory.

A similar effect is observed in [Hong-xu et al., 2010], where the authors propose the idea of jittering the jammer hold-on time and multiplying the phase of the received waveform by a noise waveform distributed between 0 and 2π. They also propose sampling only some of the recieved waveform, so the pulse width is less than the victim radar waveform. There will still be some processing gains in range compression due to partial correlation. They can also transmit more jittered pulses within a single PRI to create a distinct noise band at desired range and azimith bands. Another method of achieving a similar effect is presented in [Huang et al., 2015]. Here the authors propose using repeat jamming with a random delay against a SAR GMTI (Ground Moving-Target Indication) system.

As proposed in [Harness & Budge, 2014], if the jammer multiplies the seeker waveform by a random phase and repeats it back to the seeker, a distinct Doppler band can be produced, corresponding to the range resolution of the pulse. By this, if the range resolution is 5 m, a strip appears on the range Doppler map occupying all Doppler bins and has a width of 5 m in the range axis.

Whilst not directly related to this thesis, there is also a little published research in jamming bi and multistatic SAR systems. In [Wang & Cai, 2007], the authors propose transmitting a randomly jittered copy of the received waveform from outside the scene area, to mask the presence of targets in the scene. This requires the jammer receiver to be inside the scene area and the employment of a DRFM to store copies of the victim radar waveforms, as shown in Figure 2.5.

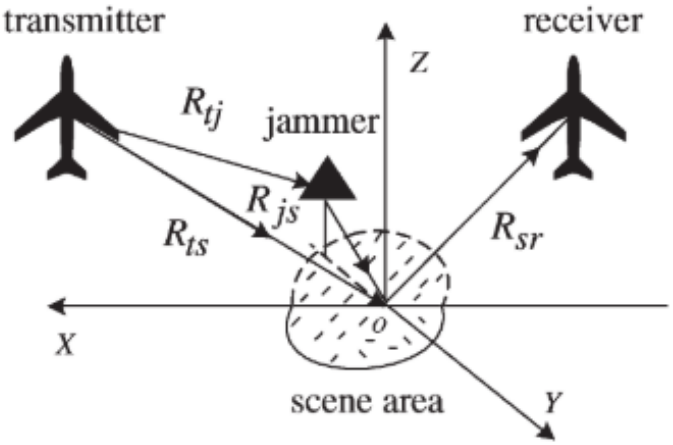

Figure 2.5: Schematic of the Jamming Technique [Wang & Cai, 2007], © 2007 IEEE

By transmitting copies of the victim radar waveforms into the scene from outside, the assumed omnidirectional scattering mitigates the problem of not knowing where the victim receiver is, due to it being passive and therefore not trackable to the radar without prior intelligence.

In [Pan et al., 2014], the authors propose jamming a bistatic Inverse Synthetic Aperture Radar (ISAR) system by undersampling the waveform of the victim radar in a sub-Nyquist manner. The jammer receives a scattered echo from a moving target and then transmits the undersampled jamming waveform at the moving target in order for the jamming waveform to be scattered towards the victim receiver. This form of deception jamming aims to create multiple false targets with the number of false targets being a function of the undersampling rate used. The sub-Nyquist method to create multiple false targets is also used in [Wang et al., 2014] against an ISAR system which uses Compressive Sensing (CS). In this setup, the ISAR is in a monostatic configuration and the jammer forms a bistatic system. The jammer receives an echo scatterered from the moving target and re-transmits an undersampled copy of the victim radar back towards the moving target in order to be scattered towards the victim radar receiver.

2.6 Conclusion

At the time of thesis publication, there is no unclassified literature for jamming DBS radar modes (apart from papers published as part of the PhD studies). If control of the position of the false target or a focused false target is required, the jammer requires knowledge of the victim platform trajectory to jam either SAR or DBS.

None of the cited literature details how to create a false target at a specific location within the victim image for a platform which is operating in a DBS mode. Nor does any of the literature explain how positional errors in the false target are induced by incorrectly estimating the platform trajectory.

There are two distinct gaps in the literature which the PhD will focus on:

1. Inserting false targets into DBS images.

2. Investigating the location of the false target when the victim platform trajectory is erroneously estimated.

Chapter 3

Background Theory

3.1 Introduction

This chapter presents the background theory required to theoretically explain how a DBS radar would operate. Several parts of this chapter are applicable to many types of radar, but it is explained with respect to a DBS radar.

3.1.1 The Radar Range Equation

The radar range equation exists in many forms and has been used throughout the PhD project as a 'Rule of Thumb' guide when making quick validation checks of simulations and measurements from the laboratory. It therefore deserves a short introduction and explanation. The radar equation is typically expressed in the form of

$$P_r = \frac{P_t G^2 \lambda^2 \sigma}{(4\pi)^3 R^4} \tag{3.1}$$

where P_t and P_r are the transmitted and received power, G is the gain of the antennas (assuming a single antenna for both transmit and receive), σ is the target cross-sectional area (RCS) and R is the range of the target from the radar.

The power density (denoted by S) of the radiated electromagnetic waves at the target

range is given by

$$S = \frac{P_t}{4\pi R^2} \tag{3.2}$$

which is found by treating the origin of a sphere as the transmission point of the waveform. For a directive antenna, the power density is

$$S = \frac{P_t G}{4\pi R^2} \tag{3.3}$$

The gain of the antenna is the ability to focus energy in a given direction when compared to an isotropic antenna and can be expressed as

$$G = \frac{4\pi A_e}{\lambda^2} \tag{3.4}$$

where λ is the wavelength of the transmitted radiation and A_e is the effective aperture of the antenna. Radar Cross Section (RCS) is a measure of the fictitious area an isotropic target would need to have in order to produce the real echo power received at the radar. For example, the Northrop Grumman B-2 Spirit aircraft is a stealthy aircraft with a wingspan in the order of 40-50 m. Due to its stealthy properties, however, it has the RCS of a small bird [Stimson et al., 2014] which would be in the order of 0.1 m^2, as opposed to an area of tens to hundreds of square metres corresponding to its actual size.

Modelling the RCS of a complex object (e.g. a ship or aircraft) is a field of study in its own right as there are many factors that dictate the RCS. However, if the target is assumed to be a perfect conductor, a flat plate and observed head on with zero aspect angle, the directional RCS, σ, of the target is given by

$$\sigma = RCS = \frac{4\pi w^2 h^2}{\lambda^2} \tag{3.5}$$

where w and h are the width and height of the flat plate respectively. Therefore, the power density reflected back towards the radar can be calculated using the ratio of RCS to the

area of a sphere

$$S_r = \frac{\sigma}{4\pi R^2} \times \frac{P_t G}{4\pi R^2} \tag{3.6}$$

This reflected power will be intercepted by the radar antenna which will have an effective aperture

$$A_e = \frac{G_r \lambda^2}{4\pi} \tag{3.7}$$

Therefore, the total received power will be

$$P_r = \frac{P_t G_t}{4\pi R^2} \times \frac{\sigma}{4\pi R^2} \times \frac{G_r \lambda^2}{4\pi} \tag{3.8}$$

If a single antenna is shared between transmit and receive (or if the gain of the transmit and receive antennas is the same), the power received at the seeker antenna will be approximately

$$P_r = \frac{P_t G^2 \lambda^2 \sigma}{(4\pi)^3 R^4} \tag{3.9}$$

The signal to noise ratio (SNR) is the ratio of the received signal power to the average noise power. Therefore,

$$SNR = \frac{P_r}{P_n} \tag{3.10}$$

where P_n is the average noise power of the system. In the next section, it will be shown that

$$P_n = kTB \tag{3.11}$$

where k is Boltzmann's constant, T the effective temperature of the noise and B is the effective bandwidth of the noise. The effective temperature, T, is commonly expressed as

$$T = T_0 F_n \tag{3.12}$$

where $T_0 = 290$ K and F_n is the noise figure of the radar. The SNR of the echo signal

received at the radar is thus

$$SNR = \frac{P_t G^2 \lambda^2 \sigma}{(4\pi)^3 R^4 k T_0 F_n B} \tag{3.13}$$

3.2 Noise

3.2.1 Measurable Thermal Noise

Thermal noise in circuits is caused by Brownian motion of electrons due to the ambient temperature [Connor, 1982]. Brownian being in reference to the Scottish Botanist, Robert Brown, who in 1827 first observed that pollen suspended in water would undergo a random "Zig-Zag" motion [Bikkin, 2013]. In the 19$^{\text{th}}$ Century, it was realised that this motion was caused by molecules in the water striking the pollen, as they themselves moved due to fluctuations in ambient temperature. In 1928, Harry Nyquist [Nyquist, 1928] formulated an equation to give the mean squared voltage (variance) across a resistor, R_n, when in thermal equilibrium at temperature T as

$$\bar{V^2} = 4kR_nTB \; volts \tag{3.14}$$

The absolute temperature T is in Kelvin and $k = 1.380650 \times 10^{-23}$ J/K. A noisy resistor can then be modelled using Thévenin's equivalent circuit, which connects a noiseless resistor in series with a noise generator.

In Thévenin's circuit, the noisy resistor, R_n, is connected in series with the noiseless resistor, R_L and the voltage generator as shown in Figure 3.1:

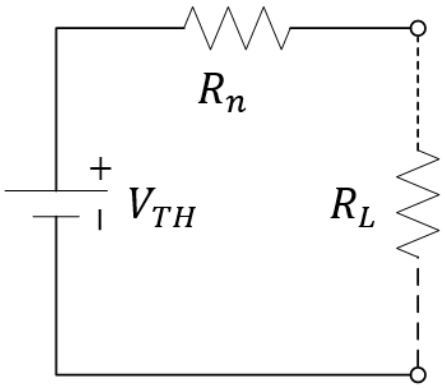

Figure 3.1: Thévenin's Equivalent Circuit

As the two resistors R_n and R_L are connected in series, the current across the two resistors is the same, giving

$$I_{R_L} = I_{R_n} = \frac{V_{TH}}{R_n + R_L} = \frac{V_{R_L}}{R_L} \tag{3.15}$$

This gives the voltage across the noiseless resistor as

$$V_{R_L} = \frac{V_{TH} R_L}{(R_n + R_L)} \; volts \tag{3.16}$$

then the mean power transferred to R_L is

$$P = \frac{\bar{V_{R_L}}^2}{R_L} \tag{3.17}$$

From Eq. (3.14) if

$$V_{TH}{}^2 = 4kTBR_n \tag{3.18}$$

then

$$P = \frac{4kTR_nB{R_L}^2}{R_L(R_n + R_L)^2} \tag{3.19}$$

The maximum-power transfer theorem states that the maximum possible power is transferred from an internal resistance R_n to a load of resistance R_L, when $R_L = R_n$ [Haykin & Moher, 2009]. When this condition is met, the power generated by the source is shared equally across the internal resistance of the source and the load resistance. The power delivered to the load is referred to as the 'available power'. Therefore the available mean noise power is equal to

$$P_n = \frac{4kTBR_n^3}{4R_n^3} = kTB \tag{3.20}$$

and is measured in Watts. Thévenin's circuit can therefore be used to model noise which is seen frequently in noise calculations.

White Gaussian Noise

White noise is a type of noise used to model thermal noise in electronic circuits. White Noise assumes that the power spectral density is constant across all of the frequency spectrum, which therefore gives infinite average power. This assumption holds until frequencies start to reach around the 10 THz range [Connor, 1982]. The term 'white' is in reference to the colour of white light, which contains equal amounts of frequencies in the visible light section of the electromagnetic spectrum.

The justification for assuming the noise to be Gaussian is based on the central limit theorem. The central limit theorem essentially states that the probability distribution of random variables tends to a Gaussian distribution when a large number of random variables are summed together [Haykin & Moher, 2009]. For example, if the noise process is infinitely sampled with replacement, the resultant distribution of the noise process should be Gaussian.

For all models in this thesis, it is also assumed that the noise process, $n(t)$, is Wide-Sense Stationary (WSS) unless otherwise stated. The first two moments of the process can be used to give a partial description of a random process. The mean of a random process is

the expected value of a random variable at a given time:

$$\mu_n(t) = E[n(t)] \tag{3.21}$$

A Random Process is stationary to the first order, if the mean of the process does not change with time, and

$$\mu_n(t) = \mu_n \tag{3.22}$$

A random process is stationary to the second order, if the autocorrelation function only changes as a function of the time difference between observation times. The autocorrelation function of a random process, is the expectation of the product of two random variables obtained from the random process, observed at two times:

$$R_x(t_1,t_2) = E[X(t_1)X(t_2)] \tag{3.23}$$

If the random process is stationary to the second order:

$$R_x(t_1,t_2) = R_x(t_2 - t_1) \tag{3.24}$$

or

$$R_x(\tau) = E[X(t+\tau)X(t)] \tag{3.25}$$

Therefore by taking the zero value of the autocorrelation function, the mean squared value or variance of the random process is obtained. As

$$R_x(0) = E[X^2(t)] \tag{3.26}$$

Whilst the mean and variance of a process only give a partial description, it is assumed for the rest of the thesis that if the random process is stationary in the first and second order, the random process is wide sense stationary (WSS) and has a Gaussian distribution unless otherwise stated.

This gives rise to the Einstein Wiener-Khinchtine equations which form a Fourier Transform pair between the power spectral density and autocorrelation function of a WSS random process [Haykin & Moher, 2009]. As

$$S_N(f) = \int_{\infty}^{\infty} R_N(\tau) e^{-i2\pi f\tau} d\tau \text{ and } R_N(\tau) = \int_{\infty}^{\infty} S_N(f) e^{i2\pi f\tau} df \tag{3.27}$$

Therefore, the zero frequency value of the PSD for a WSS random process, equals the total area under the graph of the autocorrelation function and vice versa:

$$S_N(0) = \int_{\infty}^{\infty} R_N(\tau) d\tau \tag{3.28}$$

$$R_N(0) = \int_{\infty}^{\infty} S_N(f) df \tag{3.29}$$

Therefore, the power of a WSS random process is equal to

$$E[X^2(t)] = R_N(0) = \int_{\infty}^{\infty} S_N(f) df \tag{3.30}$$

3.2.2 Power Spectral Density (PSD)

The power spectral density (PSD) of white noise is

$$S_N(f) = \frac{N_o}{2} \tag{3.31}$$

The division by two is to denote the one sided PSD of the noise where $N_o = kT_e$. T_e is defined as the temperature required to maintain a noisy resistor at a temperature which will cause it to produce the same level of noise if it is added to a noiseless version of the same system.

The Autocorrelation function of White Noise is given as

$$R_N(\tau) = \int_{\infty}^{\infty} S_N(f)df = \frac{N_o}{2}\delta(t) \tag{3.32}$$

This means that the Autocorrelation function of white noise is a delta function which is weighted by the PSD of the noise.

3.2.3 Matched Filter

Introduction

The matched filter is a linear filter that is used to maximise the signal to noise ratio of a received signal, in order to improve detection performance. The filter takes in a known waveform with additive White Gaussian Noise.
The impulse response of a linear filter, $h(t)$, is matched to the input signal. It is an image of the transmitted waveform, as

$$h(t) = s^*(-t) \tag{3.33}$$

In the frequency domain, the transfer function $H(f)$ can be calculated by taking the Fourier Transform of the impulse response

$$H(f) = \int_{\infty}^{\infty} h(t)e^{-i2\pi ft}dt \tag{3.34}$$

and the output of the matched filter in the frequency domain is

$$Y(f) = H(f)S(f) \tag{3.35}$$

To convert the output of the system from the frequency domain to the time domain, take the Inverse Fourier Transform of $Y(f)$.

$$y(t) = \int_{\infty}^{\infty} Y(f)e^{i2\pi ft}df \tag{3.36}$$

Maximising SNR

The matched filter is a filter that maximises the signal to noise ratio of the output signal in white noise. The signal to noise ratio at the output of the matched filter at sample time

τ_d is given as

$$SNR_{out} = \frac{|s_{ro}(\tau_d)|^2}{E\left[|n_o(t)^2|\right]} \tag{3.37}$$

Where $s_{ro}(\tau_d)$ is the received signal at the output of the matched filter at time τ_d and $n_o(t)$ is the additive noise. The received signal at the output of the matched filter at time τ_d is given as

$$s_{ro}(\tau_d) = \int_{\infty}^{\infty} H(f)S(f)e^{i2\pi f\tau_d}df \tag{3.38}$$

and the output power of the received signal is

$$|s_{ro}(t)|^2 = \left|\int_{\infty}^{\infty} H(f)S(f)e^{i2\pi ft}df\right|^2 \tag{3.39}$$

where $H(f)$ is the transfer function of the matched filter and $S(f)$ the spectral density of the output signal, $s_{ro}(t)$. The PSD of the noise at the output of the matched filter, $S_{No}(f)$, is

$$S_{No}(f) = S_N(f)|H(f)|^2 = \frac{N_o}{2}|H(f)|^2 \tag{3.40}$$

The output SNR can now be re-defined as:

$$SNR_{out} = \frac{\left|\int_{\infty}^{\infty} H(f)S(f)e^{i2\pi ft}df\right|^2}{\frac{N_o}{2}\int_{\infty}^{\infty}|H(f)|^2df} \tag{3.41}$$

Using the Cauchy-Schwartz Inequality:

$$|\int_{\infty}^{\infty} H(f)S(f)e^{i2\pi ft}df|^2 \leq \int_{\infty}^{\infty}|H(f)|^2df\int_{\infty}^{\infty}|S(f)|^2df \tag{3.42}$$

This is only equal if

$$H(f) = kS^*(f) \tag{3.43}$$

where k is a constant. Using the Cauchy-Schwartz inequality with the expression for the

SNR in Eq. (3.41) gives

$$\frac{|\int_{\infty}^{\infty} S^*(f)S(f)e^{i2\pi ft}df|^2}{\frac{N_o}{2}\int_{\infty}^{\infty}|S^*(f)|^2df} \leq \frac{\int_{\infty}^{\infty}|S^*(f)|^2df\int_{\infty}^{\infty}|S(f)|^2df}{\frac{N_o}{2}\int_{\infty}^{\infty}|S^*(f)|^2df} \tag{3.44}$$

therefore,

$$SNR_{out} \leq \frac{2}{N_o}\int_{\infty}^{\infty}|S(f)|^2df \tag{3.45}$$

Parseval's Theorem states that:

$$\int_{\infty}^{\infty}|S(f)|^2df = \text{Signal Energy} = \varepsilon \tag{3.46}$$

Therefore the output SNR is equal to $\frac{2\varepsilon}{N_o}$. It also shows that the SNR at the output does not depend on the design of the waveform but only on its energy.

3.3 Detection Probability

3.3.1 Introduction

Figure 3.2 shows a basic linear process of a received echo from a target and how a binary detection process can be modelled. Noise is added to the received echo and is processed through the matched filter. The output of the filter is then sampled and each sample is compared against a threshold to decide one of two hypothesises.

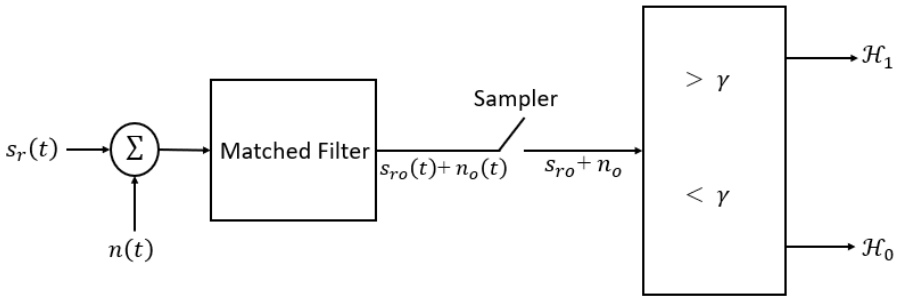

Figure 3.2: Process of Signal Detection

3.3.2 Neyman-Pearson Theorem

The Neyman-Pearson approach to the binary detection problem has been selected, to maximise the probability of detection by choosing an appropriate probability of false alarm. The binary detection scenario consists of two hypothesises:

$$\begin{aligned} \mathscr{H}0 &: s_o = n_o \\ \mathscr{H}1 &: s_o = s_{ro} + n_o \end{aligned} \tag{3.47}$$

Where s_{ro} is a received signal sample and n_o a Gaussian random variable obtained from the white noise process. This gives four possible outcomes:

1. Decide $\mathscr{H}0$ when $\mathscr{H}0$ is true. (There is not a target).
2. Decide $\mathscr{H}1$ when $\mathscr{H}1$ is true. (There is a target).
3. Decide $\mathscr{H}1$ when $\mathscr{H}0$ is true. (False Alarm/Type I error).
4. Decide $\mathscr{H}0$ when $\mathscr{H}1$ is true, (Miss/Type II error).

For the purpose of this model, both hypotheses have Gaussian Probability Density Functions (PDF), due to the assumption that the input noise process is white for each hypothesis. That is, they are assumed to be distributed according to $\mathscr{N}(\mu, \sigma^2)$ where μ is the mean, and σ^2 is the variance. Where

$$\mathscr{H}0 \sim \mathscr{N}(\mu, \sigma^2) \quad \mathscr{H}1 \sim \mathscr{N}(s_{ro}, \sigma^2) \tag{3.48}$$

3.3.3 Variances and Hypotheses

Variance is defined as the squared deviation of a random process from its mean value. Under $\mathscr{H}0$, the variance can be calculated as follows:

$$Var(s_o) = E[(s_o - \mu_0)^2] = {\sigma_n}^2 \tag{3.49}$$

Under $\mathscr{H}0$, only the noise component n_o is present which has a mean of zero. Therefore,

$$Var(s_o) = E[{n_o}^2] = \frac{N_o}{2}\int_{\infty}^{\infty} |H(f)|^2 df = {\sigma_n}^2 \tag{3.50}$$

Under $\mathscr{H}1$, both the received echo from a target and the noise process is present. This gives a variance of

$$Var(s_o) = E[s_o - {\mu_1}^2] = E[(s_o - s_{ro})^2] = E[{n_o}^2] = \frac{N_o}{2}\int_{\infty}^{\infty} |H(f)|^2 df = {\sigma_n}^2 \tag{3.51}$$

Therefore, the variances of the matched filter output for both hypotheses are the same. The mean of $\mathscr{H}1$ is the received signal sample, s_{ro}. This therefore means that the outputs of the matched filter for each hypothesis can be shown to be

$$\begin{aligned} \mathscr{H}0 &: y(t) \sim \mathscr{N}(0, {\sigma_n}^2) \\ \mathscr{H}1 &: y(t) \sim \mathscr{N}(s_{ro}, {\sigma_n}^2) \end{aligned} \tag{3.52}$$

3.3.4 Obtaining Probability of Detection

First, the Probability of False Alarm (P_{FA}) is constrained by choosing a threshold:

$$P_{FA} = (\mathscr{H}_1 \,|\, \mathscr{H}_0) = P_r\{s_o > \gamma | \,\mathscr{H}_0\} = \int_{\gamma}^{\infty} \frac{1}{\sqrt{2\pi{\sigma_n}^2}} e^{-\frac{x^2}{2{\sigma_n}^2}} dx = Q\left(\frac{\gamma}{\sqrt{{\sigma_n}^2}}\right) \tag{3.53}$$

The Q function is the right tail probability function for Gaussian distributions. This can be summarised by: '$Q(\gamma) =$ The probability that a standard normal random variable exceeds γ'. Mathematically, the Q function is described as:

$$Q(\gamma) = \frac{1}{\sqrt{2\pi}} \int_{\gamma}^{\infty} e^{-\frac{x^2}{2}} dx \tag{3.54}$$

If a specific P_{FA} is required, the threshold can be determined for a given (P_{FA}) by

$$\gamma = \mu_0 + \sqrt{\sigma_n{}^2} Q^{-1}(P_{FA}) \tag{3.55}$$

The probability of detection, P_D, is the probability of choosing $\mathscr{H}_1$ when $\mathscr{H}_1$ is true and can be calculated by

$$P_D = (\mathscr{H}_1 \,|\, \mathscr{H}_1) = P_r\{s_o > \gamma | \, \mathscr{H}_1\} = Q\left(\frac{\gamma - \mu_1}{\sqrt{\sigma_n{}^2}}\right) \tag{3.56}$$

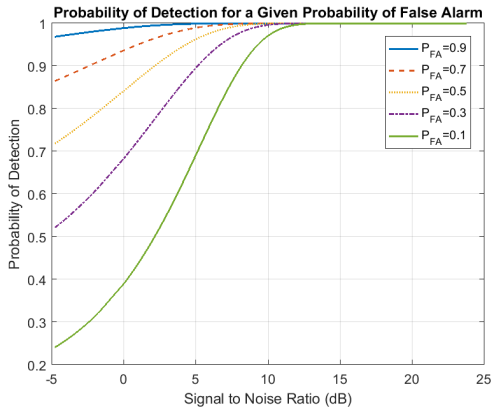

Figure 3.3: Probability of Detection for a Given Probability of False Alarm

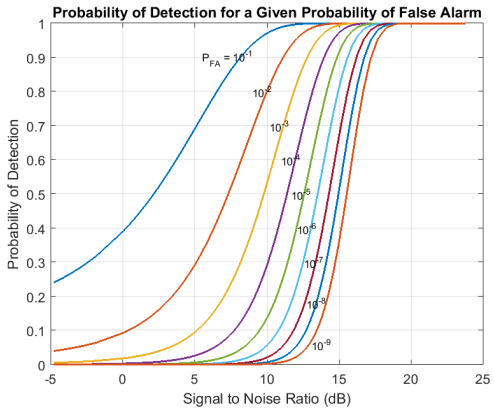

Figure 3.4: Probability of Detection for a Given Probability of False Alarm

Figure 3.3 demonstrates that for a given SNR, the probability of detection increases as the probability of false alarm increases. Where

$$SNR = \frac{s_{ro}{}^2}{\sigma_n{}^2} \tag{3.57}$$

However, having a high probability of detection is not particularly useful for detecting

targets when the probability of false alarm is also high. Generally, radar systems require the P_{FA} to be in the order of 1×10^{-8} and a P_D of 0.9 or more. With this P_{FA}, the SNR needs to be approximately 16dB as shown in Figure 3.4.

3.3.5 Obtaining a Probability of False Alarm

The Neyman-Pearson approach to hypothesis testing, enables either a threshold or probability of false alarm to be specified, in order to calculate either one of the two parameters. I.e.

$$\gamma = \text{Threshold} = \mu_0 + \sqrt{\sigma_n{}^2} Q^{-1}(P_{FA}) \tag{3.58}$$

$$P_{FA} = Q\left(\frac{\gamma - \mu_0}{\sqrt{\sigma_n{}^2}}\right) \tag{3.59}$$

By selecting an appropriate false alarm, the threshold for deciding which hypothesis can therefore be calculated. Figure 3.5 shows that the number of false alarms from a sampled noise set should coincide with the calculated probability figure. To estimate the false alarm from a sampled noise set, divide the number of false alarms by the total number of samples. This should approximate to the probability of false alarm calculated using the Q function. Figure 3.5 presents a nominal example of using a P_{FA} of 0.1 with 1000 samples being measured. From the example, the measured false alarm rate is 0.096, which is approximately 0.1. As the sample size increases, the false alarm rate should approach exactly 0.1 by using the law of large numbers.

Naturally, for a radar system in operation, such a high number of false alarms is undesirable. Therefore, a much lower probability of false alarm is required around the order of 1×10^{-8}, which should give only 1 false alarm in 100,000,000 samples. Figure 3.6 demonstrates this.

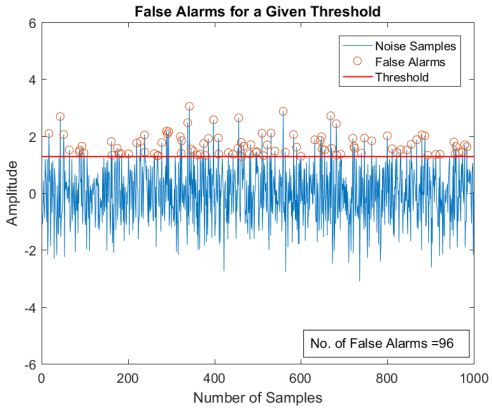

Figure 3.5: Measured False Alarms for $P_{FA} = 0.1$ and ${\sigma_n}^2 = 1$

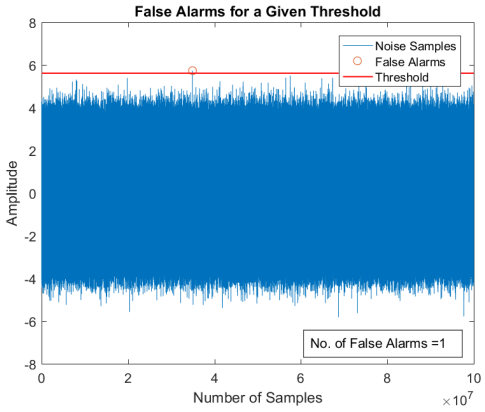

Figure 3.6: Measured False Alarms for $P_{FA} = 1 \times 10^{-8}$ and ${\sigma_n}^2 = 1$

3.3.6 Noise Jamming

This section follows the scheme as depicted in Figure 3.2, but also adds a noise jamming signal. If the jamming signal is WGN, it will have a mean of zero and a variance, ${\sigma_J}^2$, of

$$ {\sigma_J}^2 = \frac{J_{ro}}{2} \int_{\infty}^{\infty} |H(f)|^2 df \tag{3.60} $$

where $\frac{J_{ro}}{2}$ is the one-sided jammer noise power spectral density. The variance of the total noise is therefore

$$ {\sigma_T}^2 = \frac{J_{ro}}{2} \int_{\infty}^{\infty} |H(f)|^2 df + \frac{N_o}{2} \int_{\infty}^{\infty} |H(f)|^2 df = \frac{(J_{ro} + N_o)}{2} \int_{\infty}^{\infty} |H(f)|^2 df \tag{3.61} $$

Under $\mathscr{H}_0$, only the WGN is present in the form of background noise and the jammer. Therefore both will have a mean of zero. Therefore

$$ Var(s_o) = \frac{(J_{ro} + N_o)}{2} \int_{\infty}^{\infty} |H(f)|^2 df = {\sigma_T}^2 \tag{3.62} $$

Under $\mathscr{H}_1$, the variance is going to be the same as it is in $\mathscr{H}_0$.

$$ Var(s_o) = E[(s_o - s_{ro})^2] = E[(n_o + J_o)^2] = {\sigma_J}^2 \tag{3.63} $$

3.3.7 Increasing the Probability of False Alarm

When $\mathscr{H}_0$ is true and there is not a target present, noise jamming of this type will increase the number of false alarms to a number greater than the designed false alarm rate. This is assuming the model assigns a threshold to decide $\mathscr{H}_0$ or $\mathscr{H}_1$, when the system is designed and cannot adjust detection thresholds during operation. For example, in Figure 3.5, the probability of false alarm is set to 0.1. This means that in a thousand samples, there should be approximately one hundred false alarms. In the case of Figure 3.7, the threshold and probability of false alarm are set to 1.2816 and 0.1 respectively. The threshold value was calculated using Eq. (3.58). These figures are obtained by assuming that the noise power or noise variance is one. If the noise variance is set to two, due to WGN jamming, then the new false alarm rate will be

$$P_{FA} = Q\left(\frac{\gamma}{\sqrt{\sigma_T^2}}\right) = Q\left(\frac{1.2816}{\sqrt{2}}\right) = 0.18 \tag{3.64}$$

The newly calculated P_{FA} agrees with the measured number of false alarms in Figure 3.7. The measured P_{FA} can be calculated by:

$$P_{FA} = \frac{176}{1000} = 0.176 \tag{3.65}$$

The deviation from 0.18 can be accounted for by the law of large numbers in that the sample size was not large enough to get to 0.18.

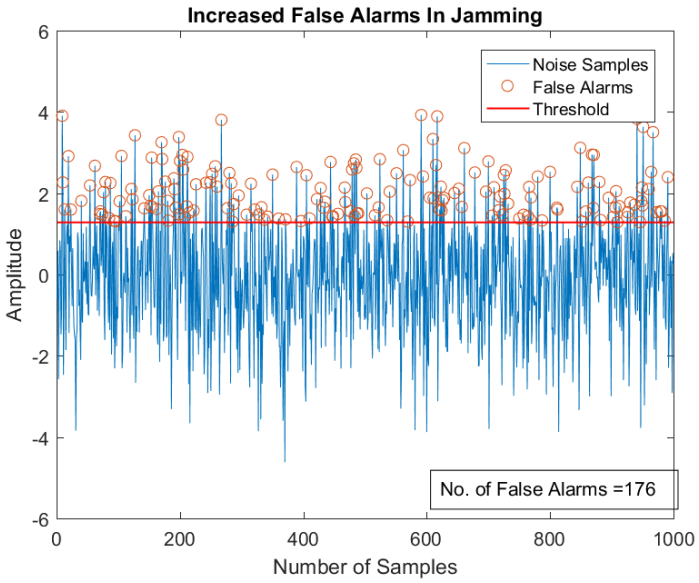

Figure 3.7: False Alarm rate with ${\sigma_T}^2 = 2$

3.4 Doppler Beam Sharpening

3.4.1 Introduction

Modern RF seekers are becoming increasingly more capable of medium to high resolution target imaging capabilities. Doppler Beam Sharpening (DBS) is a crude imaging radar, that was a precursor to Synthetic Aperture Radar (SAR). DBS uses relative motion between the target and the platform, to resolve targets or dominant scatterers within the same target in cross-range, by exploiting the Doppler effect.

3.4.2 Cross-Range Resolution: Real Beam Vs DBS

Modern radars used Active Electronically Scanned Array (AESA) antennas to transmit and steer the illuminating beam. They consist of many elements in a variety of configurations, such as planar, linear, circular, etc. These elements each independently transmit radiation through dedicated transmit/receive modules to create a beam pattern. This differs from a Passive Electronically Scanned Array (PESA) whose elements do not in-

dependently transmit, but instead receive a feed of power generated from a single source high-power amplifier. Both AESA and PESA antennas use electronic steering to steer the illuminating beams, but it is generally considered that AESA is an improved version of PESA. The benefits of an AESA antenna over a PESA is generally an increased reliability (no single point of failure with power generation), an ability to transmit multiple beams at different frequencies and a higher overall transmit power.

Instead of physically turning the antenna like mechanically scanned radars do, AESA antennas apply phase shifts to the elements, to steer the beam in the desired direction to illuminate the target. The benefits of using an AESA antenna, is that they are typically more reliable as there are less moving parts (e.g. gimbals and servos) which can lead to mechanical faults and many elements can fail before the array needs replacing. AESAs also have better beam agility than a mechanically scanned array as they can electronically switch to illuminate a different direction, rather than mechanically rotate the antenna to the desired position [Stimson et al., 2014].

AESA antennas are a modern feature and older mechanically scanned arrays are being upgraded to the modern AESA type. For example, in 2016 flight trials began [Eurofighter, 2016] for a new AESA radar on the Eurofighter Typhoon, an aircraft which entered service with the Royal Air Force (RAF) in 2003 with a mechanically scanned radar, known as Captor-M [Royal Air Force, 2019].

One of the key design parameters of AESA antennas is the spacing between the elements. They are typically spread apart with spacings of approximately $d < \frac{\lambda}{2}$. Generally, to avoid grating lobes the spacing should be less than

$$d < \frac{\lambda}{1 + sin(\Delta\theta)} \tag{3.66}$$

where $\Delta\theta$ is the maximum steering angle [Blake & Long, 2009a]. For a linear array with a maximum steering angle of 60deg, $d < 0.54\lambda$. Grating lobes are the result of aliasing, caused by undersampling in the spatial domain. The array factor is essentially

an expression for the directivity of an antenna. Using Eq. (3.67), which is derived in [Blake & Long, 2009b], Figures 3.8 and 3.9 show a broadside linear array factor with and without grating lobes for a frequency of 36 GHz:

$$AF(\vartheta) = \left| \frac{\sin\left[N\frac{\pi d \sin\vartheta}{\lambda}\right]}{N\sin\left[\frac{\pi d \sin\vartheta}{\lambda}\right]} \right| \tag{3.67}$$

Where N is the total number of elements in the array, d is the element spacing and ϑ is the steering angle which for these plots, is 0°. The justification for using 36 GHz is provided in Section 5.3.1.

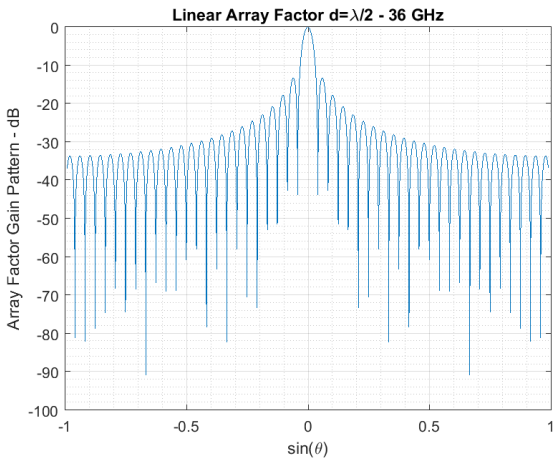

Figure 3.8: 48 element linear array factor Without Grating Lobes

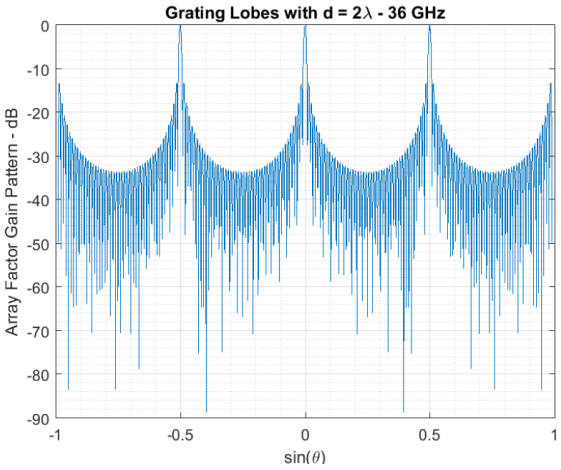

Figure 3.9: 48 element linear array Factor with Grating Lobes

One issue with AESA antennas, is that the beamwidth of the array increases with steering or look angle. A mechanically scanned array will have a constant beamwidth, but the greater the look angle for a steered beam, the greater the beamwidth. Using the halfpower beam width rule, Figure 3.10 shows how beam steering can affect the angular resolution of the radar.

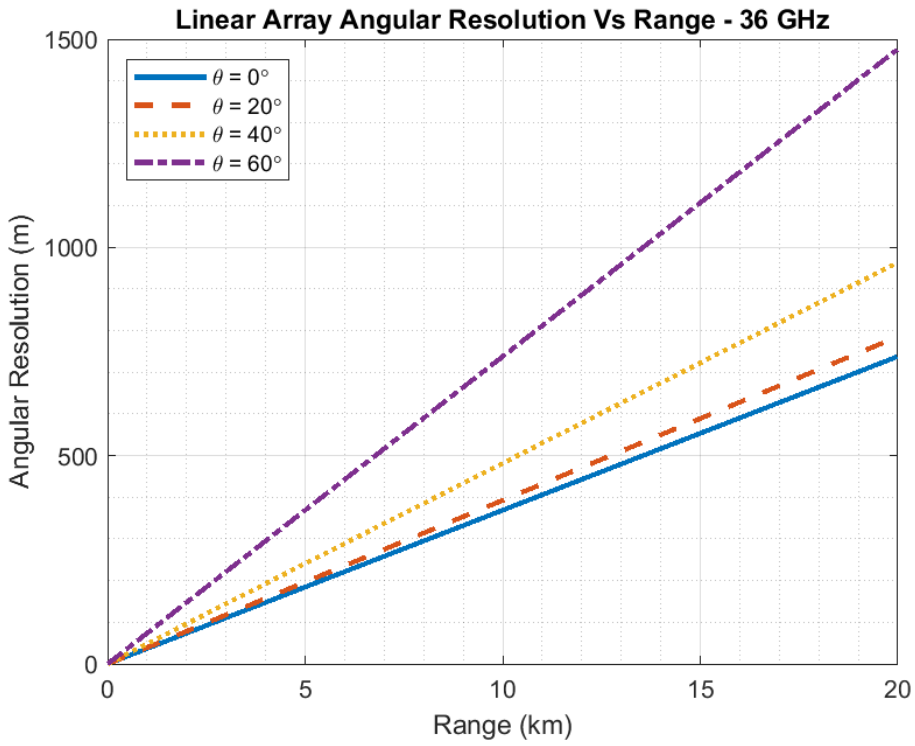

Figure 3.10: Angular Resolution of 48 element linear array with varying degrees of beam steering

DBS can increase the cross-range resolution without being computationally intense, which means that it can be used more easily in real time [G. Pietrzyk et al., 2004]. The beam of the radar is synthetically narrowed using the Doppler domain. Figure 3.11 shows an estimate of the cross-range resolutions that a real beam could achieve, if a missile uses a phased array antenna with a diameter of 0.2 m. Each plot is calculated using the 3dB or half-power beamwidth, which is calculated by [Skolnik, 2008]

$$\Theta_{3dB} = \frac{0.886\lambda}{dN_{el}} \tag{3.68}$$

Where λ is the carrier wavelength, N_{el} is the number of elements used in the antenna and d is the element spacing which is assumed to be half the wavelength. The number of elements used for each of the three decreasing wavelengths is 13, 20 and 48 respectively. The number of elements for a given antenna diameter can be increased, as the spacing between each element decreases with decreasing lambda to maintain $d = \frac{\lambda}{2}$. With such

a small antenna (due to the missile size constraints), the real beam cross-range resolution is low, which can be improved to a medium resolution with DBS. The element spacing is assumed to be half the wavelength to avoid grating lobes. The desired range resolution can be achieved using pulse compression techniques. The theoretical cross-range resolution DBS can achieve depends on the Doppler resolution, which is the inverse of the dwell time [Stimson, 1998]:

$$\delta f_d = \frac{1}{T_{dwell}} \tag{3.69}$$

Using a dwell time of 35 ms and a perpendicular trajectory to the target, Figure 3.12 was created to have a qualitative comparison between the cross-range resolutions of real beam and DBS modes. Using [Hodgson & Lee, 2003, Farooq & Limebeer, 2007, Farooq & N. Limebeer, 2002]:

$$\Delta_{CR} = \frac{\lambda R_0}{2VT_{dwell}\sin(\theta_\lambda)} \tag{3.70}$$

where R_0 is the longitudinal range or 'downrange', V is the speed of the missile and θ_λ is the angle between the platform velocity vector and target sightline. Eq. (3.70) demonstrates that the cross-range resolution is dependent on the target range. Figure 3.11 was created by calculating the 3dB beamwidth from Eq. (3.68).

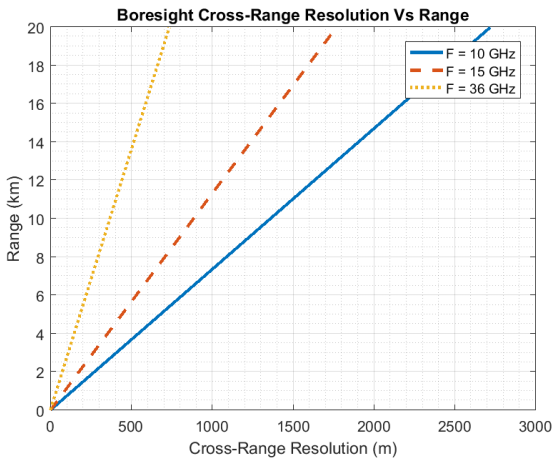

Figure 3.11: Real Cross-Range Resolution

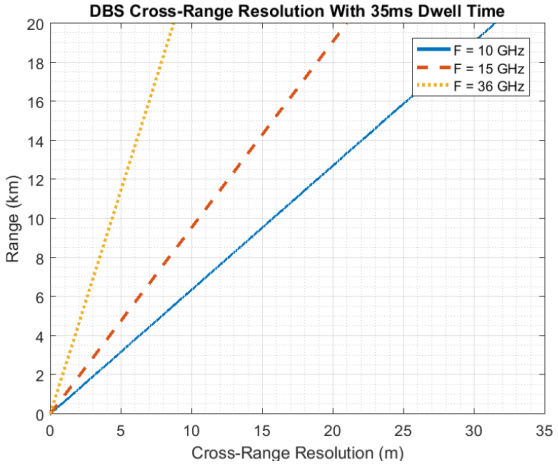

Figure 3.12: DBS Cross-Range Resolution

Figure 3.13 shows a real example of how DBS can improve the resolution of a real

beam image, which will enable the seeker to resolve targets more effectively. The parameters of the radar used for the two images are not known, but the figure is helpful as a qualitative example.

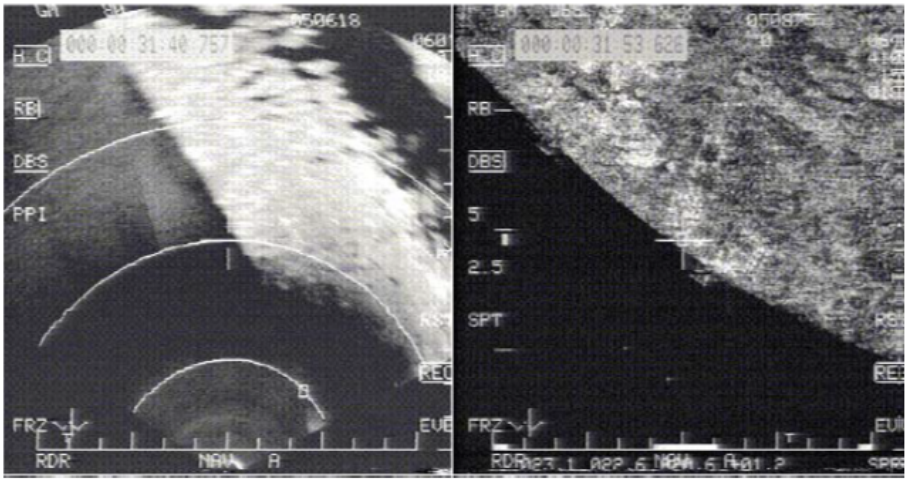

Figure 3.13: Comparison of Real Beam (left) Against DBS Image (right) [Kim et al., 2011],© [2011] IEEE

Many modern missile seekers use near millimetre wavelengths, which could have an operating frequency of 15, 36.5 or 94 GHz. The higher frequencies enable the antenna of a given size to have a narrower beamwidth and better cross-range resolution. The core component of this work is based on the Doppler effect and the Doppler shift, f_d can be calculated by

$$f_d = \frac{2V\cos\left(\theta_{fd}\right)}{\lambda} \tag{3.71}$$

Where V is the missile velocity, θ_{fd} is the angle between the Line of Sight (LOS) vector and velocity vector and λ is the wavelength of the carrier frequency. The Doppler equation shows that if the missile speed and wavelength remain constant, changing the direction of the missile will cause the Doppler shift to vary. Figure 3.15 shows this relationship at increasing multiples of Mach number. The Mach numbers are assumed to be at International Standard Atmosphere (ISA) conditions, where Mach 1 is 340.29 m/s. It can be seen in Figure 3.14 that the largest Doppler shift is observed when the missile is heading directly towards the target. Figure 3.15 shows some typical boresight Doppler

shifts with respect to Mach number.

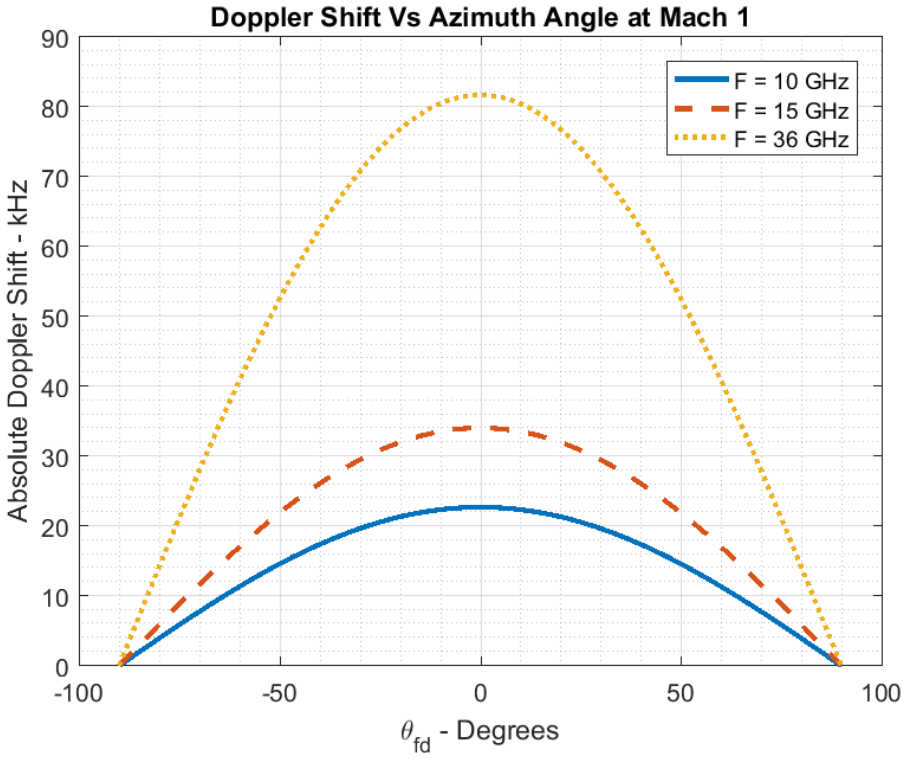

Figure 3.14: Doppler Shift with Varying θ_{fd}

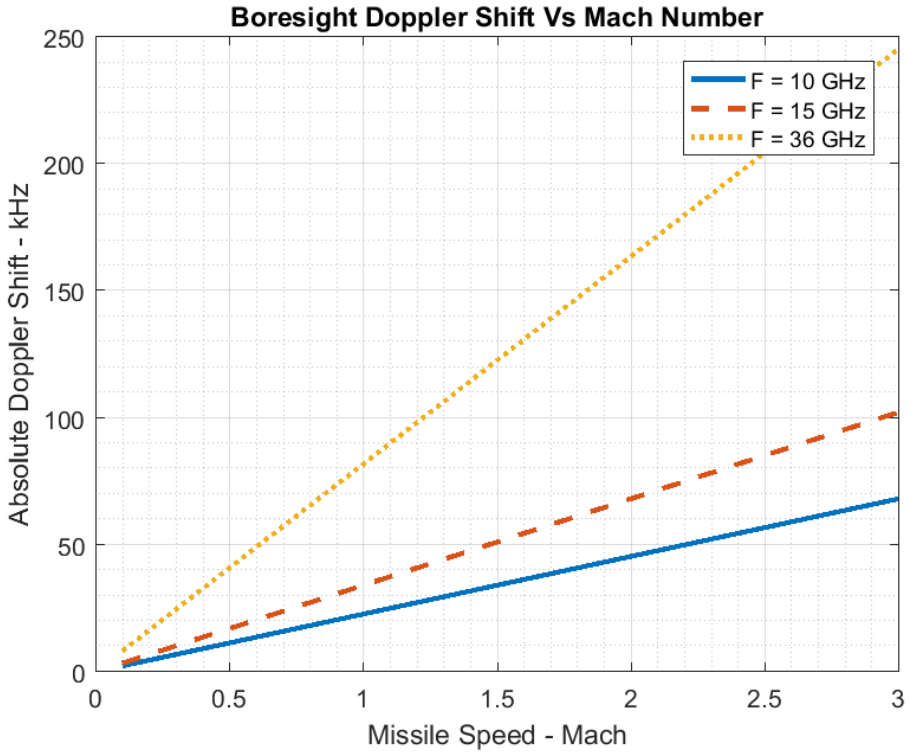

Figure 3.15: Doppler Shift for Increasing Missile Speed

Linear Frequency Modulation

DBS is a method to improve the cross-range resolution of the radar. It does not improve the range resolution. For an unmodulated rectangular pulse, the range-resolution of the waveform is given by

$$\rho = \frac{c\tau}{2} \tag{3.72}$$

where c is the speed of light and τ is the pulse width. Using this method results in a range resolution of 150 m if τ is 1 μs long, which is not desirable. To improve the resolution, shorter pulses could be transmitted. However, this would result in less energy being transmitted for a given antenna transmitter power, which reduces the effective detection range of the radar. Alternatively, a higher transmit power could be used to maintain the effective range of the radar, whilst shortening the pulse. But this will likely require an unrealistic peak transmitter power.

A technique to improve the range-resolution of the radar is to use Linear Frequency Modulation (LFM) (also known as a 'chirp') to sweep the frequency of the waveform across a bandwidth, B. A rectangular LFM pulse is given by

$$s(t) = e^{i\pi\gamma t^2} Rect\left(\frac{t}{\tau}\right) \tag{3.73}$$

where in this thesis, $Rect\left(\frac{t}{\tau}\right)$ is defined as

$$Rect\left(\frac{t}{\tau}\right) = \begin{cases} 1, & -\frac{\tau}{2} < t < \frac{\tau}{2} \\ 0, & \text{Elsewhere} \end{cases} \tag{3.74}$$

The chirp (or LFM) rate, γ, is given by:

$$\gamma = \frac{B}{\tau} \tag{3.75}$$

The larger the bandwidth, the better the range resolution. Using a bandwidth of 20 MHz gives a range resolution of approximately 7.5 m using the equation:

$$\rho = \frac{c}{2B} \tag{3.76}$$

An example of a chirp waveform with a pulse width of 10 μs is shown in Figure 3.16 and the frequency spectrum corresponding to a bandwidth, B, of 20 MHz is shown in Figure 3.17.

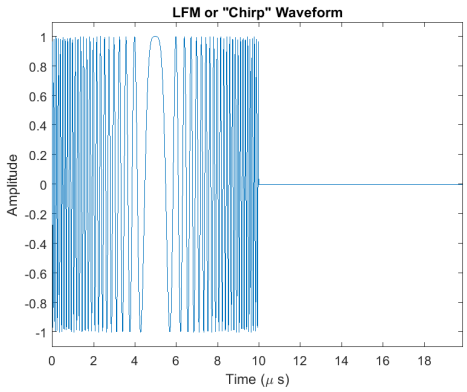

Figure 3.16: LFM or Chirp Waveform

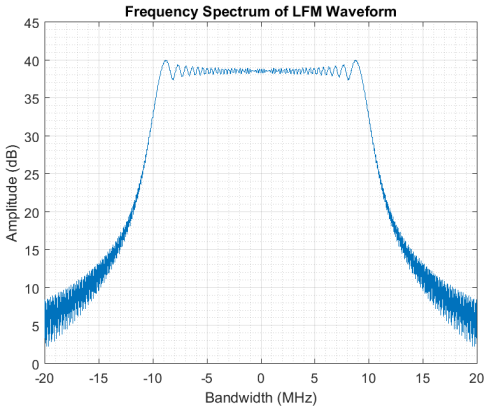

Figure 3.17: Frequency Spectrum of LFM Waveform

The range resolution from Eq. (3.76) can be observed in the output of the matched filter. The matched filter from Section 3.2.3 can be realised by the cross-correlation function between a received signal $s_R(t)$ and the transmitted signal, $s_T(t)$. To demonstrate Eq. (3.76) in an example, let

$$s_T(t) = s(t)e^{i2\pi f_c t} \tag{3.77}$$

where f_c is the carrier frequency of the waveform and $s(t)$ is the same as Eq. (3.73). If $s_T(t)$ is transmitted and delayed by an arbitrary time delay t_d , then after downmixing, the received signal is

$$s_R(t) = s(t-t_d)e^{-i2\pi f_c t_d} \tag{3.78}$$

By cross-correlating the received signal $s_R(t)$ with $s(t)$, the matched filter output is

$$s_{MF}(t) = s_T(t) * s_R(t) = \int_{\infty}^{\infty} s_T^*(t_d - t)s_R(t_d)dt_d \tag{3.79}$$

This will give a peak at the time lag where $s_R(t_d)$ matches $s_T^*(t_d - t)$. For ease of implementation and speed, the cross-correlation between the transmitted and received pulses can be found in the frequency domain. The convolution theorem states that convolution in the time domain is equivalent to multiplication in the frequency domain [Haykin &

Moher, 2009]. The cross-correlation can therefore be found by

$$s_{MF}(t) = \int_{\infty}^{\infty} \left[s_T^*(f) s_R(f) \right] e^{i2\pi ft} df \tag{3.80}$$

With a bandwidth of 20 MHz and a pulse width of 10 μs, Figure 3.18 shows the cross-correlation of a single pulse for one target at a nominal range of 10000 m. The figure demonstrates Eq. (3.76) as the width between the first nulls either side of the main peak is 7.5m.

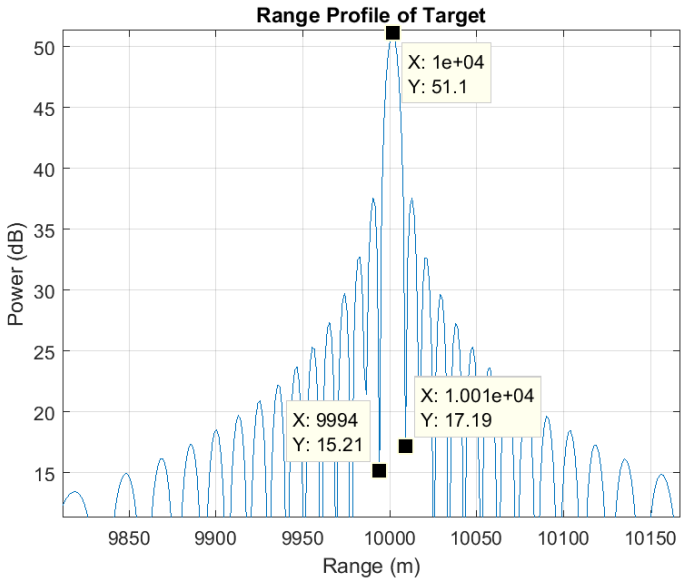

Figure 3.18: Range Profile of a Single Target for One Pulse

3.4.3 DBS Example

An example scenario for a missile using a DBS system is now detailed. The theory will explain the scenario for a single waveform first and then give the theory for a pulsed DBS system. The scenario uses four targets with two pairs at the same ranges, but separated in cross-range. Figure 3.19 shows the geometry for this scenario and Table 3.1 shows the actual target locations with respect to the missile.

Table 3.1: Jamming Scenario One Target Locations

Target	R (km)	x (m)
1	4000	100
2	4010	100
3	4010	136
4	4000	136

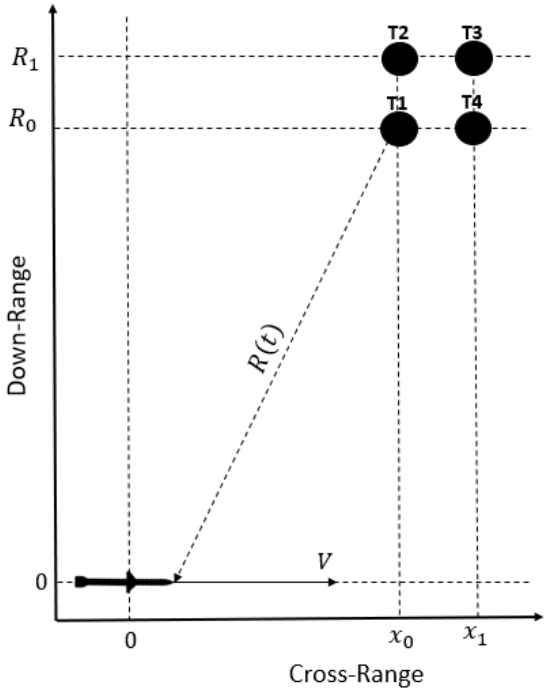

Figure 3.19: Scenario Geometry

Consider a missile seeker transmitting a signal

$$s_T(t) = s(t)e^{i2\pi f_c t} \tag{3.81}$$

flying along the x-axis of a 2D Cartesian coordinate system with dynamics

$$x(t) = Vt \tag{3.82}$$

and velocity V, where f_c is the carrier frequency of the radar. The signal reflected from a target located at a slant range R_0 and cross range x_0, as shown in Figure 3.19, can

be expressed as

$$s_R(t) = \gamma_R s(t - \tau_d(t)) e^{-i2\pi f_c \tau_d(t)} e^{i2\pi f_c t} \tag{3.83}$$

where

$$\tau_d(t) = \frac{2R(t)}{c} \tag{3.84}$$

is the echo time delay and

$$R(t) = \sqrt{(x_0 - Vt)^2 + {R_0}^2} \tag{3.85}$$

is the instantaneous target distance from the missile. Using algebraic manipulation, $R(t)$ can be redefined as

$$\sqrt{(x_0 - Vt)^2 + {R_0}^2} = R_0 \left(1 + \frac{{x_0}^2}{{R_0}^2} - \frac{2Vtx_0}{{R_0}^2} + \frac{(Vt)^2}{{R_0}^2}\right)^{\frac{1}{2}} \tag{3.86}$$

For $R_0 >> x_0$ and $t \approx 0$, $\frac{{x_0}^2}{{R_0}^2}$ and $\frac{(Vt)^2}{{R_0}^2}$ can be approximated to zero. This gives

$$R(t) = R_0 \left(1 + \frac{{x_0}^2}{{R_0}^2} - \frac{2Vtx_0}{{R_0}^2} + \frac{(Vt)^2}{{R_0}^2}\right)^{\frac{1}{2}} \simeq R_0 \left(1 - \frac{2Vtx_0}{{R_0}^2}\right)^{\frac{1}{2}} \tag{3.87}$$

For $R_0 >> x_0$ and $t \approx 0$

$$R(t) \simeq R_0 \sqrt{1 - \frac{2Vtx_0}{{R_0}^2}} = \sqrt{1 + y} \tag{3.88}$$

where

$$y = -\frac{2Vtx_0}{{R_0}^2} \tag{3.89}$$

This is where DBS differs from SAR. With short dwell times ($t \approx 0$), the higher order terms can be neglected, which will result in only linear phase terms being included in the DBS equation in Eq. 3.94. A first order taylor approximation of Eq. (3.88) can be taken,

which results in

$$\sqrt{1+y} = (1+y)^{\frac{1}{2}} = 1 + \frac{y}{2} - \frac{y^2}{8}... \tag{3.90}$$

Figure 3.20 shows that this approximation holds when the ratio of downrange (R_0) to cross-range (x_0) is large $\left(\frac{x_0}{R_0} << 1\right)$.

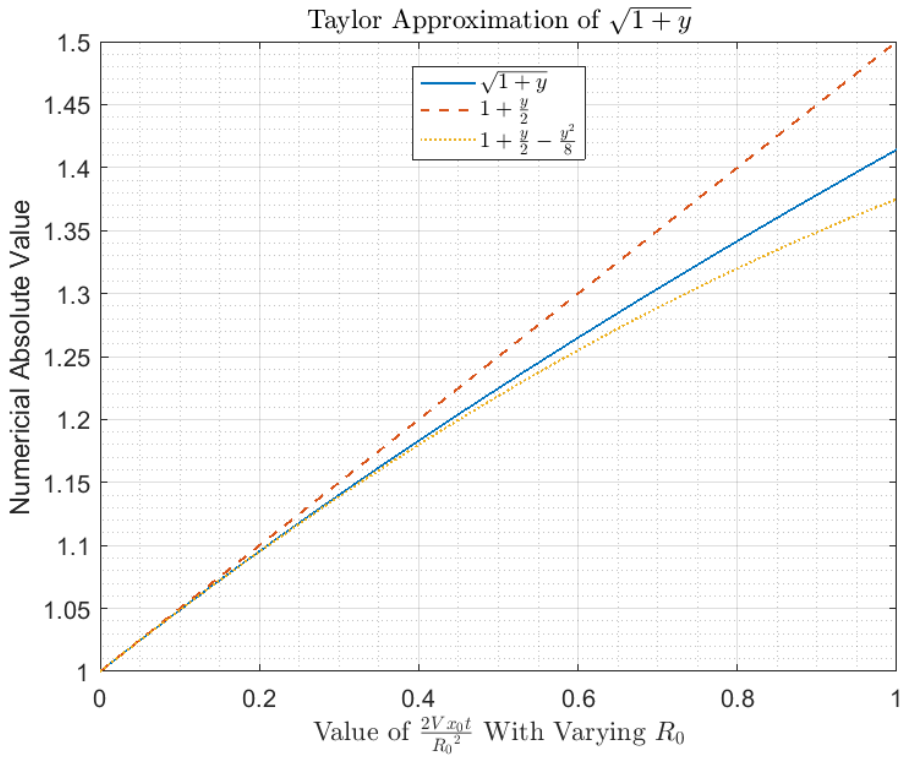

Figure 3.20: Comparison of True Value Vs Binomial Expansion of $(1+y)^{\frac{1}{2}}$

Therefore, the first order Taylor approximation about $t = 0$ leads to

$$R(t) = R_0 - \frac{Vx_0t}{R_0} \tag{3.91}$$

and

$$\tau(t) = \frac{2R_0}{c} - \frac{2Vx_0t}{cR_0} \tag{3.92}$$

Finally, the signal received by the seeker after IQ demodulation can be expressed as

$$s_R(t) = \gamma_R s(t - \tau(t)) e^{-i\frac{4\pi}{\lambda}R_0} e^{i2\pi\frac{2Vx_0}{\lambda R_0}t} \tag{3.93}$$

which after the narrowband approximation [Van Trees, 2001] becomes

$$s_R(t) = \gamma_R s\left(t - \frac{2R_0}{c}\right) e^{-i\frac{4\pi}{\lambda}R_0} e^{i2\pi\frac{2Vx_0}{\lambda R_0}t} \tag{3.94}$$

where γ_R is the two-way attenuation factor. The received signal is a delayed copy of the transmitted signal shifted in Doppler of $f_D = \frac{2Vx_0}{\lambda R_0}$. DBS measures the Doppler shift and obtains an estimate of the slant range to find the cross-range coordinate of the target.

Following the geometry and notation for a single pulse, an example of pulsed DBS system is now presented. The transmitted waveform is given by:

$$s(t) = \sum_{m=0}^{M-1} s(t - mPRI) \tag{3.95}$$

where $s(t)$ is the baseband signal, τ is the pulse width, m is the pulse number and PRI is the Pulse Repetition Interval. For this example, $s(t)$ is a Linear Frequency Modulated (LFM) or 'Chirped' pulse where

$$s(t) = e^{i\pi\gamma t^2} Rect\left(\frac{t}{\tau}\right) \tag{3.96}$$

and

$$Rect\left(\frac{t}{\tau}\right) = \begin{cases} 1, & -\frac{\tau}{2} < t < \frac{\tau}{2} \\ 0, & \text{Elsewhere} \end{cases} \tag{3.97}$$

The received signals from one target is given by

$$s_R(t,m) = \sum_{m=0}^{M-1} s(t - \tau(t) - mPRI) e^{i2\pi f_c(t-\tau(t))} \tag{3.98}$$

where m is the pulse number. Noise and clutter were considered to be negligible, as it was assumed that there was a good Signal to Noise Ratio (SNR). The scenario is measured over one Coherent Processing Interval (CPI) of 128 pulses. The received signal

$s_R(t)$ would normally be passed through a matched filter to get the range and maximise the Signal to Noise Ratio (SNR). In this case however, the matched filter is simulated by using the cross-correlation function, for ease of simplicity in the implementation in a noiseless environment. The signal parameters used are shown in Table 3.2.

Table 3.2: Signal Variables

Variable	Symbol	Value
Carrier Frequency	f_c	36 GHz
Bandwidth	B	20 MHz
Pulse Width	τ	20 μs
Chirp Rate	γ	1×10^{12} Hz^2
Pulse Repetition Frequency	PRF	20 kHz
Pulse Repetition Interval	PRI	50 μs

Before taking the Fourier transform, the raw signal can be plotted against the pulse number, to show the range profiles of the four targets which is shown in figure 3.21.

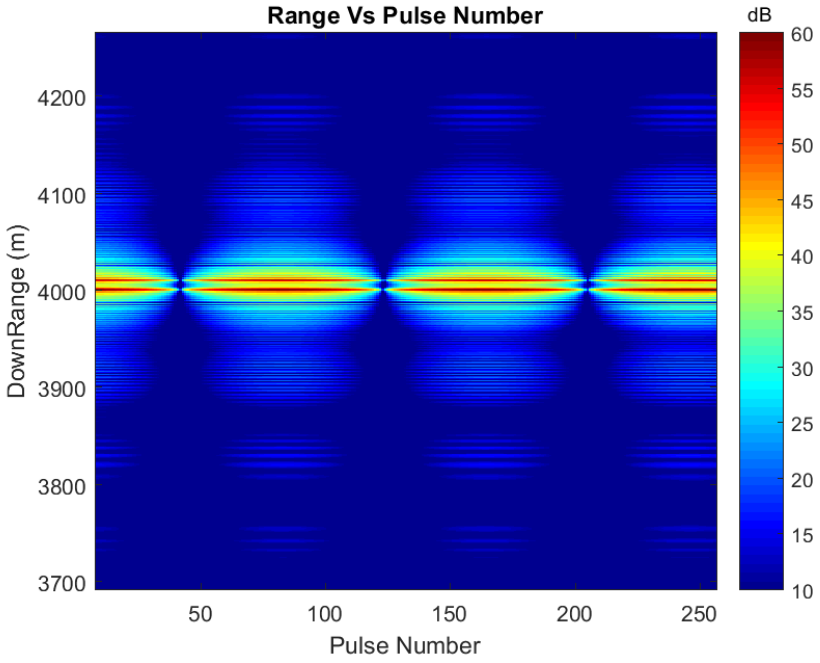

Figure 3.21: Range Profile of Targets

Figures 3.22 and 3.23 show the range and Doppler profiles for two of the four targets respectively. These plots are slices across DBS image to show the range and Doppler profiles of the targets.

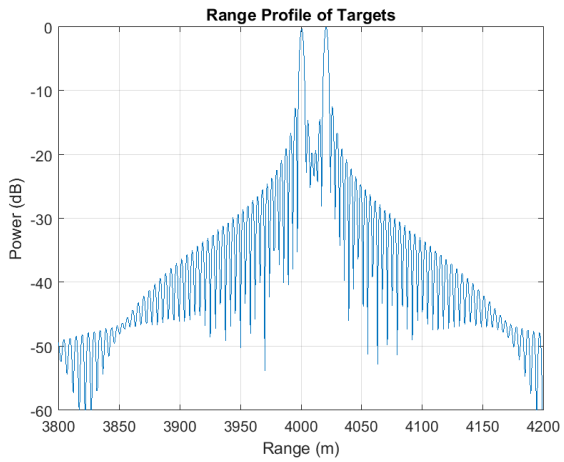

Figure 3.22: Range Profile with Two Targets

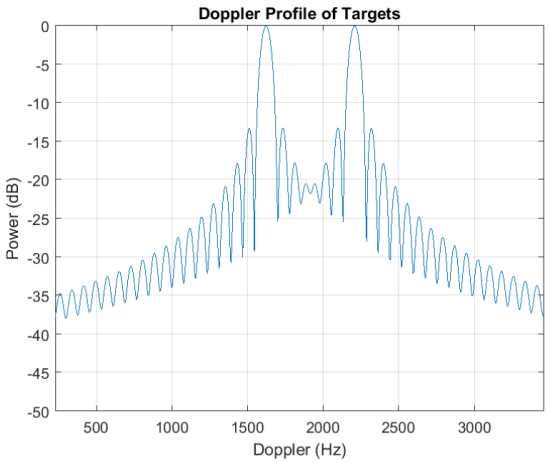

Figure 3.23: Doppler Profile of Two Targets

Range Doppler Maps

After the matched filter, the range profiles are then Fourier transformed in the azimuth direction to obtain a Range-Doppler matrix. This can then be plotted to create a Range-Doppler map, which contains the range and Doppler profiles of the four targets. Figure 3.24 shows four targets at their respective ranges and Doppler Shifts.

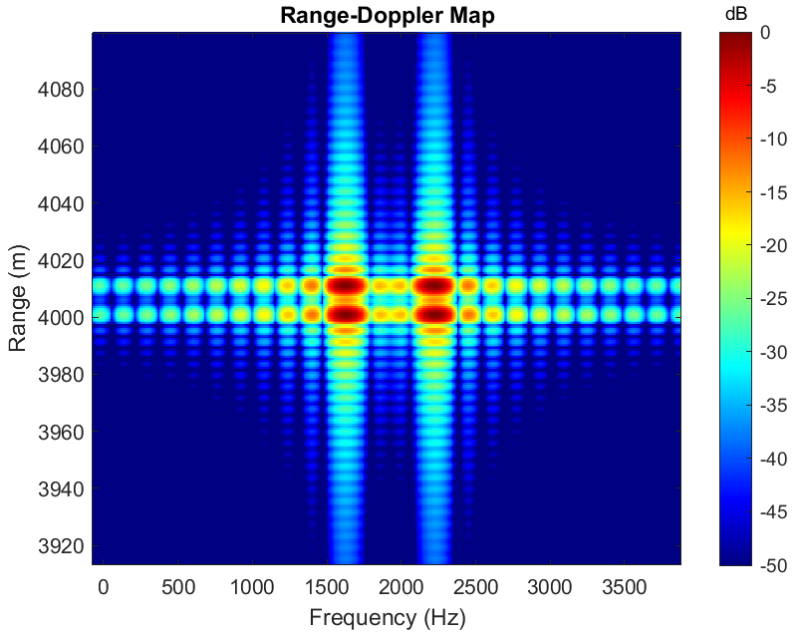

Figure 3.24: Range Doppler Map

From Figure 3.11, a conventional radar would not have been able to resolve the targets in cross-range, only in range (due to the bandwidth of the transmitted waveform), resulting in the detection of only two targets. Whereas with DBS, all four figures can be resolved.

3.5 Conclusion

An overview of general radar equations, detection processes in White Gaussian Noise, antennas and DBS has been presented in this chapter. The theory presented has been used extensively throughout this thesis and the theory used for DBS will be built upon and explored in the remaining chapters.

Chapter 4

Taking DBS Images with Hardware

4.1 Introduction

This chapter describes how a system capable of obtaining DBS images was constructed, tested, verified and subsequently implemented. A Universal Software Radio Peripheral (USRP) was used for all images taken with hardware and the setup was later modified to include jamming scenarios in future chapters. In short, the system comprises a belt driven rail that uses a stepper motor, to move the antennas in a linear motion to create an aperture and simulate a trajectory.

4.2 Overview of Experimental System

The rail is a 2 m belt driven rail, with a stepper motor driving the belt from one end of the rail to the other (either direction) in a linear motion. See Figure 4.1 for an overview of the rail. The microcontroller used to control the motor is an Arduino Uno (ATmega328P chip) and a NEMA17 bi-polar stepper motor was used as the actuator. Implementing a Direct Current (DC) motor without positional control can easily be done with just a resistor, transistor and feedback diode, with the speed controlled by Pulse Width Modulation (PWM). PWM varies the length of pulses of voltage supplied to the motor from the Arduino. It is equivalent to rapidly switching the motor on and off, where if the PWM duty

cycle is 100%, the motor is continuously running and at its maximum speed for the given load upon it. Stepper motors were favoured against a conventional DC motor, as although they are much slower compared to a DC motor, the position of stepper motors can be accurately controlled (without the need for rotary encoders) to a given step angle. They also generally provide higher torque (at the expense of speed), which was required to move the antennas, which weighed approximately 1.1 kg.

Figure 4.1: Constructed DBS Rail

4.2.1 Controlling Circuit

National Instrument's LabVIEW software controlled the Universal Software Radio Peripheral (USRP) and sent the required movement distance strings to the Arduino, via Serial connections. Arduino used a serial connection to receive the required distance from LabVIEW and then the software written for the Arduino (c++) would enable the motor to move the antenna by the desired distance. This was on a pulse-per-pulse basis. This

meant LabView would send a string to the Arduino every time it required it to move a single increment between transmitted/received pulses.

The motor used was a 'NEMA 17' 0.9° (400 steps per 360° revolution) bi-polar stepper motor. The breakout board used to interface the Arduino to the stepper motor was an A4988 'StepStick' driver board. The board has an on board translator, which means that one pulse from the Arduino gives a one step rotation in the motor and it varies the voltage to supply a constant current to the motor for each pulse.

The Arduino outputs the direction of the rotation, the step PWM and the power supply for the A4988 driver. An external 12 V power supply is connected to the A4988 driver, which the motor draws its power from. See Figure 4.2 for a full circuit diagram, which was created using 'Fritzing' software.

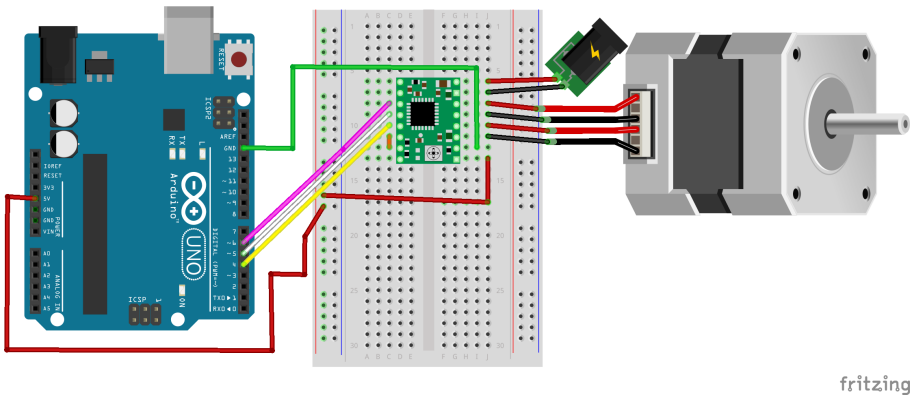

Figure 4.2: Circuit Schematic

4.2.2 Calibration of Antenna Movement

One of the key aspects of this test was to verify the precision and accuracy of the rail. Several approaches were explored. One method was to use a Vector Network Analyser (VNA), which is generally considered to be an accurate device for taking measurements. The VNA would take a measurement of a target and compare the expected phase differences between the pulses with the actual data. This method was however dismissed, because the verification of the rail should be independent of the signals generating device (e.g. a Software Defined Radio (SDR) or VNA), to help with potential fault finding in

more complicated data. It is easier to understand erroneous data if the source of the error can be independently isolated. The movable platform (in this case the rail), is a completely different type of system to the measurement system (in this case a VNA or SDR). Therefore, the two systems should not be used to calibrate each other, in order to avoid coupling of errors.

Another approach to verifying the rail accuracy was to use a laser range finder and measure the distance moved, relative to the walls of the laboratory, see Figure 4.3.

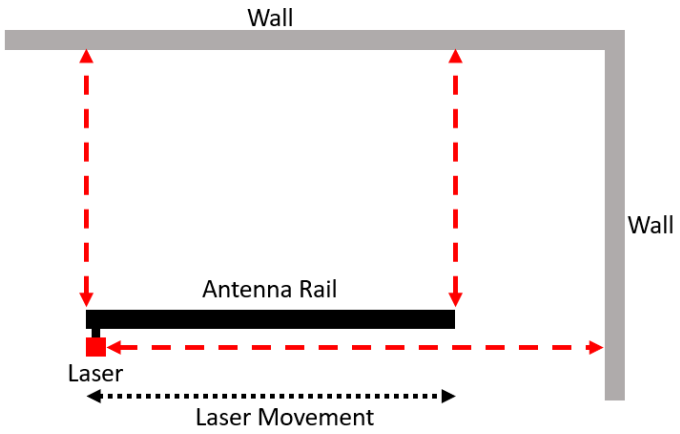

Figure 4.3: Set up for Displacement Verification With Laser

The problem with this method is that it assumes that the wall is perfectly straight and with no perturbations in its surface. A visual inspection of the wall revealed that this assumption was not fully valid. Whilst it is likely that errors induced by the pertubations would have been small (potentially less than the 1 cm resolution of the laser range finder), another method was available. The final approach was to clamp a Vernier caliper to the rail and use the antenna movement to displace the caliper, by the distance the antenna was supposed to move by. The caliper has a resolution of 1 micron which is suitable for the measurements used in calibration. See Figure 4.4 for a visual explanation.

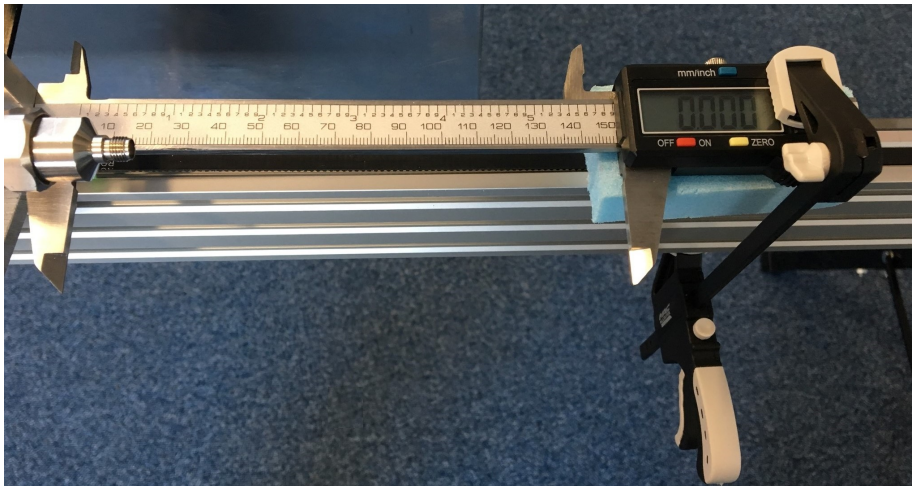

Figure 4.4: Set up for Displacement Verification

The advantage of using the clamped caliper over the laser range finder meant it was easier to repeat the measurements to the same standard as the measurements were independent of the room and rail orientation. The digital reading was recorded and then reset to zero for each step. The "NEMA 17" motor has a step of 0.9° (400 steps per 360° revolution). With the drive gear (as shown in the top-left image of Figure 4.1) being 18.57 mm in diameter (measured with the vernier caliper), one full revolution results in a horizontal displacement of 58.34 mm. In turn, one 0.9° step, results in a minimum displacement of 0.146 mm. This rounds to approximately 0.15 mm, which means that if a mm integer displacement distance is required, the integer 3 must be a factor of the displacement distance. To measure the accuracy of the rail, a total of 180 steps of 3.06 mm were used. The measurements were taken in blocks of 30 pulses at 3 locations on the rail, for both clockwise and anti-clockwise stepper motor movements, as shown in Figure 4.5.

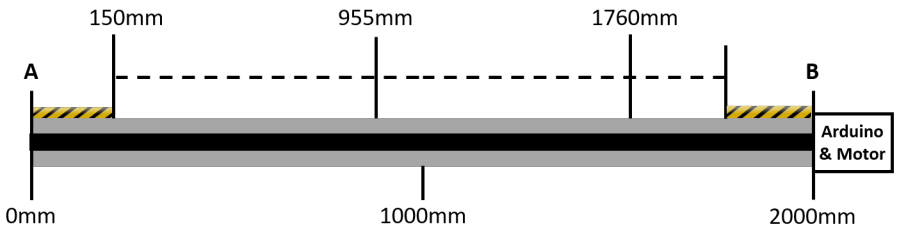

Figure 4.5: Points Along Rail Where Calibration Started

In Appendix A, Figure A.1 gives the travelled distance for each pulse measured and

shows 6 batches of 30 pulses. Figure 4.5 shows the points where the batches started from. Batches 1-3 for clockwise stepper motor rotation, were taken in the direction of A to B at the corresponding measurements shown in the Figure 4.5. Batches 4-6 from Figure A.1 used the same measurements in Figure 4.5, but instead ran from point B to A with the stepper motor rotating in an anti-clockwise direction (for an observer facing the rail with point B to the right of point A).

Due to the construction of the rail, the final 150 mm at either end is not a usable part, hence the measurements started and finished at measurements corresponding to those values. The yellow and black stripes in Figure 4.5 indicate these unusable areas. The results from the measurements are shown in Table 4.1.

Batch	Mean	Error	Standard Deviation	Average Deviation
1	3.08	0.02	0.12	0.10
2	3.12	0.06	0.13	0.08
3	3.07	0.01	0.15	0.12
4	3.08	0.02	0.14	0.11
5	3.10	0.04	0.10	0.08
6	3.05	-0.01	0.14	0.11
Total A to B	3.09	0.03	0.13	0.10
Total B to A	3.08	0.02	0.13	0.10
Total	3.08	0.02	0.13	0.10

Table 4.1: Rail Calibration Statistics (in mm) With 3.06 mm Intended Movement Distance

The experimental results for this thesis were obtained with a transmission frequency of 5 GHz and a wavelength of 6 cm. The reasons for using 5 GHz will be detailed in the next section. The mean of the total number of measured step distances has an error of 0.02 mm, which when using a wavelength of 6 cm, is an error of 0.03% and therefore not significant enough to affect the measurement result. Table 4.1 shows a consistent accuracy of step increment. This demonstrates that the system can be operated anywhere along the usable parts of the rail and in either direction.

4.3 Taking DBS Images with a USRP

Once the precision and accuracy of the rail was verified, a DBS image of a flat plate was taken. Other types of target could have been used for the measurements, such as a sphere or corner reflector. A spherical target has a Radar Cross Section (RCS) which is independent of aspect angle [Skolnik, 2008], but a small RCS when compared to a flat plate or corner reflector of a similar physical size.

A flat plate has the highest RCS out of the three types of target, when illuminated with zero aspect angle (i.e. head on). However, the RCS of a flat plate degrades rapidly to almost zero when aspect angles are introduced. The drop in RCS due to changing the aspect angle could also result in a poorer cross-range resolution (than calculated) of the target being imaged. This is due to the lack of detectable returns from the target and a subsequent shorter dwell time on the target.

The RCS of a corner reflector when illuminated with zero aspect angle is comparable to a flat plate, but generally not as high. However, a corner reflector has better coverage across a greater range of aspect angles. For the measurements taken, either a flat plate or corner reflector could have been used. Due to the geometries of the measurements and short movement of the antennas along the rail (less than 40 cm), the change in aspect angles will be small. Therefore, a flat plate target was chosen, to give the largest RCS.

A Universal Software Radio Peripheral (USRP) was used to take the measurements. A USRP is a type of software defined radio, which can be used for prototyping communication systems, radars, radios, etc. The USRP used for the measurements is the National Instruments (NI) USRP 2943R, which has a frequency range of 1.2-6 GHz. The frequency used for the experimental results in this thesis is 5 GHz. The reason for this is that it was desired to have as narrow a beamwidth as possible, for a given antenna size. However, it was decided not to use 6 GHz to avoid hitting the limits of the USRP which may have caused problems with the results. Therefore, 5 GHz was chosen as a compromise of using the highest frequency available, whilst staying well clear of the limits of the USRP. The

USRP has an instantaneous bandwidth of 40 MHz, as shown in Table 4.2. This means that the smallest range resolution possible would be 3.75 m. Whilst it would be desirable to have a better range resolution, the parameter of interest is cross-range resolution, which for DBS is dependant on the dwell time and not on the bandwidth.

Parameter	Value
Operating Frequency	$1.2 - 6$ GHz
Instantaneous Bandwidth	40 MHz
Max Output Power (3.5 - 6 GHz)	5 mW to 32 mW
Max. Sampling Rate	200 MHz
Number of Channels	4 ($2 \times$ Tx/Rx)

Table 4.2: NI USRP 2943R Specifications

The movement of the antennas was carried out in steps and was used to simulate the linear motion of a missile to test the developed theory. To reduce the complexity of the measurements, a 'stop and go' method was used between pulses, instead of continuously moving the antenna and transmitting. Using this method removed the requirement for instantaneous processing of the transmitted and received waveforms as well as removing the requirement to move the antenna at high speeds. The 'stop and go' method also enabled the simulation of higher velocities than the rail was physically capable of or different PRIs as the antenna can be moved according to the distance the seeker would travel between PRIs. For example, if the PRF is 10 kHz and the missile speed 300 m/s, the antenna can be moved 3 cm between each transmitted pulse. Therefore by controlling the distance moved by the antenna between pulses and assuming a fixed PRF, the speed can be simulated as the Doppler shifts are not observed in fast time, but in slow time between pulses.

One constraint of using this method is that the imaged scene must be stationary during the imaging period. This is due to the real time between pulses being in the order of several seconds (it takes time to move the antenna the desired distance between pulses).

All measurements were completed in the far-field region of the antennas. The far-field

of an antenna can be calculated by[Balanis, 2015]:

$$FarField \geq \frac{2D^2}{\lambda} \tag{4.1}$$

With a horn antenna that is $\approx$ 90 mm at the flared end and with an operating frequency of 5 GHz or 6 cm wavelength, the far-field is at a distance greater than 0.27 m from the antenna. The target was placed at a range of 4 m from the antenna, so was well into this region. The far-field region was used because the radiation pattern does not change with distance/range whilst in this region. The horizontal beamwidth used can be calculated by:

$$\theta_h = \frac{51\lambda}{W} = \frac{51 \times 0.06}{0.090} = 34.0^\circ \text{ or } 0.59 \text{ rad} \tag{4.2}$$

where W is the width of the antenna at the flared end. This means that at a range of 4 m, cross-range resolution of the real beam is $2R\sin\left(\frac{\theta_h}{2}\right)$ and therefore $\approx$ 2.34 m.

4.3.1 USRP Image of a Single Target

Before jamming, a DBS image of a flat plate was taken to prove that an image could be taken with a USRP. Table 4.3 shows the parameters used for the experiment.
The Radar Cross Section (RCS) of the Rectangular plate used in the experiments assumes broadside illumination and is calculated using

$$\sigma = \frac{4\pi A^2}{\lambda^2} \tag{4.3}$$

where A is the area of the target and λ is the wavelength. The rectangular plate used had dimensions 0.3 m $\times$ 0.3 m $\times$ 0.002 m, which gives an area of 0.09 m^2.

Parameter	Symbol	Value
Flat Plate RCS	σ	28.27 m^2
Frequency	f_c	5 GHz
BandWidth	B	30 MHz
Pulse Width	τ	10 μs
Chirp Rate	γ	3×10^{12} Hz^2
Sample Rate	F_s	80 MHz
Number of Pulses	M	128
Downrange	R_D	3.64 m
Crossrange	R_{cr}	1.3 m
Step Distance	Δ_x	2 mm
Pulse Repetition Interval	PRI	50 μs
Inferred Velocity	V	40 m/s

Table 4.3: DBS Image Parameters

Figure 4.6 gives the schematic for the measurement. The antenna was moved towards the rectangular plate and a chirp waveform was transmitted.

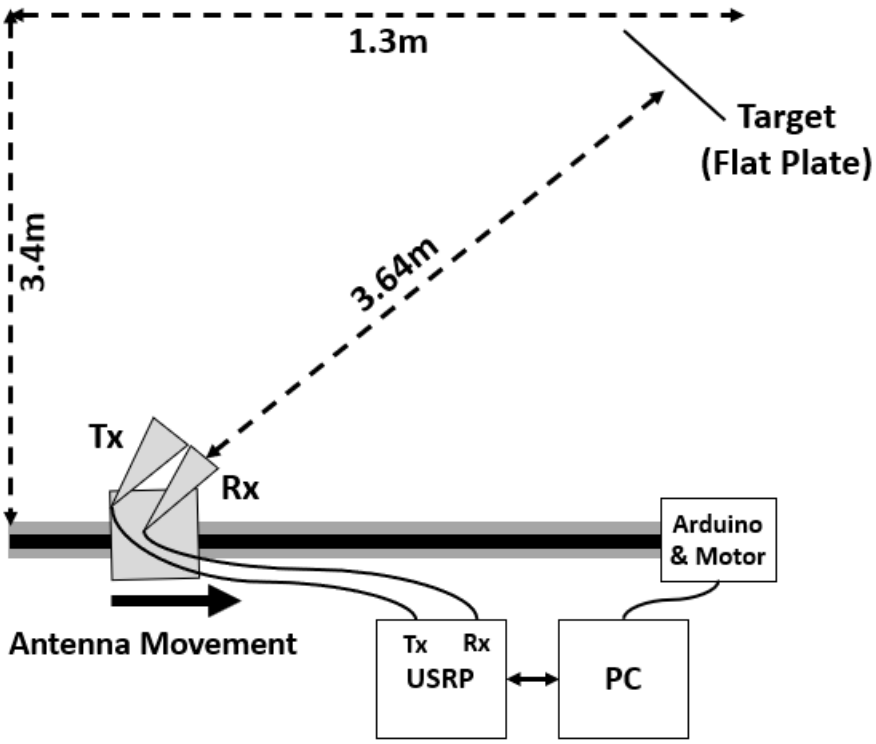

Figure 4.6: Schematic of DBS System

The transmitted signal was

$$s_T(t) = \sum_{m=0}^{M-1} s(t - m\text{PRI})\, e^{i2\pi f_c t} \tag{4.4}$$

where

$$s(t) = e^{i\pi\gamma t^2} Rect\left(\frac{t}{\tau}\right) \tag{4.5}$$

$$Rect\left(\frac{t}{\tau}\right) = \begin{cases} 1, & -\frac{\tau}{2} < t < \frac{\tau}{2} \\ 0, & \text{Elsewhere} \end{cases} \tag{4.6}$$

Figures 4.7 and 4.9 show the transmitted and received waveforms for a single step, as well as their corresponding frequency spectrums, which demonstrate a bandwidth of 30 MHz was used.

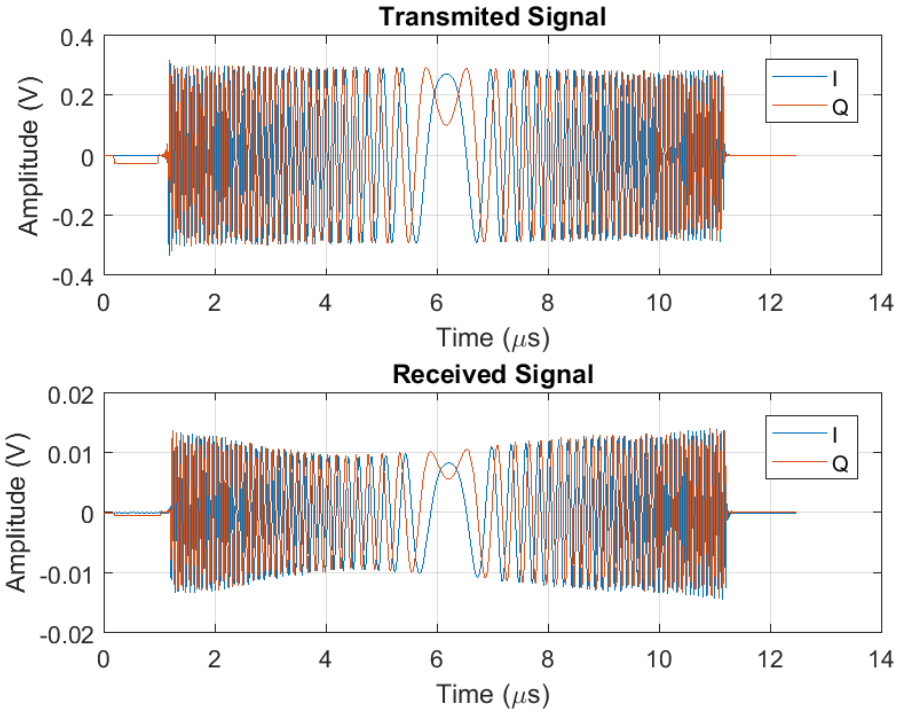

Figure 4.7: Transmitted and Received Signal from Target

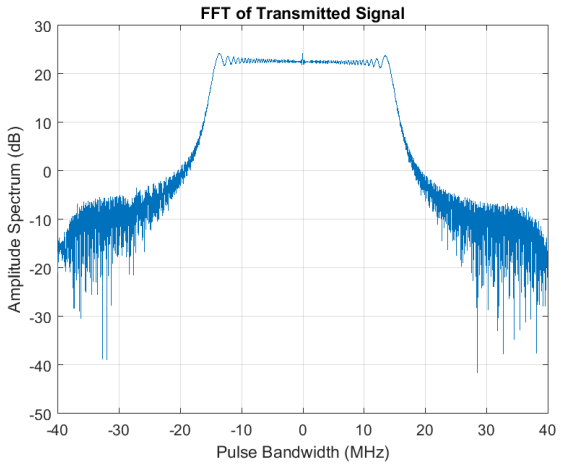

Figure 4.8: FFT of Transmitted Signal

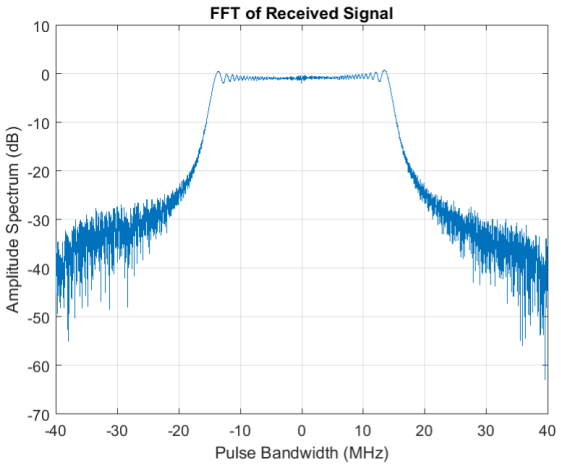

Figure 4.9: FFT of Received Signal

Figure 4.11 shows the range and cross-range profiles of the target. To factor in the length of the cables ($\simeq$ 1.3 m each), the two cables were connected together and a single pulse (identical to the transmitted pulses for each experiment) was transmitted and received through the cables. This single pulse was then stored and used to correlate the received pulses to create the DBS images in this thesis. The null-to-null width of the main

lobe of the range profile is 10 m wide and the 3dB width is 5 m which is expected when a bandwidth of 30 MHz is used. From Table 4.3, the Doppler resolution, δ_{fd}, is 156.25 Hz $\left(\frac{1}{T_{dwell}}\right)$ which will give a cross-range resolution [Hodgson & Lee, 2003, Farooq & Limebeer, 2007, Farooq & N. Limebeer, 2002] of

$$\Delta_{CR} = \frac{\lambda R_0}{2VT_{dwell}\sin(\theta_\lambda)} = \frac{0.06 \times 3.64}{2 \times 40 \times 0.0064 \times \sin(69.08^\circ)} = 0.46 \text{ m} \qquad (4.7)$$

where θ_λ is the angle between the platform velocity vector and target sightline $\left(\tan^{-1}\left(\frac{3.4}{1.3}\right)\right)$. The null-to-null width of the main peak for the cross-range profile is approximately 1m, giving a 3dB width of approximately 0.5 m, which agrees with Eq. (4.7).

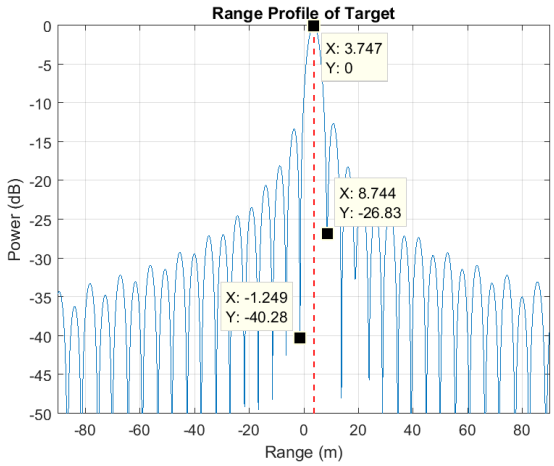

Figure 4.10: Range Profile of Target

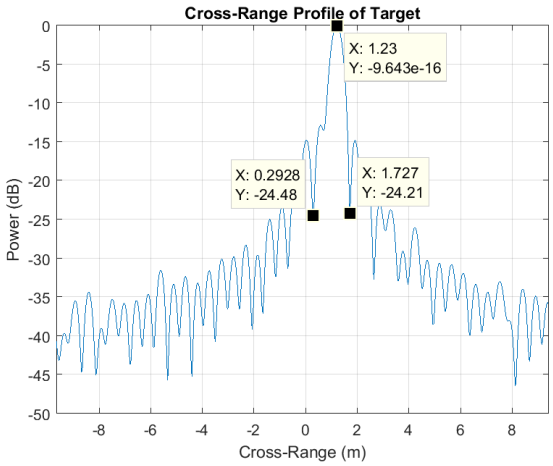

Figure 4.11: Cross-rangeProfile of Target

The range profile for all of the pulses is shown in Figure 4.12. The figure shows a constant range profile for the target.

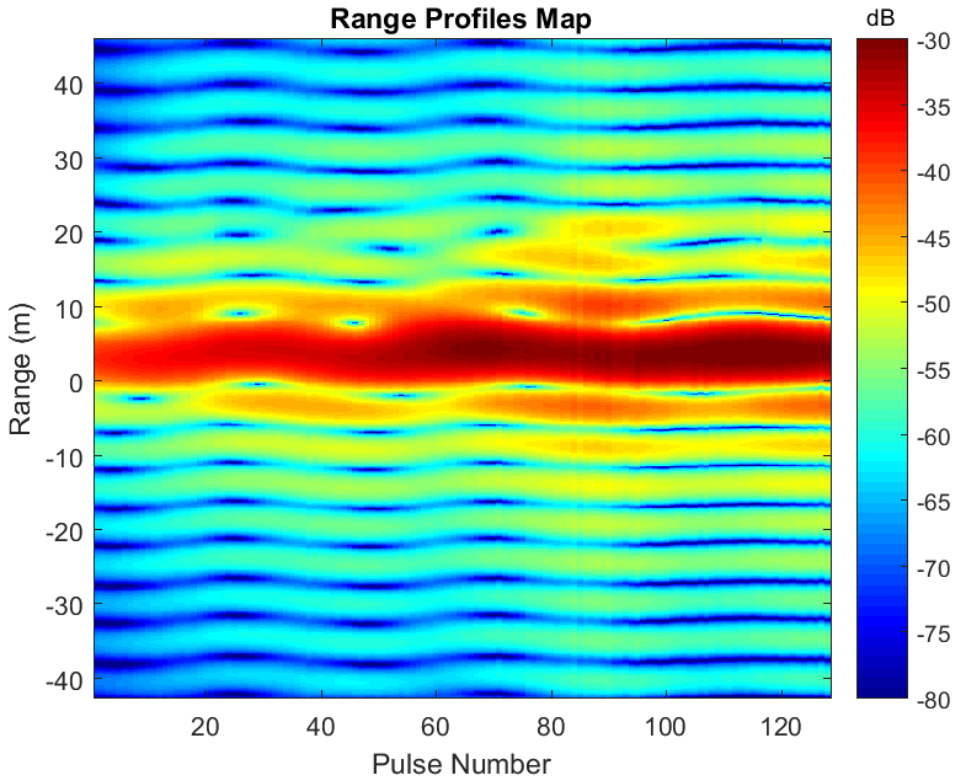

Figure 4.12: Output of Matched Filter

Figure 4.13 shows the range-Doppler map for the target and the DBS image for the target. Based on the geometry of the scenario, the expected Doppler shift is

$$f_d = \frac{2Vx_0}{\lambda R_0} = 476.19 \text{ Hz} \tag{4.8}$$

and the Doppler shown in the figure demonstrates this expected value.

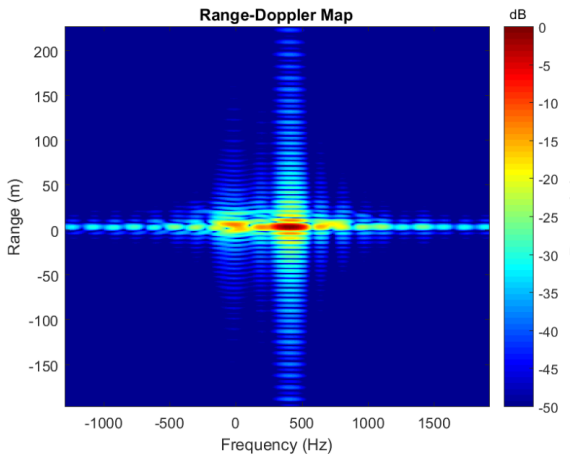

Figure 4.13: Range-Doppler Map of Imaged Target

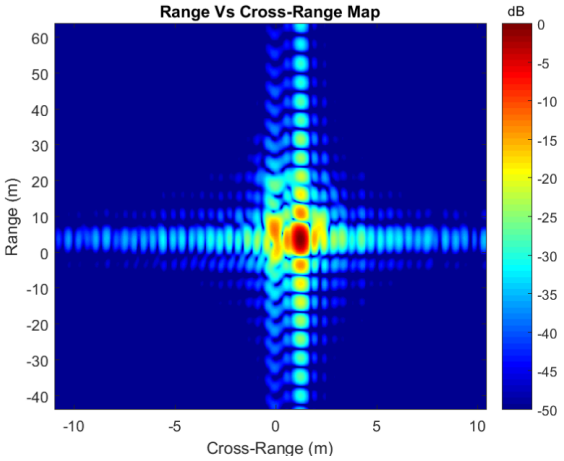

Figure 4.14: DBS Image of Imaged Target

4.3.2 Demonstrating DBS with Two Targets

The benefit of using DBS, is to increase cross range resolution and to resolve targets which are closer in cross-range, than the resolution of the real beam of the radar. Therefore, a second measurement was taken to show how DBS can resolve two targets in cross-range, which are closer than the cross-range resolution that the real beam can resolve. There are two measurements, one completely stationary, which should show one target at zero Doppler and the correct range and a second DBS image, showing how two targets were resolved by performing DBS. Both sets of images are taken using the signal parameters shown in Table 4.4.

Parameter	Symbol	Value
Flat Plate RCS	σ	28.27 m^2
Frequency	f_c	5 GHz
BandWidth	B	30 MHz
Pulse Width	τ	10 μs
Chirp Rate	γ	3×10^{12} Hz^2
Sample Rate	F_s	80 MHz
Number of Pulses	N_p	128
Downrange	R_D	4 m
Cross-range	R_{cr}	0.5 m and 1.8 m
Step Distance	Δ_x	2 mm
Pulse Repetition Interval	PRI	50 μs
Inferred Velocity	V	40 m/s

Table 4.4: DBS Image Parameters

The geometry for both sets of images is shown in Figure 4.15. The layout and setup is very similar to the previous scenario with just a single target, but now with two targets and slightly different cross-range positions.

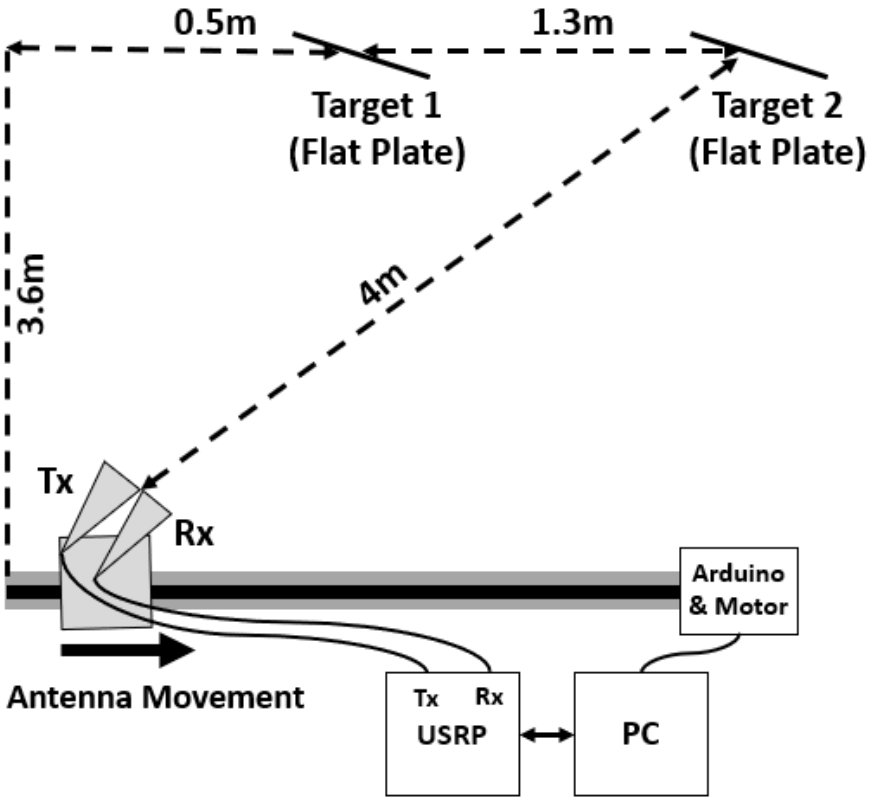

Figure 4.15: Schematic for Two Targets Separated by 1.3 m

Stationary Measurement of Two Targets

The purpose of conducting a stationary measurement is to demonstrate that the theory of DBS presented in Chapter 3 is correct. The theory says DBS requires a changing Doppler shift caused by either platform or target motion across the real-beam to increase cross-range resolution. When stationary, the DBS image will show one target at 0 Hz Doppler and a target at 4 m in range, as shown in Figures 4.18 and 4.19. The cross-range resolution was approximately 2.34 m as previously calculated, so the real beam could not resolve the two targets without using DBS.

Figure 4.16 shows constant range profiles at approximately 4.5 m. The purpose of this figure is to show that the range was constant across each pulse of the measurement.

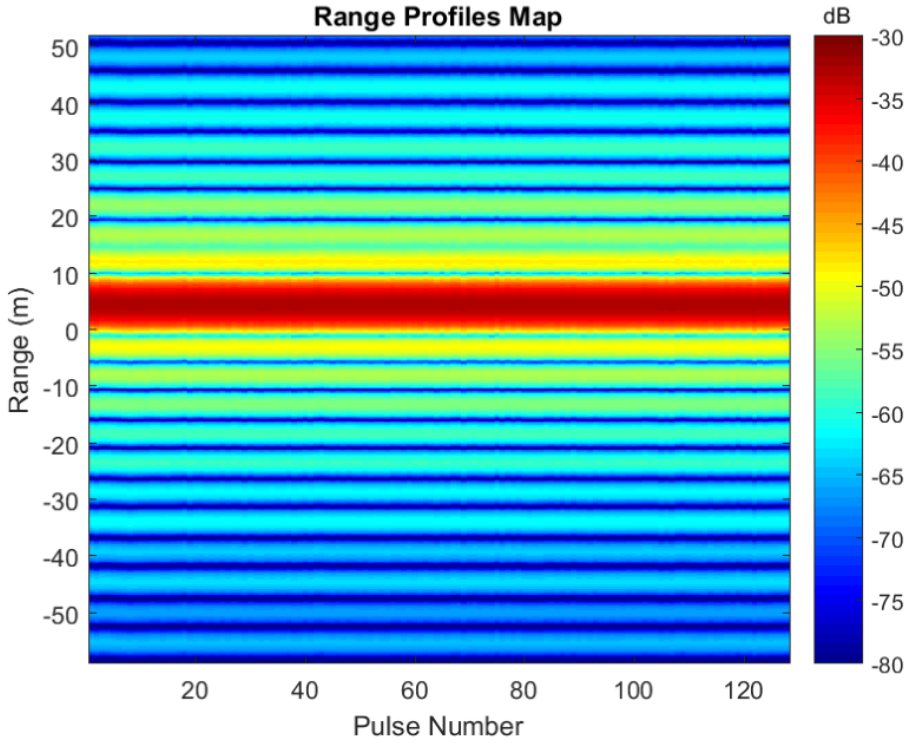

Figure 4.16: Matched Filter Output

Figure 4.18 shows a single target at a specific range and at zero Doppler/cross-range. This is to be expected without any antenna movement, and shows that the targets could not be resolved. The range resolution should again be 5 m and from Eq. (4.7),the cross-range resolution should be approximately 0.5 m which the plot labels show.

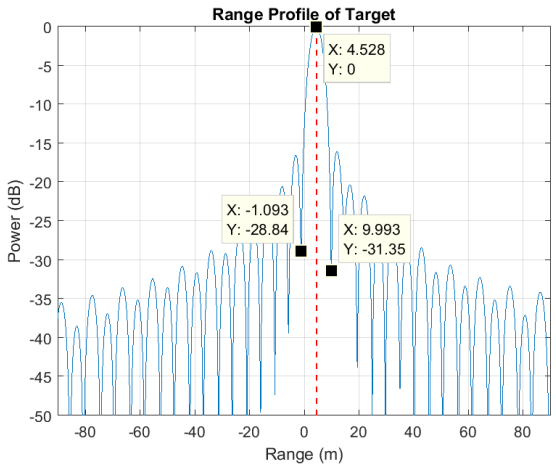

Figure 4.17: Range Profile of Targets

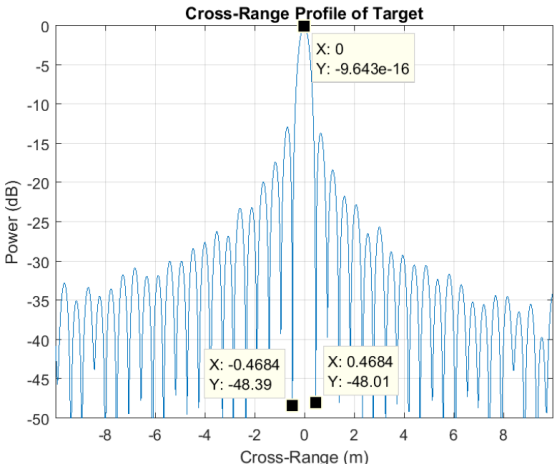

Figure 4.18: Doppler Profile of Targets

Figure 4.19 shows that due to the lack of movement of the antenna, DBS cannot be performed as there was no changing Doppler shifts during the measurement. It shows a single target (as opposed to two) at zero Doppler and a range of approximately 4.5 m, which was expected.

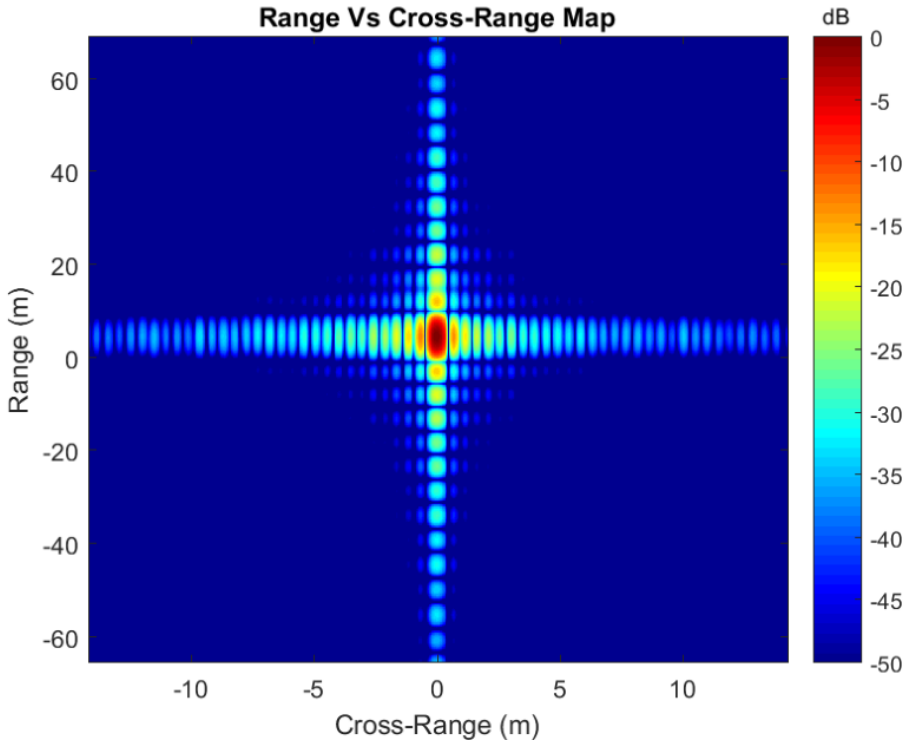

Figure 4.19: DBS Image of Two Targets When Stationary

DBS Image with Rail

The second part of the two-part measurement was to use the same layout as shown in Figure 4.15, but incorporating antenna movement to create a DBS image and resolve the two rectangular plates. Figure 4.20 shows the range profile for the two targets which are at the same range. There is a single profile at a range of approximately 4 m. The null-to-null width of the main peak is approximately 10 m, giving the 3dB range resolution of 5 m, which is expected when a bandwidth of 30 MHz is used.

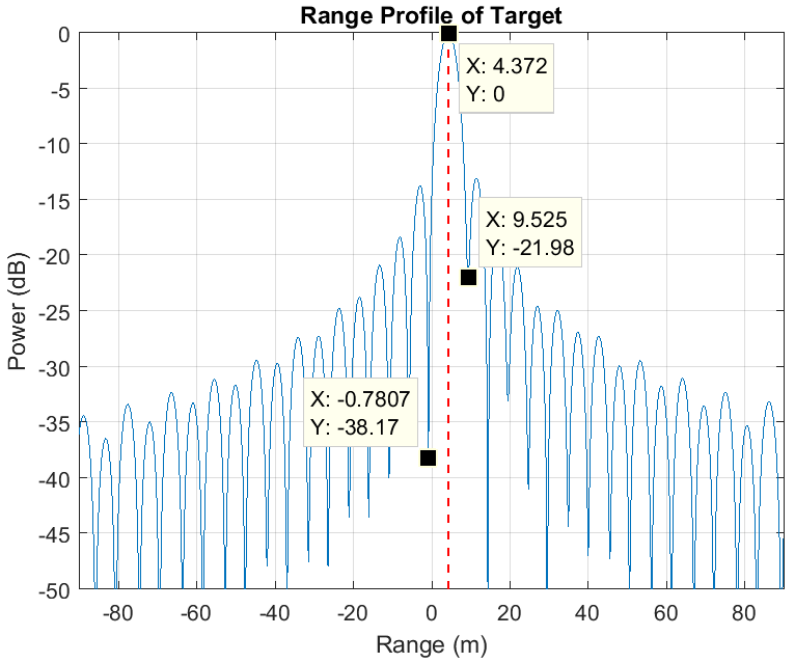

Figure 4.20: Range Profile of Target

The range profiles for all of the pulses is shown in Figure 4.21. Whilst the range profiles are constant, there is a noticeable power difference across the pulses, this is thought to be due to the incidence of the flat plates changing as the antenna moves along the rail and interference between the echoes from the two plates because the relative distance changes at each step.

Figure 4.23 shows the cross-range profiles of two targets at the corresponding cross-ranges, demonstrating that the two targets could be resolved using DBS. The two plots show the positions of the targets in cross-range at the correct location (corresponding to

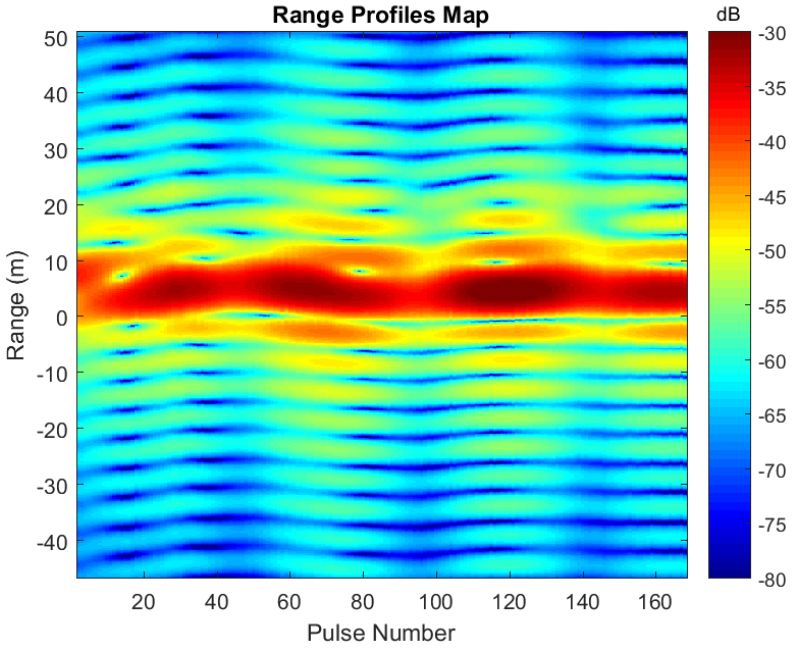

Figure 4.21: Matched Filter Output

Figure 4.15). The second plot shows the null-to-null width of the main peak is approximately 1 m, giving a 3dB cross-range resolution of approximately 0.5 m.

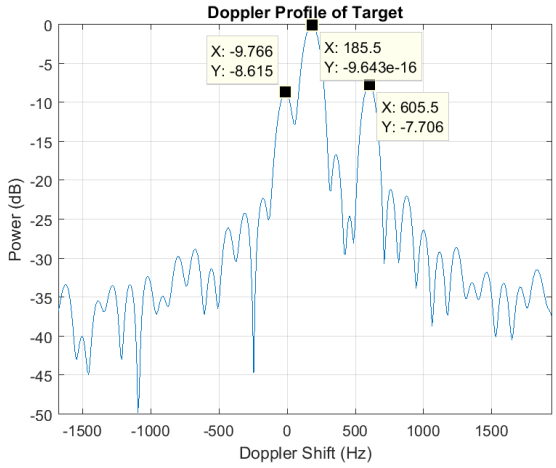

Figure 4.22: Doppler Profile of Targets

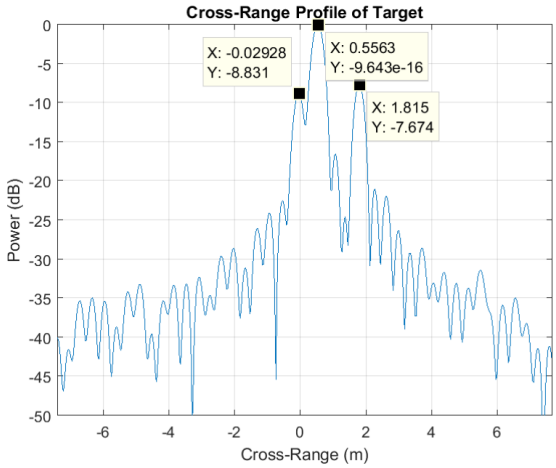

Figure 4.23: Cross-Range Profile of Targets

Figure 4.24 shows two targets at the respective cross-ranges and range profile. However, the figure also has a noticeable 'target' to the left of the two imaged plates at approximately 0 Hz and 0 m in cross-range. It is thought that this is caused by background objects in the scene (caused by immovable pipework in the laboratory and no radar ab-

sorbent material was available). Figure 4.23 shows a reasonably constant range profile but between pulses 60 and 130 there are weaker reflections at a range of approximately 10 m, which would correspond with these objects. The overall result however, demonstrates the principle of DBS. Creating an aperture and a changing Doppler shift causes a synthetic narrowing of the real beam and results in an improved cross-range resolution. This leads to targets being resolved in cross-range which the real-beam radar would not have been resolve.

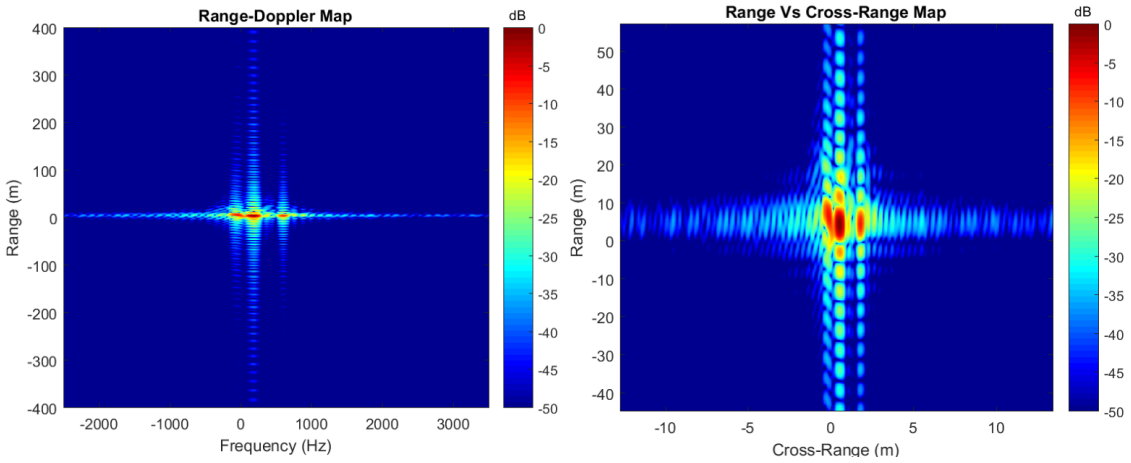

Figure 4.24: Range-Doppler Map and DBS Image of Two Targets

4.4 Conclusion

This Chapter has detailed the experimental setup used throughout the thesis and how DBS images were taken with a linear, belt-driven rail. The setup does have some limitations such as the exact horizontal distances being limited by a step resolution of 0.146 mm per step. However, this is overcome by factoring step resolution into the measurements. The results in this chapter demonstrate the effectiveness of the system to take DBS images. The DBS images of the flat plate show DBS theory in action and prove that DBS can resolve targets where a real beam cannot, by creating an aperture across the target being imaged. The setup and measurements have been built upon in the remaining chapters and used to test the jamming theory that this thesis develops.

Chapter 5

Generating False Targets Against DBS Modes

5.1 Introduction

This chapter presents two implementation methods of creating a false target in a DBS image and is one of the main novel and original contributions of this thesis. Both methods assume the jammer has the ability to create high fidelity copies of the seeker waveform, using Digital Radio Frequency Memory (DRFM). Both methods aim to create the same result of a false target in a specific location, but create the target in different ways.

The first implementation method repeats the seeker waveform with an incremental delay between pulses to create the desired time delay history of the false target. The jamming theory is developed for this method and tested with simulations in Matlab. The second implementation method uses a constant delay and applied Doppler shift to create the false target and is considered to be the easiest of the two to practically implement against narrowband signals. Whilst both methods are tested with simulations, only the second method is tested with practical experiments, due to it being more feasible to implement in practice than the first method.

The developed theory and experimental results show that false targets can be placed at

desired locations within the seeker DBS image, providing that the jammer has knowledge of the trajectory of the seeker and the ability to reproduce the waveforms of the seeker.

5.2 General Geometry and Signal Model

It was proved in Chapter 3 that there must be an offset angle between the platform and the target to perform DBS. The scenario in this chapter therefore studies an anti-ship missile, flying at an offset angle to the target. DBS is often used in an area search mode and there are different search modes it can use to acquire targets. The modes are not discussed or detailed in this thesis, but it is assumed that the seeker is using a 'spotlight' search mode. Spotlight is used in SAR and is essentially steering the illuminating pattern (either mechanically or electronically), to image a constant target area over the Coherent Processing Interval (CPI) [Stimson et al., 2014]. Therefore, it is assumed that the jammer is at the centre of the target area and is illuminated for the entire CPI, for each scenario presented in this thesis.

The geometry and signal model is now presented. Consider a missile seeker, transmitting a signal

$$s_T(t) = s(t)e^{i2\pi f_c t} \tag{5.1}$$

whilst flying along the x-axis of a 2D Cartesian coordinate system with dynamics

$$x(t) = Vt \tag{5.2}$$

and constant velocity V, as shown in Figure 5.1, where $s(t)$ is an arbitrary complex envelope of the waveform and f_c is the carrier frequency.

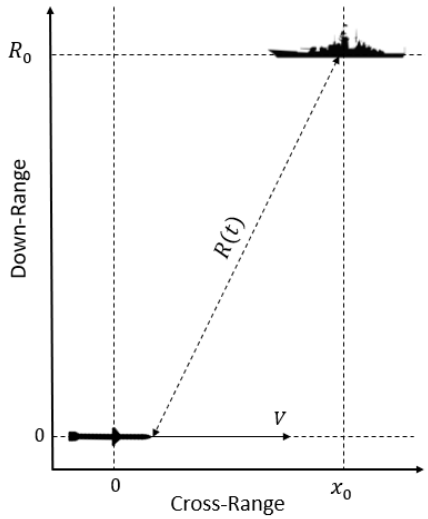

Figure 5.1: Missile Reference Frame

The signal reflected from a target located at a slant range R_0 and cross range x_0, can be expressed as

$$s_R(t) = \gamma_R s(t - \tau(t)) e^{-i2\pi f_c \tau(t)} e^{i2\pi f_c t} \tag{5.3}$$

where

$$\tau(t) = \frac{2R(t)}{c} \tag{5.4}$$

is the echo time delay and

$$R(t) = \sqrt{(x_0 - Vt)^2 + {R_0}^2} \tag{5.5}$$

is the instantaneous target distance from the missile. Using algebraic manipulation, $R(t)$ can be redefined as

$$\sqrt{(x_0 - Vt)^2 + {R_0}^2} = R_0 \left(1 + \frac{{x_0}^2}{{R_0}^2} - \frac{2Vtx_0}{{R_0}^2} + \frac{(Vt)^2}{{R_0}^2}\right)^{\frac{1}{2}} \tag{5.6}$$

For $R_0 >> x_0$ and $t \approx 0$, $\frac{{x_0}^2}{{R_0}^2}$ and $\frac{(Vt)^2}{{R_0}^2}$ can be approximated to zero. This gives

$$R(t) = R_0 \left(1 + \frac{{x_0}^2}{{R_0}^2} - \frac{2Vtx_0}{{R_0}^2} + \frac{(Vt)^2}{{R_0}^2}\right)^{\frac{1}{2}} \simeq R_0 \left(1 - \frac{2Vtx_0}{{R_0}^2}\right)^{\frac{1}{2}} \tag{5.7}$$

For $R_0 >> x_0$ and $t \approx 0$

$$R(t) \simeq R_0 \sqrt{1 - \frac{2Vtx_0}{{R_0}^2}} \tag{5.8}$$

which after a first order Taylor approximation about $t = 0$ leads to

$$R(t) = R_0 - \frac{Vx_0t}{R_0} \tag{5.9}$$

and

$$\tau(t) = \frac{2R_0}{c} - \frac{2Vx_0t}{cR_0} \tag{5.10}$$

Finally, the signal received by the seeker after IQ demodulation can be expressed as

$$s_R(t) = \gamma_R s(t - \tau(t)) e^{-i\frac{4\pi}{\lambda}R_0} e^{i2\pi\frac{2Vx_0}{\lambda R_0}t} \tag{5.11}$$

which after the narrowband approximation [Van Trees, 2001] becomes

$$s_R(t) = \gamma_R s\left(t - \frac{2R_0}{c}\right) e^{-i\frac{4\pi}{\lambda}R_0} e^{i2\pi\frac{2Vx_0}{\lambda R_0}t} \tag{5.12}$$

where γ_R is the two-way attenuation factor. The received signal is a delayed copy of the transmitted signal shifted in Doppler of $f_D = \frac{2Vx_0}{\lambda R_0}$. DBS measures the Doppler shift and obtains an estimate of the slant range to find the cross-range coordinate of the target.

5.3 Jamming Theory and Method

This section presents two implementation methods of creating a false target in a DBS image. The first is by adding an incremental time delay to the waveform and the second is a delay and Doppler shift to create the false target.

5.3.1 Varying Time Delay Method

This sub-section details how to create false targets by using a repeat jamming method with a time-varying delay. As shown in Figure 5.2, the propagation distance, $R(t)$, is time varying due to the movement of the missile. This means that the time delay for an echo reflection will also change with time due to the movement of the missile. The changing delay is what creates the time varying Doppler shift that enables DBS to be used.

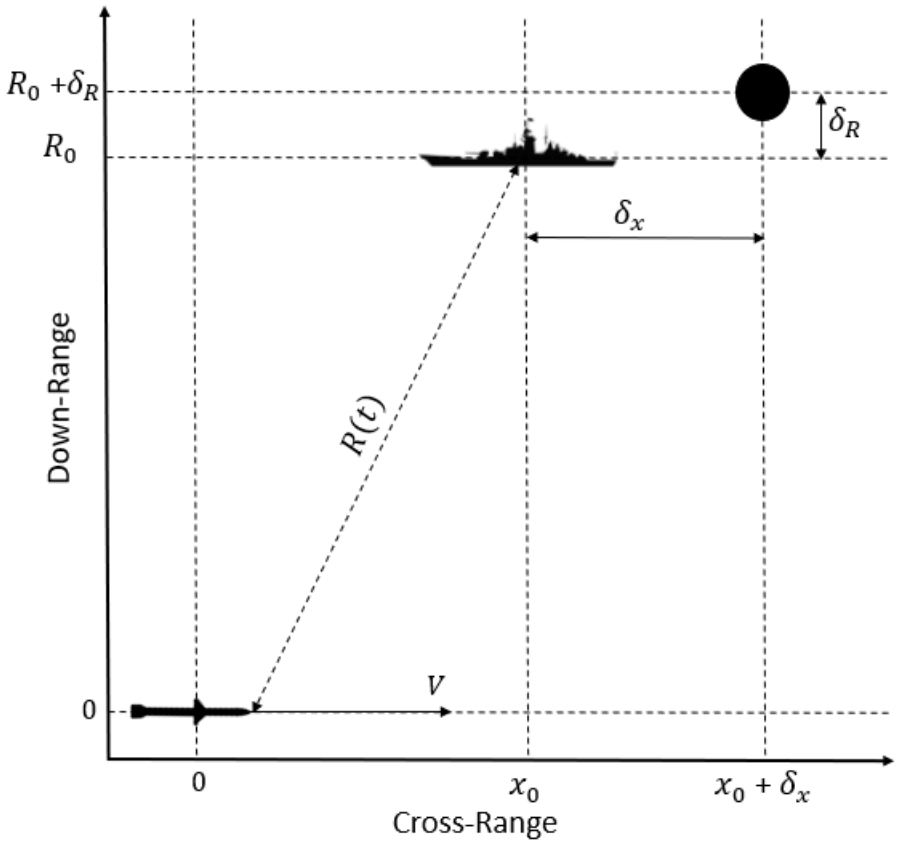

Figure 5.2: Missile Reference Frame With Jammer

The presented theory shows how a jammer can create the time-delay history for a false target. This is done by repeating the seeker waveform but with an incremental delay, $\tau_j(t)$. This is to mimic the delay a false target would have, if it was located at the location the jammer is trying to represent. A schematic of the jamming scheme is shown in Figure 5.3

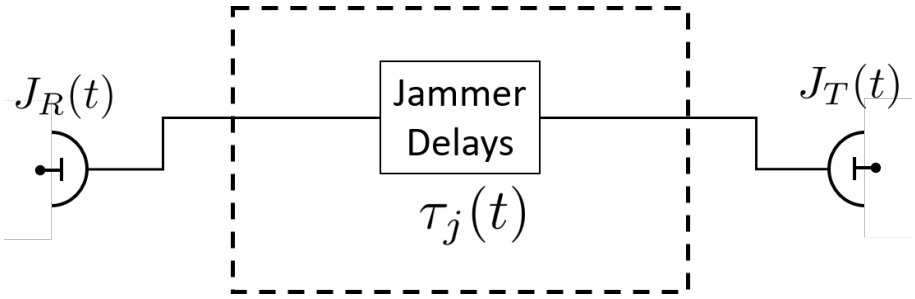

Figure 5.3: Jamming Block Diagram

From Eq. (5.12) , an ideal target located at $(x_0+\delta_x, R_0+\delta_R)$ would generate an echo signal

$$s_R(t) = \gamma_R s\left(t - \frac{2(R_0+\delta_R)}{c}\right) \times \exp\left(-i4\pi\frac{(R_0+\delta_R)}{\lambda}\right) \exp\left(i2\pi\frac{2V(x_0+\delta_x)t}{\lambda(R_0+\delta_R)}\right) \tag{5.13}$$

where from Eq. (3.92), the total time delay $\tau_T(t)$ is

$$\tau_T(t) = \frac{2(R_0+\delta_R)}{c} - \frac{2V(x_0+\delta_x)t}{c(R_0+\delta_R)} \tag{5.14}$$

This means that the value of $\tau_j(t)$ must be such that when applied to the seeker waveform, the seeker receives the signal in Eq. (5.13). Using Eq. (5.12) and Eq. (5.13), an expression for $\tau_j(t)$ can be defined as

$$\tau(t) + \tau_j(t) = \tau_T(t) \tag{5.15}$$

which leads to

$$\tau_j(t) = \frac{2(R_0+\delta_R)}{c} - \frac{2V(x_0+\delta_x)t}{c(R_0+\delta_R)} - \frac{2R_0}{c} + \frac{2Vx_0t}{cR_0} \tag{5.16}$$

and gives the final result as

$$\tau_j(t) = \frac{2\delta_R}{c} - \frac{2V(x_0+\delta_x)t}{c(R_0+\delta_R)} + \frac{2Vx_0t}{cR_0} = \frac{2\delta_R}{c} + \frac{2\beta_j t}{c} - \frac{2\beta t}{c} \tag{5.17}$$

where

$$\frac{2\beta_j t}{c} = -\frac{2V(x_0+\delta_x)t}{c(R_0+\delta_R)} \tag{5.18}$$

From the scenario in Figure 5.2, let the transmitted signal $s_T(t)$ from the seeker be the same as Eq. (5.1), where $s(t)$ is an arbitrary complex envelope of the waveform. Following the geometry of Figure 5.2, whilst propagating towards the jammer, $s_T(t)$ will experience a time delay corresponding to the distance $R(t)$. From Eq. (3.92), the delay $s_T(t)$ experiences is $\frac{R(t-\tau(t))}{c}$ to give

$$\tau(t) = \frac{R(t-\tau(t))}{c} = \frac{R_0}{c} + \frac{\beta}{c}[t-\tau(t)] \tag{5.19}$$

with

$$\beta = -\frac{Vx_0}{R_0} \tag{5.20}$$

Showing full workings, $\tau(t)$ can be expressed as

$$c\tau(t) = R_0 + \beta t - \beta\tau(t) \tag{5.21}$$

$$\tau(t)(c+\beta) = R_0 + \beta t \tag{5.22}$$

$$\tau(t) = \frac{R_0}{(c+\beta)} + \frac{\beta t}{(c+\beta)} \tag{5.23}$$

The signal received by the jammer is therefore

$$j_R(t) = \gamma s_T\left(t - \frac{R_0}{(c+\beta)} - \frac{\beta t}{(c+\beta)}\right) \tag{5.24}$$

where γ is a one-way attenuation factor. The jammer would then delay $j_R(t)$ by $\tau_j(t)$, to

give an additive range component and induce a Doppler shift to then transmit

$$j_T(t) = \gamma_J s_T \left(\frac{c}{(c+\beta)} t - \frac{c\tau_j(t)}{(c+\beta)} - \frac{R_0}{(c+\beta)} \right) \tag{5.25}$$

where γ_J is the jammer gain factor. The second leg of propagation back towards the seeker has the delay of

$$\tau'(t) = \frac{R(t)}{c} = \frac{R_0}{c} + \frac{\beta t}{c} \tag{5.26}$$

giving the resultant jamming signal received by the seeker as

$$s_R(t) = \gamma_R s_T \left(\frac{c}{(c+\beta)} (t - \tau'(t)) - \frac{c\tau_j(t-\tau'(t))}{(c+\beta)} - \frac{R_0}{(c+\beta)} \right) \tag{5.27}$$

The term $\frac{c}{(c+\beta)}(t-\tau'(t))$ can be simplified to

$$\frac{c}{(c+\beta)}(t-\tau'(t)) = \frac{c}{(c+\beta)} \left[\left(1 - \frac{\beta}{c} \right) t - \frac{R_0}{c} \right] = \frac{c-\beta}{c+\beta} t - \frac{R_0}{c+\beta} \tag{5.28}$$

From Eq. (5.17), expanding $\tau_j(t-\tau'(t))$ gives

$$\tau_j(t-\tau'(t)) = \frac{2\delta_R}{c} - \left[\frac{2\beta}{c} - \frac{2\beta_j}{c} \right] \left[t - \frac{R_0}{c} - \frac{\beta t}{c} \right] \tag{5.29}$$

$$= \frac{2\delta_R}{c} - \frac{2\beta t}{c} + \frac{2\beta_j t}{c} - \frac{2R_0\beta_j}{c^2} - \frac{2\beta_j\beta t}{c^2} + \frac{2R_0\beta}{c^2} - \frac{2\beta^2 t}{c^2} \tag{5.30}$$

When $R_0 > x_0$, the terms with the denominator of c^2 can be approximated to zero. Therefore,

$$\tau_j(t-\tau'(t)) = \frac{2}{c} \left[\delta_R + \beta_j t - \beta t \right] \tag{5.31}$$

This gives the received jamming signal as

$$s_R(t) = \gamma_R s_T \left(\left(\frac{c-\beta}{c+\beta} \right) t - \frac{c}{(c+\beta)} \left[\frac{2(R_0+\delta_R)}{c} + \frac{2\beta_j t}{c} - \frac{2\beta t}{c} \right] \right) \tag{5.32}$$

After replacing the expression of s_T(t), the signal received at the seeker can be expressed as

$$\begin{aligned} s_R(t) &= \gamma_R s \left(\frac{c-\beta}{c+\beta} t - \frac{c}{(c+\beta)} \left[\frac{2(R_0+\delta_R)}{c} \right] \right) \\ &\times \exp\left(i2\pi f_c \frac{c-\beta}{c+\beta} t \right) \exp\left(-i2\pi f_c \frac{c}{(c+\beta)} \left[\frac{2(R_0+\delta_R)}{c} + \frac{2\beta_j t}{c} - \frac{2\beta t}{c} \right] \right) \end{aligned} \tag{5.33}$$

which after down-conversion becomes

$$\begin{aligned} s_R(t) &= \gamma_R s \left(\frac{c-\beta}{c+\beta} t - \frac{c}{(c+\beta)} \left[\frac{2(R_0+\delta_R)}{c} \right] \right) \\ &\times \exp\left(-i2\pi f_c \frac{2\beta}{c+\beta} t \right) \exp\left(-i2\pi f_c \frac{c}{(c+\beta)} \left[\frac{2(R_0+\delta_R)}{c} + \frac{2\beta_j t}{c} - \frac{2\beta t}{c} \right] \right) \end{aligned} \tag{5.34}$$

When $\beta << c$, the terms $\frac{c}{c+\beta} \simeq 1$, $\frac{2\beta}{c+\beta} \simeq \frac{2\beta}{c}$, $\frac{c-\beta}{c+\beta} \simeq 1$ and after the narrowband approximation [Van Trees, 2001] the final waveform at the seeker becomes

$$s_R(t) = \hat{\gamma}_R s \left(t - \frac{2(R_0+\delta_R)}{c} \right) \exp\left(-i2\pi f_c \frac{2\beta_j}{c} t \right) \tag{5.35}$$

where all constant phase terms have been included in the parameter $\hat{\gamma}_R$.

False Target Simulation

The purpose of this scenario is to demonstrate how to perfectly place a false target in the desired location, assuming all required parameters are known. In practice, incorrect estimations of the seeker waveforms or inaccuracies in the trajectory or velocity of the missile, will lead to the false target not being exactly where the jammer intends to insert it. This issue is the main topic of Chapter 6 and will be presented and discussed there. The simulation was undertaken using the geometry of Figure 5.2 and Table 5.1. The miss distances chosen would be dependant on the scenario and dynamics of the battlespace, but were nominally 200m in downrange an 300m in cross-range for this particular scenario.

Table 5.1: Example Scenario Variables

Variable	Seeker	False Target	Miss Distance
Down-range (km)	14 (R_0)	14.2 ($R_0+\delta_R$)	0.2 (δ_R)
Cross-range (km)	0.5 (x_0)	0.8 ($x_0+\delta_x$)	0.3 (δ_x)

For the scenarios in this section, a pulsed Linear Frequency Modulated (LFM) waveform was used. From Eq. (5.1), this means $S_T(t)$ is equal to

$$s_T(t) = \sum_{m=0}^{M-1} s(t - m\text{PRI}) \tag{5.36}$$

where

$$s(t) = e^{i\pi\gamma t^2} Rect\left(\frac{t}{\tau}\right) \tag{5.37}$$

and

$$Rect\left(\frac{t}{\tau}\right) = \begin{cases} 1, & -\frac{\tau}{2} < t < \frac{\tau}{2} \\ 0, & \text{Elsewhere} \end{cases} \tag{5.38}$$

The waveform was constructed with the notation of negative time to maintain the centre frequency of the chirp at the carrier frequency of the radar. Table 5.2 shows the signal parameters used for the scenario.

Table 5.2: Simulation Variables

Variable	Symbol	Value
Missile Velocity	V	270 m/s
Carrier Frequency	f_c	36 GHz
Bandwidth	B	40 MHz
Pulse Width	τ	3 μs
Pulse Repetition Frequency	PRF	10 kHz
Number of Pulses	M	64
Dwell Time	t_d	6.4 ms
Doppler Resolution	δ_f	156.25 Hz

The values of Table 5.2 were chosen to best represent the seeker threat, obtained from unclassified literature. The operating frequency of 36 GHz is within the North Atlantic Treaty Organisation (NATO) K band. The frequency of 36 GHz is often used by seekers as it enables smaller beamwidths than using lower frequencies. As a general purpose rule, the higher the frequency, the narrower the beamwidth. There is a trade-off between beamwidth and frequency however, as the higher the frequency, the higher the atmospheric attenuation, generally. This means that to maintain the same detection range, more power (than the seeker could potentially generate) is generally required as frequency increases. There are peaks and troughs along this trend though and 36 GHz falls into a lull in atmospheric attenuation.

The waveforms and frequency spectrums for the scenario are shown in Figures 5.4 and 5.5. The figures show LFM pulses with a pulse width of 3 μs and a bandwidth of 40 MHz.

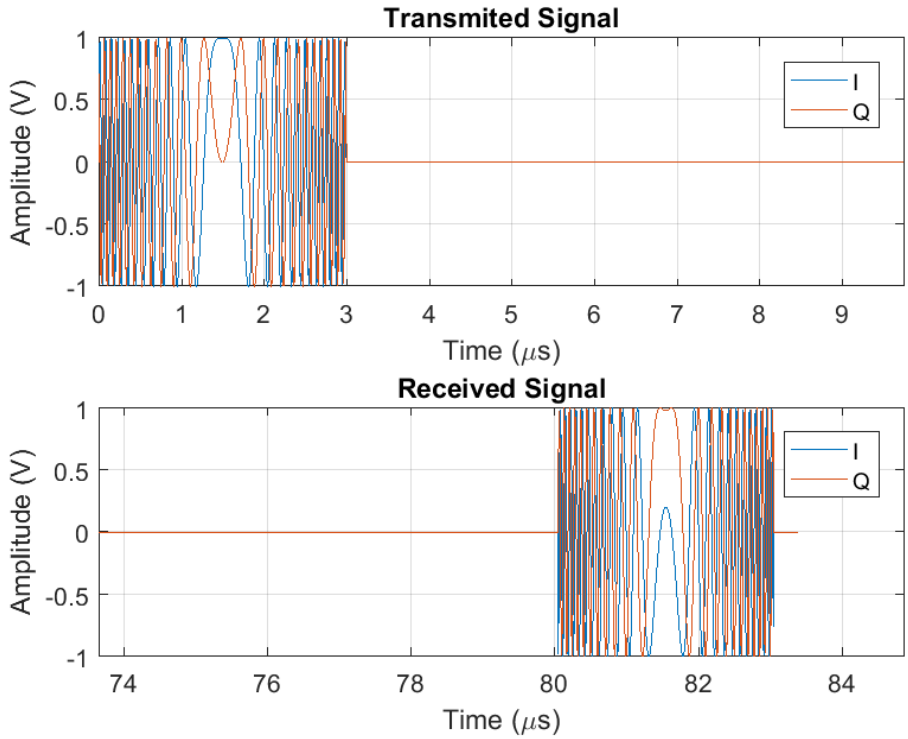

Figure 5.4: Transmitted and Received Waveforms

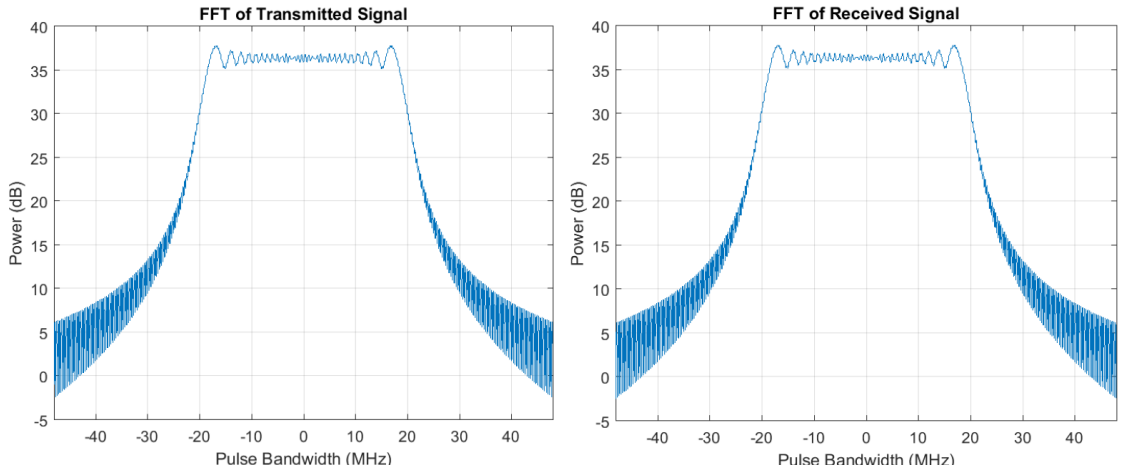

Figure 5.5: Frequency Spectrum of Transmitted and Received Waveforms

Using the method described in the previous section and parameters in Tables 5.1 and 5.2, a false target could be placed at a desired location in the DBS image from the seeker. Figure 5.6 shows the range and cross-range profiles for the false target. With a bandwidth of 40 MHz, the null-to-null width of the main lobe should be 7.5 m to give a 3 dB range-resolution of 3.75 m, which the plot labels show. From Table 5.2, the Doppler resolution

is 156.25 Hz. With the geometry in Figure 5.2 and values in Table 5.1, the cross-range resolution [Hodgson & Lee, 2003, Farooq & Limebeer, 2007, Farooq & N. Limebeer, 2002] at the jammer position is

$$\Delta_{CR} = \frac{\lambda R_0}{2VT_{dwell}\sin(\theta_\lambda)} = \frac{0.0083 \times 14000}{2 \times 270 \times 0.0064 \times \sin(87.95^\circ)} = 33.64 \text{ m} \tag{5.39}$$

which is demonstrated in the cross-range profile in Figure 5.6.

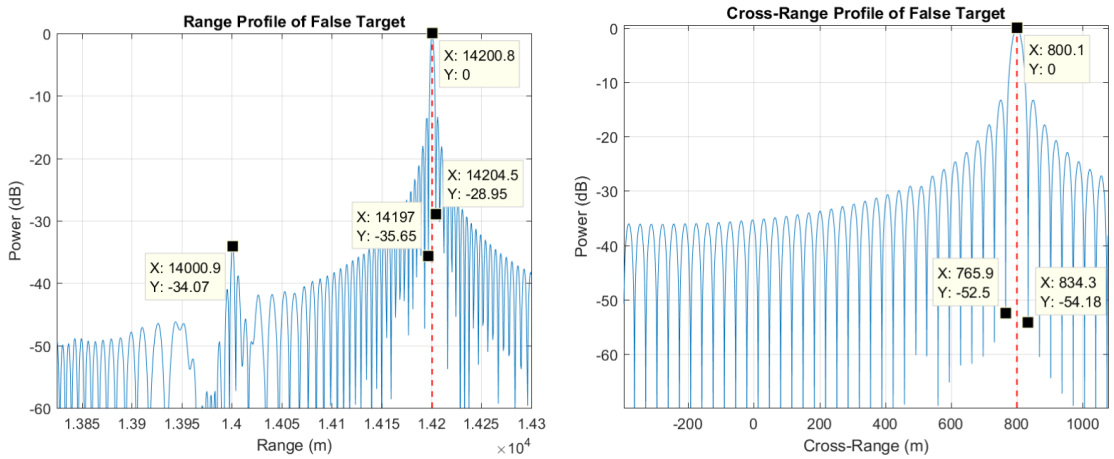

Figure 5.6: Range and Doppler Slices of False Target

Figure 5.7 shows the range-Doppler map and DBS image for the scenario. For this scenario, the expected Doppler shift for the false target is

$$f_d = \frac{2Vx_0}{\lambda R_0} = 3665.37 \text{ Hz} \tag{5.40}$$

which the range-Doppler map shows. The DBS image shows the echo and false targets at the correct position of 14.2 km in range, 0.8 km in cross-range.

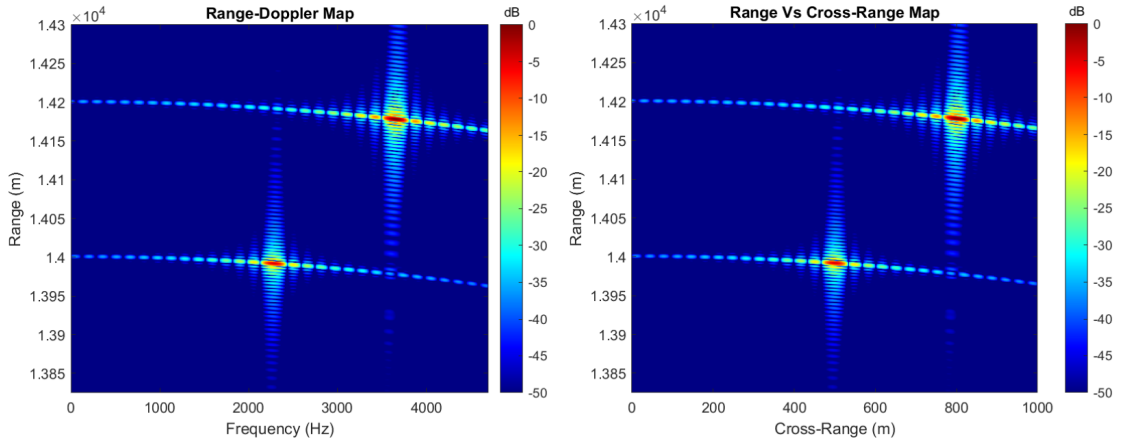

Figure 5.7: Range-Doppler Map and DBS Image of Scenario

For the geometry in Table 5.1, the time-varying delay time of the jammer, calculated by Eq. (5.17), is shown in Figure 5.8. For a typical scenario with the geometry in Table 5.1, it can be seen that the largest component of the equation is the constant $\frac{\delta_R}{c}$ and the time-varying components will be small, in the order of picoseconds as shown in Figure 5.9. For example, the difference between the time delay for each pulse in this scenario is 2.3 picoseconds. It is these slight changes which are critical to create the changing phase, to create the false target in the DBS image. However, such precise timings are difficult to achieve in practice.

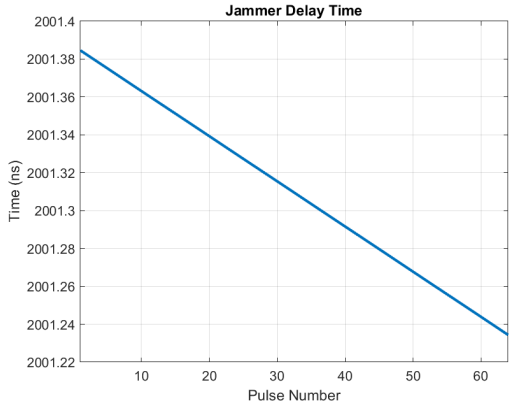

Figure 5.8: Total Jammer Hold On Time for Each Pulse

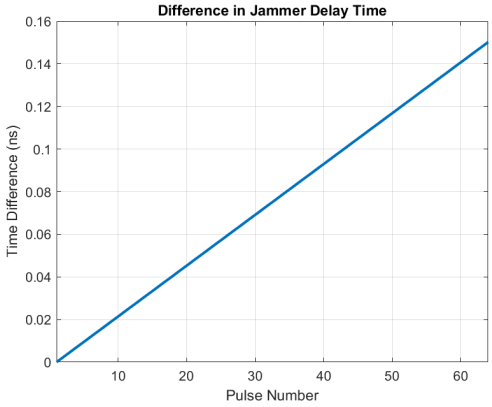

Figure 5.9: Difference of Jammer Hold On Time Relative To First Pulse

Changing the Shape of the Target

This scenario is similar to the first jamming scenario, except that there are multiple scatterers in the scene and the false target (denoted by 'FT') is placed between targets 'T2' and 'T3' in cross-range. Figure 5.10 shows the layout of this principle. For this scenario, it is assumed that the jammer is located at 'T1' with the co-ordinates (x_0, R_0). If the targets are placed close enough to each other that they can only just be resolved at their respective ranges, placing a target between them in cross range would mask the fact that there are two targets and instead create one larger target. The simulation is a simplified example, but the purpose of it is to show that the jammer can be used to change features of an existing target by placing a false target in exactly the correct place.

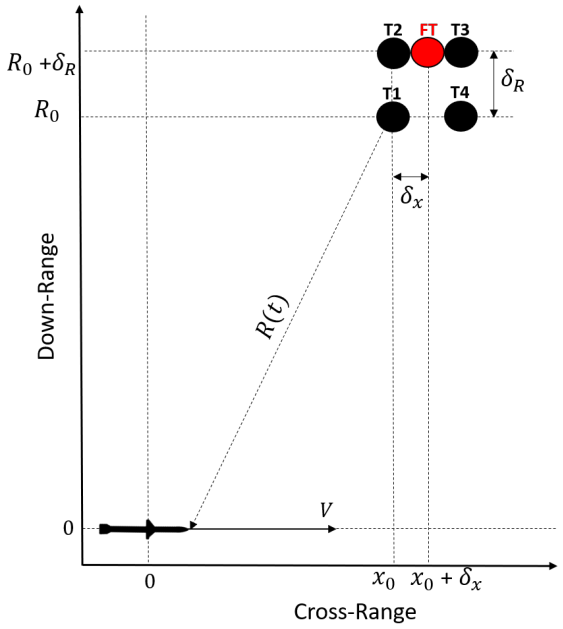

Figure 5.10: Missile Reference Frame With Jammer

Table 5.3 shows the location of the targets with the geometry of the scenario being almost the same as the first jamming scenario. From the Doppler resolution listed in Table 5.2 and by using Eq. (5.39), the cross-range resolution is 33.64 m. Therefore, by placing a false target with spacing less than the cross-range resolution, the targets will not be able to be resolve and will form into single, larger target.

Table 5.3: Jamming Scenario Two Target Locations

Target	R_0 (m)	x_0 (m)
1	14000	500
2	14010	500
False Target	14010	517
3	14010	534
4	14000	534

Figures 5.11 and 5.12 show the transmitted and received waveform with a pulse width of 3 μs as well as a bandwidth of 40 MHz.

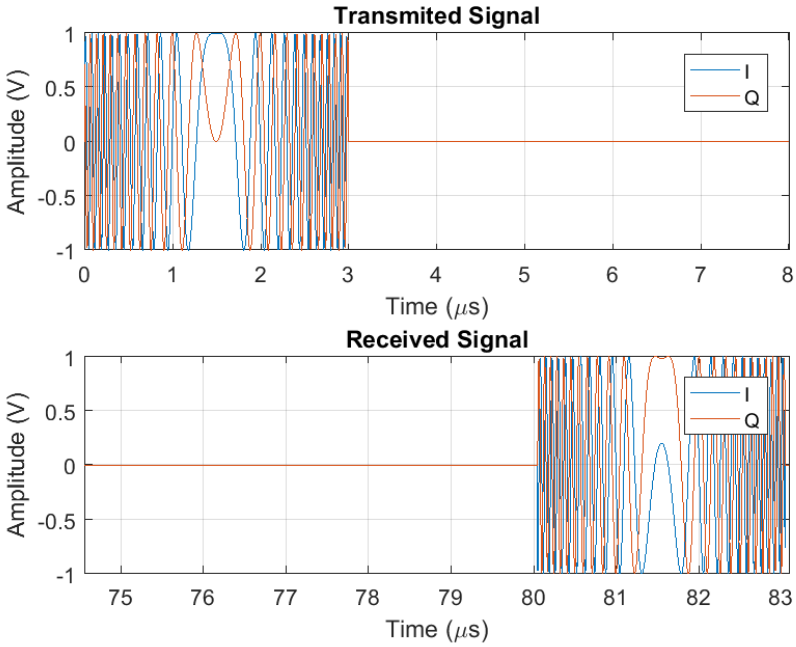

Figure 5.11: Transmitted and Received Waveforms

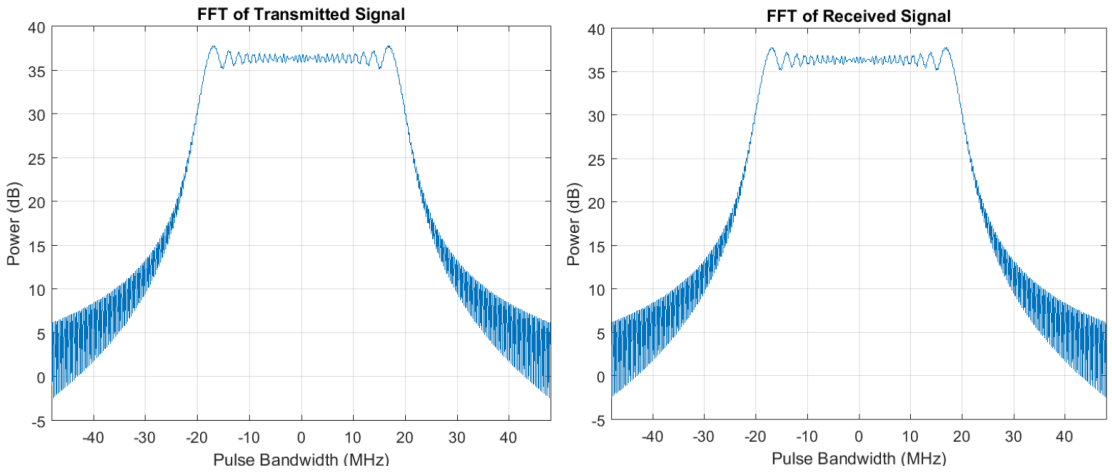

Figure 5.12: Frequency Spectrum of Transmitted and Received Waveforms

Figures 5.13 and 5.14 show the results of the simulation. Targets Two and Three cannot be resolved using the existing DBS method. The purpose of this simulation is to show that if the surrounding geometry of targets, CPI of the seeker and trajectory of the seeker is known, the jammer could attempt to change the shape of existing targets, to make smaller targets appear larger in size and possibly more desirable to the seeker.

The range profile in Figure 5.13 shows two profiles in range, which is expected as the targets were separated by a distance greater than the range resolution of 3.75 m. With a cross-range resolution of 33.64 m, the cross-range profile in Figure 5.13 shows only one, large target as the target was placed in such a way that it could not be resolved between the surrounding echoes.

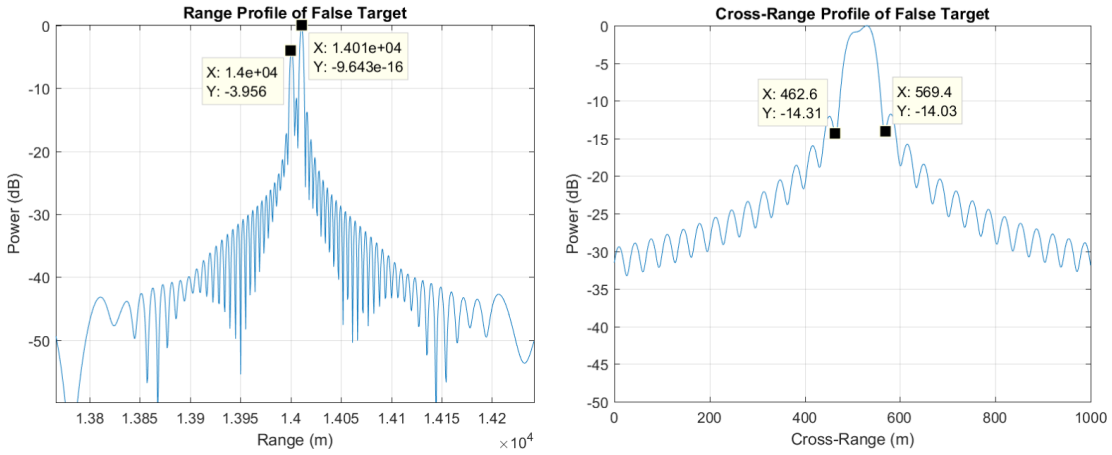

Figure 5.13: Range and Doppler Slices of False Target

The final result in Figure 5.14 shows only three targets, two echoes and one large target caused by the jammer accurately placing a false target so that it could not be resolved between surrounding echoes.

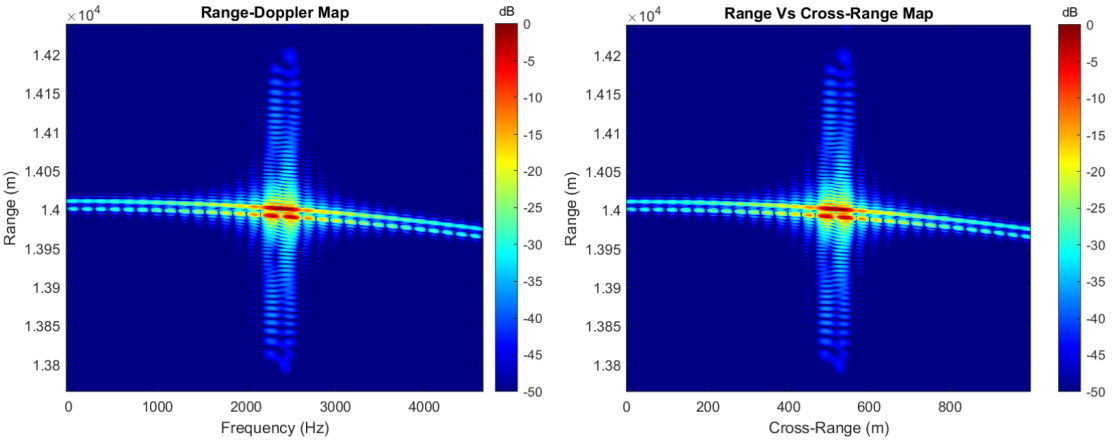

Figure 5.14: Range-Doppler Map and DBS Image of Scenario

5.3.2 Delay and Modification

In this sub-section, the jamming scheme outlined in Figure 5.15 is proposed to enable the jammer to generate false targets, by applying a constant time delay τ_j and a Doppler shift $f_J = \alpha f_D$ to the intercepted waveform. The goal of the jammer is to calculate τ_j and the parameter α, based on the received signal, to place the false target at the desired miss-distance in downrange and cross-range. This is the second of the two implementation methods presented in this chapter. This method is thought to be easier to be implemented in practice as it does not require such precise timings, due to the constant time delay used.

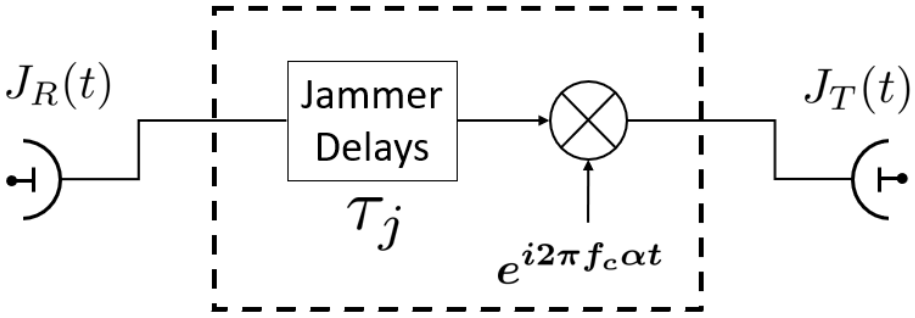

Figure 5.15: Jamming Block Diagram

Let the transmitted signal $s_T(t)$ from the seeker be the same as Eq. (5.1) where $s(t)$ is an arbitrary complex envelope of the waveform. Whilst propagating towards the jammer, $s_T(t)$ will experience a time delay

$$\tau(t) = \frac{R(t-\tau(t))}{c} = \frac{R_0}{c} + \frac{\beta}{c}[t-\tau(t)] = \frac{R_0}{(c+\beta)} + \frac{\beta t}{(c+\beta)} \tag{5.41}$$

with

$$\beta = -\frac{V x_0}{R_0} \tag{5.42}$$

The signal received by the jammer is therefore

$$j_R(t) = \gamma s_T\left(t - \frac{R_0}{(c+\beta)} - \frac{\beta t}{(c+\beta)}\right) \tag{5.43}$$

where γ is the one-way attenutation factor. The jammer would then delay $j_R(t)$ by τ_j, to give an additive range component, and induce a Doppler shift to then transmit

$$j_T(t) = \gamma_j s_T\left(\frac{c}{(c+\beta)}t - \frac{c\tau_j}{(c+\beta)} - \frac{R_0}{(c+\beta)}\right) \times \exp(i2\pi f_c \alpha t) \tag{5.44}$$

where γ_j is the jammer gain factor. The second leg of propagation back towards the seeker has the delay of

$$\tau'(t) = \frac{R(t)}{c} = \frac{R_0}{c} + \frac{\beta t}{c} \tag{5.45}$$

This gives the resulting jamming signal to be

$$\begin{aligned} s_R(t) = \gamma_R s_T &\left(\frac{c}{(c+\beta)}[t-\tau'(t)] - \frac{c\tau_j + R_0}{(c+\beta)}\right) \\ &\times \exp\Big(i2\pi f_c \alpha [t-\tau'(t]\Big) \end{aligned} \tag{5.46}$$

which, after replacing the value of $\tau'(t)$ in Eq. (5.45), can be written as

$$\begin{aligned} s_R(t) = \gamma_R s_T &\left(\frac{c-\beta}{(c+\beta)}t - \frac{c}{(c+\beta)}\left[\frac{2R_0}{c} + \tau_j\right]\right) \\ &\times \exp\Big(i2\pi f_c \alpha \frac{c-\beta}{c}t\Big) \exp\Big(-i2\pi f_c \alpha \frac{R_0}{c}\Big) \end{aligned} \tag{5.47}$$

After replacing the expression of s_T(t), the signal received at the seeker can be expressed as

$$\begin{aligned} s_R(t) = \gamma_R s &\left(\frac{c-\beta}{c+\beta}t - \frac{c}{(c+\beta)}\left[\frac{2R_0}{c} + \tau_j\right]\right) \\ &\times \exp\left(i2\pi f_c \frac{c-\beta}{c+\beta}t\right) \exp\left(-i2\pi f_c \frac{c}{(c+\beta)}\left[\frac{2R_0}{c} + \tau_j\right]\right) \\ &\times \exp\Big(i2\pi f_c \alpha \frac{c-\beta}{c}t\Big) \exp\Big(-i2\pi f_c \alpha \frac{R_0}{c}\Big) \end{aligned} \tag{5.48}$$

which after down-conversion becomes

$$\begin{aligned} s_R(t) &= \gamma_R s\left(\frac{c-\beta}{c+\beta}t - \frac{c}{(c+\beta)}\left[\frac{2R_0}{c}+\tau_j\right]\right) \\ &\times \exp\left(-i2\pi f_c\frac{2\beta}{c+\beta}t\right)\exp\left(-i2\pi f_c\frac{c}{(c+\beta)}\left[\frac{2R_0}{c}+\tau_j\right]\right) \\ &\times \exp\left(i2\pi f_c\alpha\frac{c-\beta}{c}t\right)\exp\left(-i2\pi f_c\alpha\frac{R_0}{c}\right) \end{aligned} \tag{5.49}$$

When $\beta << c$, the terms $\frac{c}{c+\beta} \simeq 1$, $\frac{2\beta}{c+\beta} \simeq \frac{2\beta}{c}$, $\frac{c-\beta}{c} \simeq 1$ and after the narrowband approximation [Van Trees, 2001], the final waveform at the seeker becomes

$$\begin{aligned} s_R(t) &= \hat{\gamma}_R s\left(t - \frac{2R_0}{c} - \tau_j\right) \\ &\times \exp\left(-i2\pi f_c\frac{2\beta}{c}t\right)\exp\left(i2\pi f_c\alpha t\right) \end{aligned} \tag{5.50}$$

where all constant phase terms have been included in the parameter $\hat{\gamma}_R$. From Eq. (5.12), an ideal target located at $(x_0+\delta_x, R_0+\delta_R)$ would generate an echo signal

$$s_R(t) = \gamma_R s\left(t - \frac{2(R_0+\delta_R)}{c}\right) \times \exp\left(-i4\pi\frac{(R_0+\delta_R)}{\lambda}\right)\exp\left(i2\pi\frac{2V(x_0+\delta_x)t}{\lambda(R_0+\delta_R)}\right) \tag{5.51}$$

In order for the jammer to create the perfect false target, the value of τ_j and α must be such that the total time delay and Doppler shift at the seeker in Eq. (5.50) are the same as that for Eq. (5.51).

If

$$\beta_J = -\frac{V(x_0+\delta_x)}{(R_0+\delta_R)} \tag{5.52}$$

then α can be calculated by imposing the Doppler equality

$$-f_c\frac{2\beta}{c} + f_c\alpha = -f_c\frac{2\beta_j}{c} \tag{5.53}$$

which leads to the final result

$$\alpha = \frac{2\beta}{c} - \frac{2\beta_J}{c} = \frac{2V(x_0+\delta_x)}{c(R_0+\delta_R)} - \frac{2Vx_0}{cR_0} \tag{5.54}$$

Similarly, it is straightforward to show that

$$\tau_j = \frac{2\delta_r}{c} \tag{5.55}$$

These results show that in order to generate a false target in the desired cross-range location, the jammer ideally needs perfect knowledge of its position with respect to the seeker.

Pulsed DBS

For a pulsed DBS system, let

$$s_T(t) = \sum_{m=0}^{M-1} s(t - mPRI)\exp(i2\pi f_c t) \tag{5.56}$$

consisting of M pulses of duration τ. Following the result obtained in Eq. (5.50) and by using the jamming scheme in Figure 5.15, the pulse train received by the seeker would be

$$\begin{aligned} s_R(t) = \hat{\gamma}_R \sum_{m=0}^{M-1} s\left(t - mPRI - \frac{2R_0}{c} - \tau_j\right) \\ \times \exp\left(-i2\pi f_c \frac{2\beta}{c} t\right)\exp(i2\pi f_c \alpha t) \end{aligned} \tag{5.57}$$

where *PRI* is the Pulse Repetition Interval. When the time domain is sampled in a fast-time, slow-time form with $t = t1 + k\text{PRI}$ and $0 < t_1 < PRI$, the received signal becomes

$$
\begin{aligned}
s_R(t_1,k) = \hat{\gamma}_R \sum_{m=0}^{M-1} s\left(t_1 - (m-k)\mathrm{PRI} - \frac{2R_0}{c} - \tau_j\right) \\
\times \exp\left(-i2\pi f_c \frac{2\beta}{c} t_1\right) \exp\left(-i2\pi f_c \frac{2\beta}{c} k\mathrm{PRI}\right) \\
\times \exp\left(i2\pi f_c \alpha t_1\right) \exp\left(i2\pi f_c \alpha k\mathrm{PRI}\right)
\end{aligned}
\tag{5.58}
$$

For a fixed range bin, the phase terms containing t_1 will be constant across each pulse. This therefore means they can be placed into the term $\hat{\gamma}_R$, which contains the other constant phase terms. When $k-m=0$ and when the pulse width, τ, is less than the PRI ($\tau <$ PRI), the received pulse train at the seeker is

$$
\begin{aligned}
s_R(t_1,k) = \hat{\gamma}_R s\left(t_1 - \frac{2R_0}{c} - \tau_j\right) \\
\exp\left(-i2\pi f_c \frac{2\beta}{c} k\mathrm{PRI}\right) \exp\left(i2\pi f_c \alpha k\mathrm{PRI}\right)
\end{aligned}
\tag{5.59}
$$

Table 5.4 gives the seeker position variables and the additional false target positions for an example scenario.

Table 5.4: Example Scenario Variables

Variable	Seeker	False Target	Miss Distance
Down-range (km)	14	14.2	0.2
Cross-range (km)	0.5	0.8	0.3

The constant $\frac{2(\delta_R)}{c}$ can be considered to be the additive range component and the term $\frac{Vt(x_0+\delta_x)}{(R_0+\delta_R)} - \frac{Vtx_0}{R_0}$ is the phase component, which will give the Doppler history. This therefore determines the cross-range position of the false target. This approximation holds providing that there is no range migration during a CPI.

Using Eq. (5.59), positions in Table 5.4 and the signal variables in Table 5.5, a simulation was used to demonstrate that a false target at a different cross-range position to the jammer can be induced into the seeker DBS image. This is achieved by incrementally applying a

phase shift to the received seeker waveform.

Table 5.5: Simulation Waveform Variables

Variable	Symbol	Value
Carrier Frequency	f_c	36 GHz
Bandwidth	B	40 MHz
Pulse Width	τ	3 μs
Pulse Repetition Frequency	PRF	10 kHz

Figure 5.16 shows a chirp pulse of 3 μs duration and 5.17 shows the bandwidth of the chirp to be 40 MHz.

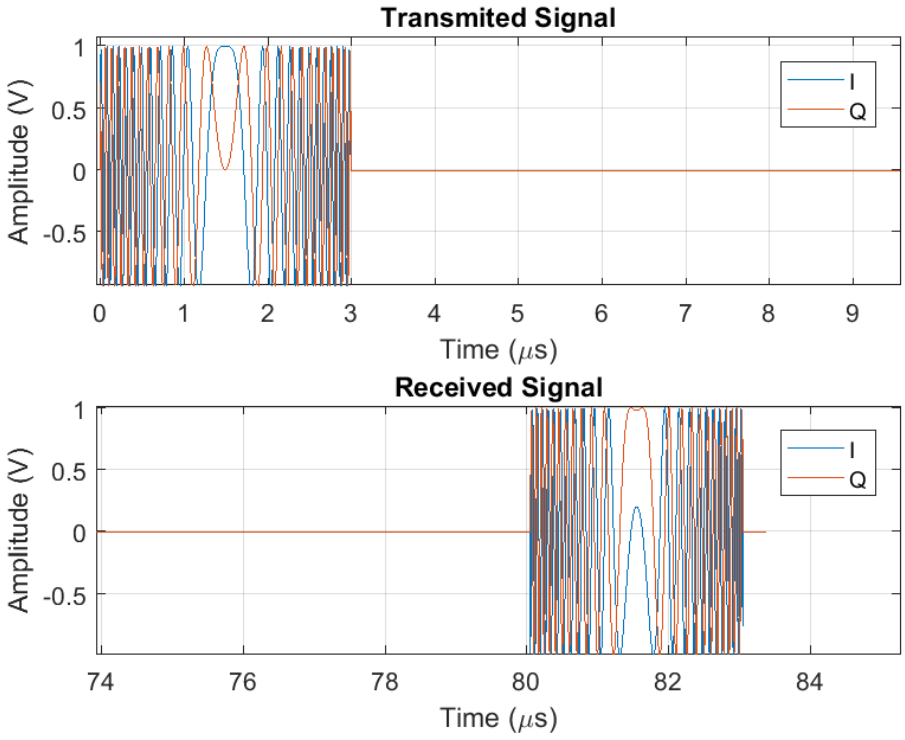

Figure 5.16: Transmitted and Received Waveforms

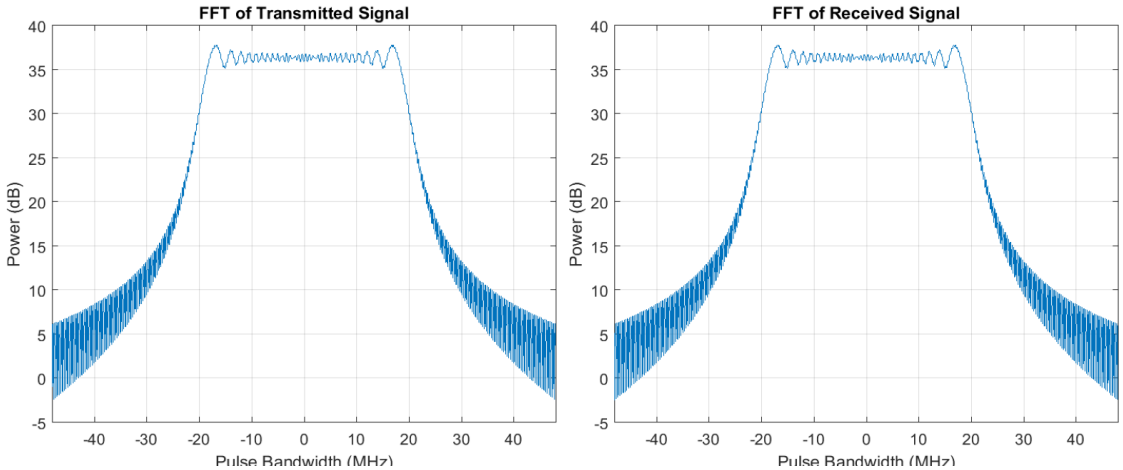

Figure 5.17: Frequency Spectrum of Transmitted and Received Waveforms

Figure 5.18 shows a clean range and Doppler profile of the false target to be at 14.2 km in range and 0.8 km in cross-range, as intended. The range and cross-range resolutions are the same as the previous scenarios (3.75 m and 33.64 m respectively).

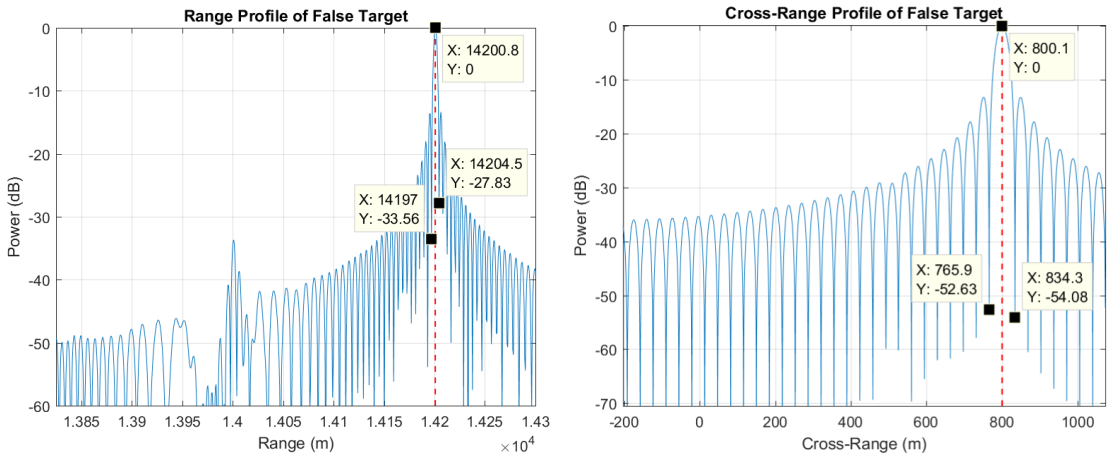

Figure 5.18: Range and Doppler Slices of False Target

The range-Doppler map and DBS image for the scenario is shown in Figure 5.19 and two targets (jammer and false target) can be clearly seen at the correct locations. Likewise with the previous section with the varying time delay method, the expected Doppler shift for the false target is 3665.37 Hz which is shown in the range-Doppler map in Figure 5.19. The DBS image shows the echo and false targets at the correct position of 14.2 km in range, 0.8 km in cross-range.

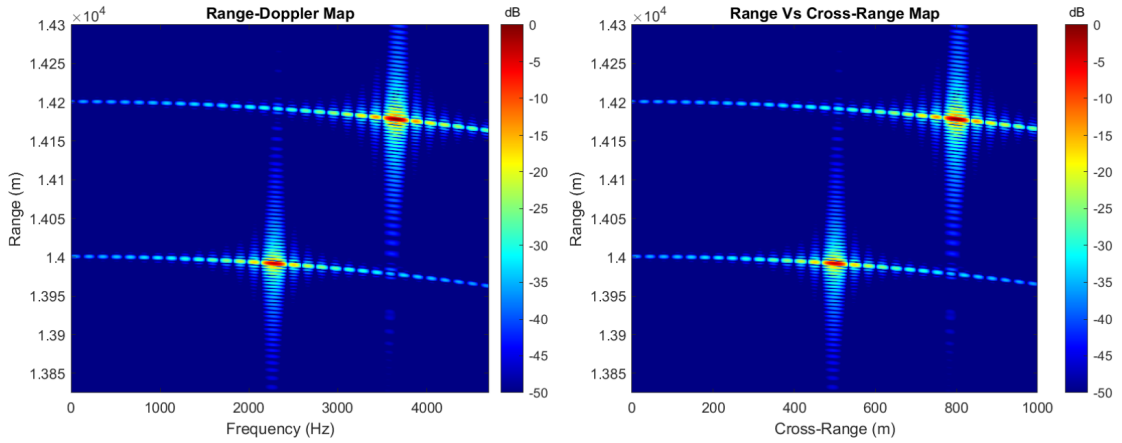

Figure 5.19: Range-Doppler Map and DBS Image of Scenario

5.3.3 Constant Delay Only

Eq. (5.59) from the previous section shows that if the jammer uses the previous scheme (depicted in Figure 5.15, but without a modification), a false target can be created at the same cross-range/Doppler position but at an increased range . If α is set to zero, but τ_j is set to the desired additive range, the result at the seeker is

$$s_R(t_1,k) = \hat{\gamma}_R s\left(t_1 - \frac{2R_0}{c} - \tau_j\right) \exp\left(-i2\pi f_c \frac{2\beta}{c} k\text{PRI}\right) \tag{5.60}$$

which shows the jammer can use the movement of the seeker to at least create the target at the same Doppler and cross-range, but at a different range. Figures 5.20 and 5.21 show the result of this method and that the position of the false target will be at the same position of the jammer, but at an additive range.

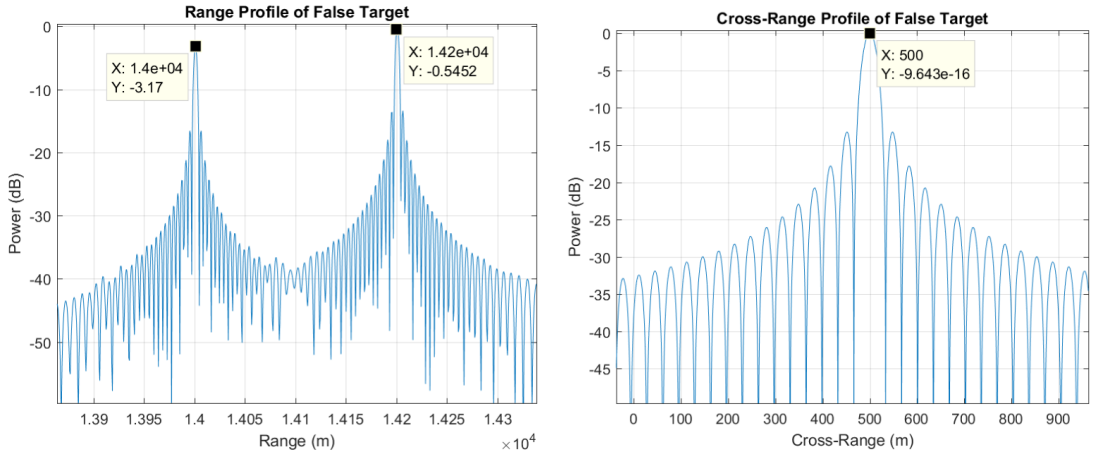

Figure 5.20: Range and Doppler Slices of False Target

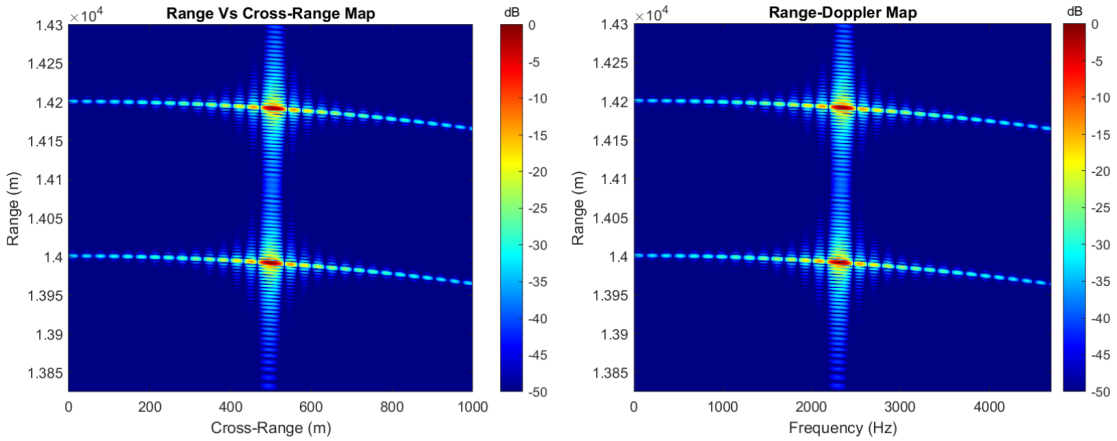

Figure 5.21: Range-Doppler Map and DBS Image of Scenario

This method is primitive, but could be used if the jammer only has the ability to repeat seeker waveforms. The jammer could continuously repeat the seeker waveform, to essentially fill each range bin corresponding to the Doppler position of the jammer. It would then change into a form of denial jamming. by denying the seeker the ability to determine the range position of the jammer.

5.3.4 Evaluation of Methods

Two implementation methods of creating false targets against DBS seekers have been presented. Theoretically, both are equivalent in terms of generating a false target at the correct location. The problem with both methods is that the jammer requires perfect knowledge of the seeker location, in order to place a false target at the desired location in the seeker image. The issue with the 'Varying Time Delay' method, is that the incremental delay between pulses for a general scenario is in the order of picoseconds, as shown in Figure 5.9. In practice, such precise timings are difficult to achieve. A more viable solution is to use the second scheme; a constant delay, and incremental Doppler shift to the seeker waveform. It is for this reason that the experimental sections of this chapter focus on the second implementation method.

5.4 Testing Jamming Scheme Without Antenna Motion

Using the techniques in the previous sections with a Universal Software Radio Peripheral (USRP), a false target was induced into an image at a desired cross-range position of 3m. With the experiment using the USRP, there was no real movement of the antennas, only a constant delay caused by the separation of the two antennas. The aim of this experiment was to show that a waveform could be modified to induce a target at a desired location. It was the first stage of the experiments in this chapter, to give an initial demonstration of the derived theory.

A target at 3 m cross-range was induced by applying an incremental shift to each transmitted pulse by using an assumed missile velocity. This experiment was carried out using a Linear Frequency Modulated (LFM) waveform, as per the simulated scenario in Figure 5.19. The variables used in the measurement are shown in Table 5.6 and the USRP used was a National Instruments NI 2943R. The USRP was controlled using LabVIEW and embedded Matlab software designed the waveforms used. No additional miss distance in downrange was added in this experiment, so the quantity δ_R is zero. As there was no real movement of the antennas, the quantity β was also zero. Therefore, the transmitted waveform was modified to

$$\begin{aligned} s_T(t_1,k) = &\sum_{m=0}^{M-1} s\left(t_1-(m-k)PRI\right) \\ &\exp\left(i2\pi f_c(t_1+kPRI)\right)\exp\left(i2\pi f_c\alpha(t_1+k\text{PRI})\right) \end{aligned} \tag{5.61}$$

where for this measurement,

$$\alpha = \frac{2\beta_J}{c} = \frac{2V\delta_x}{cR_0} \tag{5.62}$$

$$s(t) = e^{i\pi\gamma t^2} Rect\left(\frac{t}{\tau}\right) \tag{5.63}$$

where

$$Rect\left(\frac{t}{\tau}\right) = \begin{cases} 1, & -\frac{\tau}{2} < t < \frac{\tau}{2} \\ 0, & \text{Elsewhere} \end{cases} \tag{5.64}$$

Following the same notation as the previous section and when $k-m=0$, the received waveform after down-conversion was

$$s_R(t_1,k) = \hat{\gamma}_R \sum_{m=0}^{M-1} s\left(t_1 - \frac{R_0}{c}\right) \exp\left(i2\pi f_c \alpha k \text{PRI}\right) \tag{5.65}$$

As there was only one way propagation and no movement of the antenna, the term β was not included in the equations.

Table 5.6: USRP Variables

Variable	Symbol	Value
Carrier Frequency	f_c	4 GHz
Bandwidth	B	40 MHz
Pulse Width	τ	10 μs
Sampling Rate	F_s	80 MHz
Assumed Missile Velocity	V	100 m/s
Pulse Repetition Interval	PRI	50 μs
Number of Pulses	M	128

Figure 5.22 shows the set-up in the laboratory with two vivaldi antennas mounted on tripods, connected to the USRP with standard RF cables.

Figure 5.23 shows the range and cross-range profiles of the false target and demonstrate the additive cross-range position of 3 m in cross-range.

Figure 5.22: USRP Set-Up

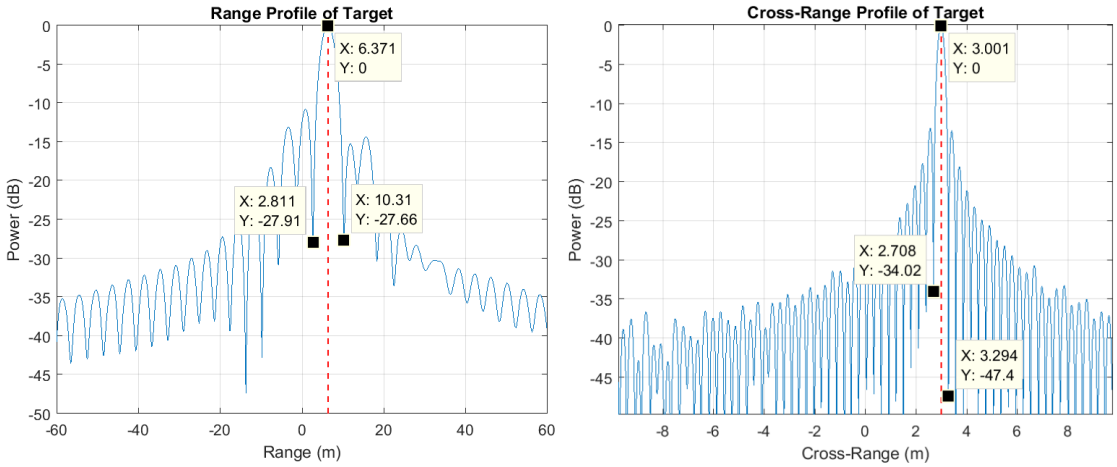

Figure 5.23: Range and Doppler Profile of False Target

Figure 5.24 shows the DBS image of this scenario with a clean target at 6m in range and 3m in cross-range. These figures demonstrate that a false target can be generated at the desired location within a DBS image, providing that the seeker trajectory is known and the carrier frequency and waveform have been estimated correctly.

These measurements were performed for a completely known/assumed trajectory and the next step is to change the experimental set-up to incorporate real movement of the antennas, in accordance with the movement of the missile during one CPI.

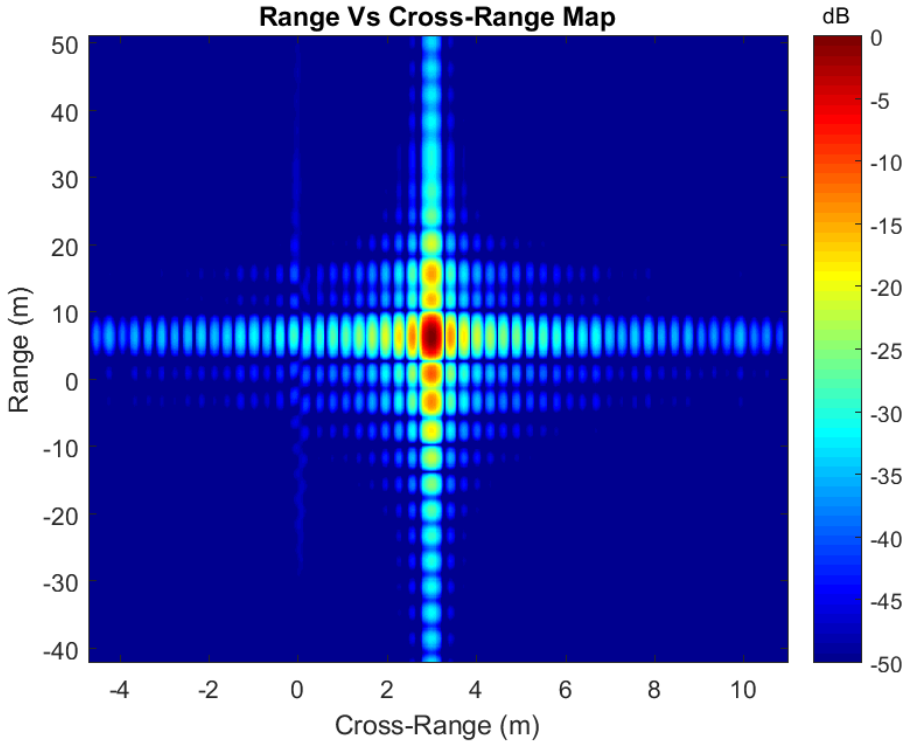

Figure 5.24: Induced False Target

5.5 Testing Jamming Scheme with DBS Rail

In order to test the theory developed in this chapter and demonstrate the practical implementation of it, real measurements were taken in a laboratory. The aim of the measurements was twofold; to show that the developed theory is correct and false targets appear in the correct location, as well as to show that the positions of the false target change accordingly, when various parameters of the seeker trajectory are erroneously estimated. The errors caused by incorrect seeker trajectory estimation will be discussed in the next chapter. The aims of the experiment were met using physical antenna movement, by sliding an antenna across an aperture with respect to a stationary target. The movement was carried out in steps and was used to simulate the linear motion of a missile to test the developed theory.

A thorough explanation of the rail is provided in Chapter 4. However, a brief summary of the rail will now be provided for convenience. The rail used is 2 m long and is driven by a

'NEMA 17' stepper motor, as shown in Figure 5.25. The motor used had 0.9° resolution with 400 steps per 360° revolution. The breakout board used to interface the Arduino to the stepper motor, was an A4988 'StepStick' driver board.

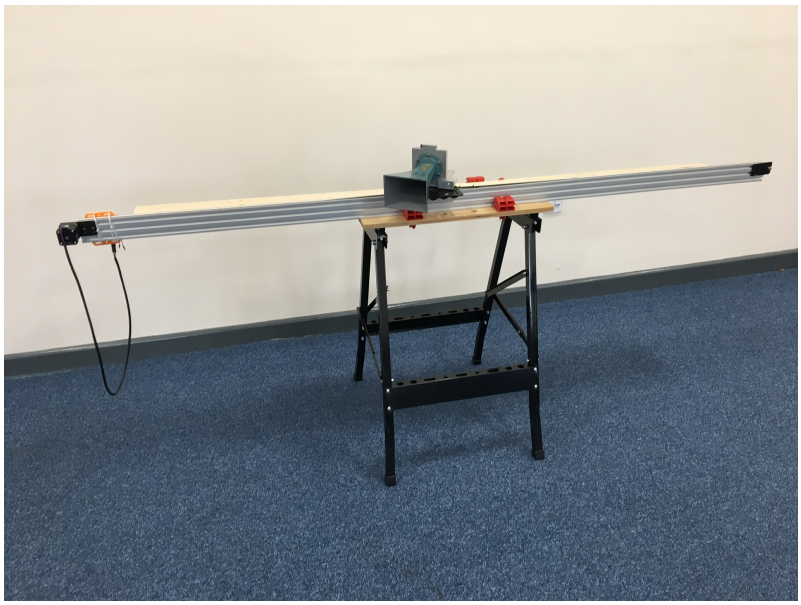

Figure 5.25: Experimental DBS Rail

For the measurements, two pyramidal horn antennas were used, as shown in Figure 5.26.

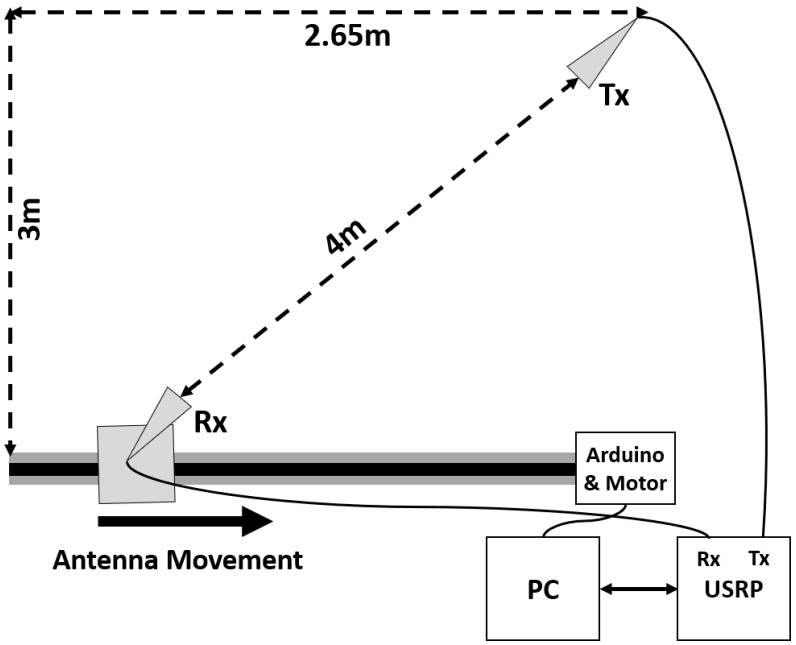

Figure 5.26: Experimental Layout

The measurements were completed in the far-field region of the antennas. No beam steering was used (mechanically or electronically) during the measurement, but the receiving antenna was kept inside the main beam of the transmitter for all of the transmitted pulses. The horizontal beamwidth used is calculated by [Balanis, 2015]:

$$\theta_h = \frac{51\lambda}{W} = \frac{51 \times 0.06}{0.09} = 34^\circ \tag{5.66}$$

where W is the width of the antenna at the flared end. This means at a range of 4 m, the cross-range resolution of the real beam is $2Rsin\left(\frac{\theta_h}{2}\right)$ and therefore ≈ 2.34 m.
The waveforms were generated with a Universal Software Radio Peripheral (USRP), made by National Instruments (NI-2943R). LabVIEW was used to control both the USRP and the Arduino and Matlab was embedded into the LabView program to design the waveforms. Table 5.7 shows the signal variables for the measurements and Figure 5.26 shows the geometry of the measurement.

Table 5.7: USRP Variables

Variable	Symbol	Value
Carrier Frequency	f_c	5 GHz
Bandwidth	B	30 MHz
Pulse Width	τ	10 μs
Sampling Rate	F_s	80 MHz
Assumed Missile Velocity	V	60 m/s
Pulse Repetition Interval	PRI	$50\mu s$
Number of Pulses	M	128

False Target in Cross-Range Only

By using a slightly modified version of Eq. (5.59), a false target can be induced at a desired location by modifying the transmitted waveform to incorporate an incremental shift. The modification was necessary due to one-way (instead of two-way) propagation, as shown in Figure 5.26. In order to create an 'echo' for reference, two pulses were transmitted. The first pulse was unmodified (where α and τ_j are set to zero) for the 'echo'. The second pulse was modified using the corresponding values for τ_j and α to create the false target. The variables of the trajectory (V, R_0 and x_0) and the carrier frequency, were assumed to be known to the jammer. Following the same scheme used for a pulsed DBS system from the previous section and by using Eq. (5.59), the transmitted signal was

$$\begin{aligned} s_T(t_1,k) = \sum_{m=0}^{M-1} & s\left(t_1-(m-k)PRI\right)\exp\left(i2\pi f_c(t_1+kPRI)\right) \\ & \exp\left(i2\pi f_c\alpha(t_1+k\text{PRI})\right) \end{aligned} \tag{5.67}$$

and when $k-m=0$ the received waveform after down-conversion was

$$\begin{aligned} s_R(t_1,k) = & \gamma\sum_{m=0}^{M-1} s\left(t_1-\frac{R_0}{c}\right) \\ & \times\exp\left(-i2\pi f_c\frac{R_0}{c}\right)\exp\left(-i2\pi f_c\frac{\beta}{c}t_1\right)\exp\left(-i2\pi f_c\frac{\beta}{c}k\text{PRI}\right) \\ & \times\exp\left(-i2\pi f_c\alpha\frac{R_0}{c}\right)\times\exp\left(i2\pi f_c\alpha t_1\right)\exp\left(i2\pi f_c\alpha k\text{PRI}\right) \end{aligned} \tag{5.68}$$

For a fixed range bin, the phase terms containing t_1 will be constant from pulse to pulse. This therefore means they can be placed into the term $\hat{\gamma}_R$, which contains the other constant phase terms. This gives the final received signal as

$$\begin{aligned} s_R(t_1,k) = \hat{\gamma}_R \gamma \sum_{m=0}^{M-1} s\left(t_1 - \frac{R_0}{c}\right) \\ \times \exp\left(-i2\pi f_c \frac{\beta}{c} k\text{PRI}\right) \exp\left(i2\pi f_c \alpha k\text{PRI}\right) \end{aligned} \tag{5.69}$$

Eq.(5.69) shows that for a pulsed waveform, introducing a false target in a fixed range bin is equivalent to introducing an incremental phase shift from pulse to pulse. This will be exploited for the experimental demonstration of the results where a 'stop and go' method is employed to carry out measurements without the use of a DFRM. The 'stop and go' method has been used solely for the scope of demonstrating the jamming technique in the laboratory. As shown in Eq. (5.51), a higher velocity or varying PRF does not affect the analytical performance of the proposed solution as long as the narrowband approximation in Eq. (5.50) holds (which is commonly the case for the velocities of the missiles under consideration in this research). From Eq. (5.69) and for a fixed range bin, the Doppler shift can be induced with respect to slow-time (kPRI) and not fast time. As shown in Figure 5.25, the range bin will be fixed for the experiment, enabling the 'stop and go' method to be used.

For this measurement,

$$\alpha = \frac{\beta}{c} - \frac{2\beta_J}{c} \tag{5.70}$$

and

$$s(t) = e^{i\pi\gamma t^2} Rect\left(\frac{t}{\tau}\right) \tag{5.71}$$

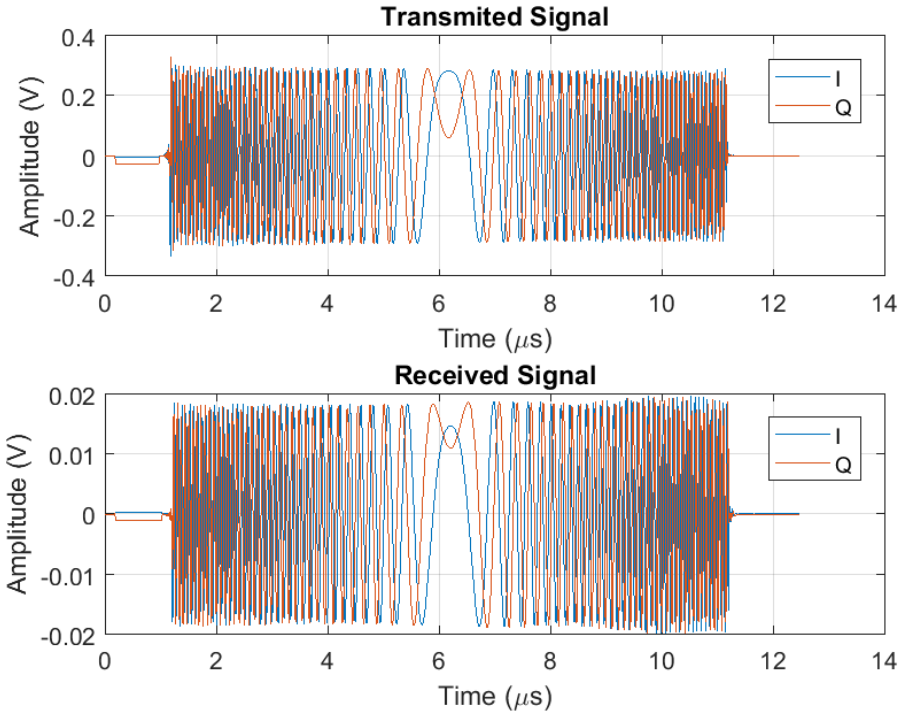

Figure 5.27: Transmitted and Received Waveforms

where

$$Rect\left(\frac{t}{\tau}\right) = \begin{cases} 1, & -\frac{\tau}{2} < t < \frac{\tau}{2} \\ 0, & \text{Elsewhere} \end{cases} \tag{5.72}$$

A transmitted and received waveform is shown in Figure 5.27 with a pulse width of 10μs.

The the corresponding frequency spectrums with a bandwidth of 30 MHz are shown in Figure 5.28. The figures show that the transmitted and received bandwidths are the same. The range profiles of the scenario are shown in Figure 5.29.

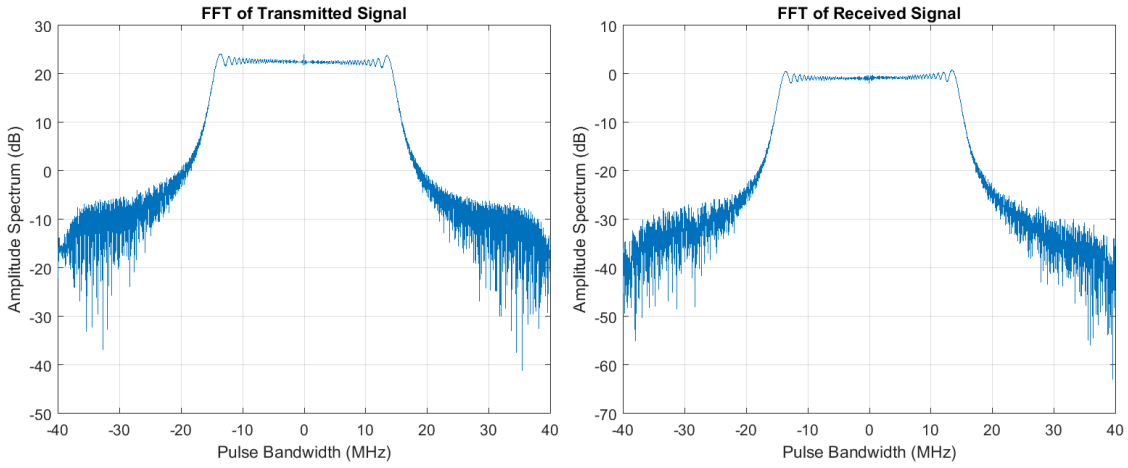

Figure 5.28: Frequency Spectrum of Transmitted and Received Waveforms

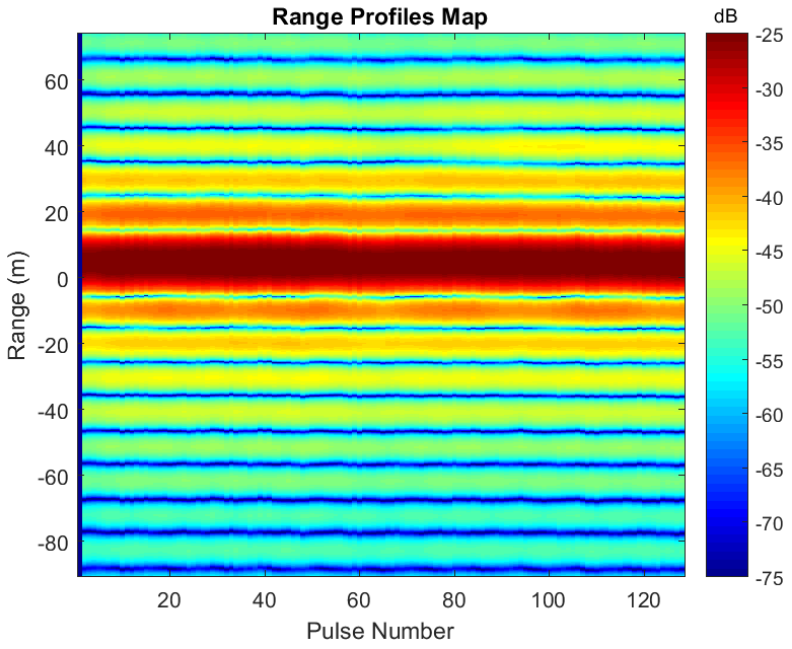

Figure 5.29: Range Profiles of 'Echo' and False Target

Figure 5.30 shows that a false target can be induced to have a cross-range position of 10m. The reference of the antenna location is at 2.65 m. The result gives clean range and Doppler profiles at the correct positions. With a bandwidth of 30 MHz, the null-to-null width of the main lobe of the range profile should be 10m to give a 3 dB range-resolution of 5 m, which the plot labels show. Using the values in Table 5.7, the Doppler resolution is 156.25 Hz. With the geometry in Figure 5.26 and values in Table 5.1, the cross-range resolution is

$$\Delta_{CR} = \frac{\delta_{fd}\lambda R_0}{2V\sin(\theta_\lambda)} = \frac{156.25 \times 0.06 \times 4}{2 \times 60 \times \sin(48.54)} = 0.42 \text{ m} \tag{5.73}$$

which is shown in the Figure.

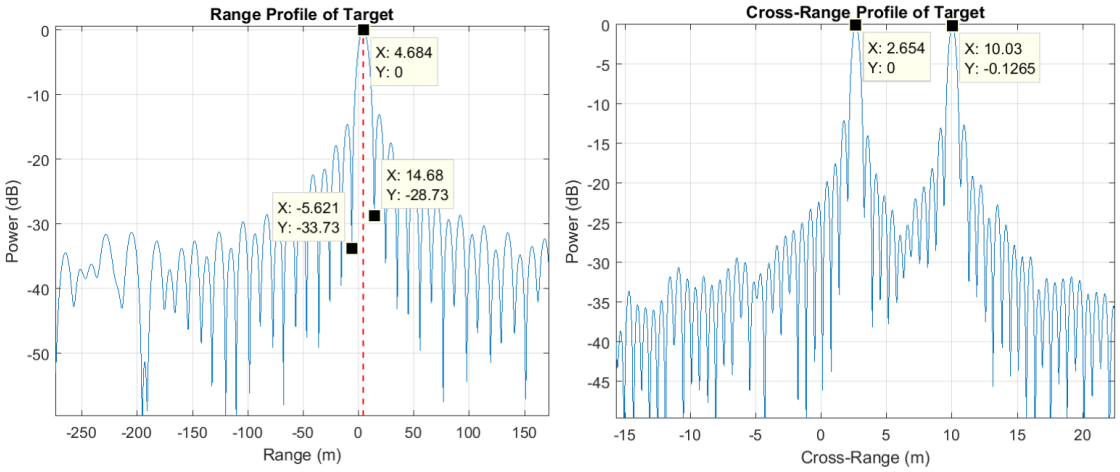

Figure 5.30: Range and Doppler Slices of 'Echo' and Jamming Target

The final result is given in Figure 5.31 which shows a range-Doppler map and a DBS image of the reference target and false target. The expected one-way Doppler value for the false target in the range-Doppler map is 2500 Hz which was remapped to give a cross-range position of 10 m in the DBS image.

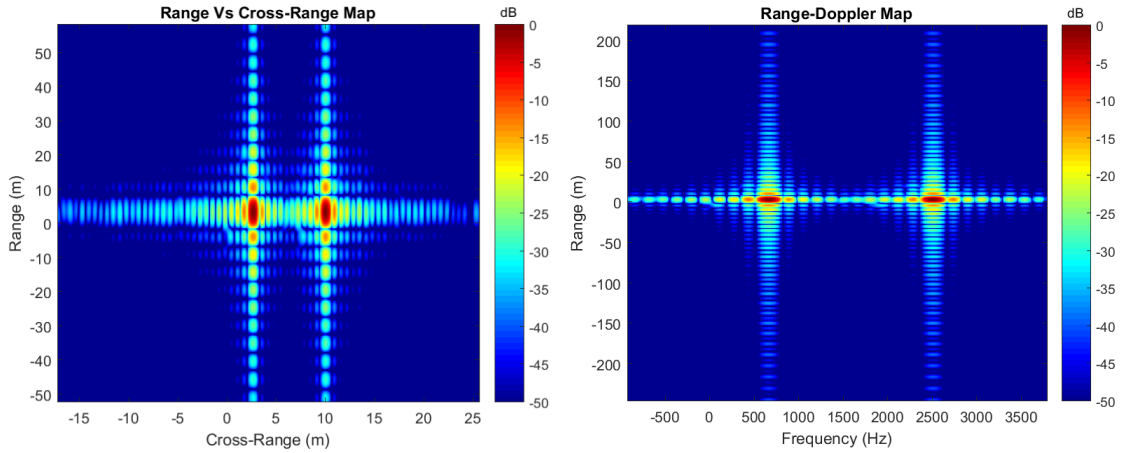

Figure 5.31: Range-Doppler Map and DBS Image of 'Echo' and Jamming Target

False Target with Additive Range and Cross-Range

Following the method in the previous sub section, the next step was to create a false target with an additive range and cross-range. Using the derived jamming scheme, a false target was created at 35 m in range and 60 m in cross-range. A transmitted and received waveform for a single target is shown in Figure 5.32 and the corresponding frequency spectrums in Figure 5.33. The figures show a transmitted pulse width of 10 μs and bandwidth of 30 MHz.

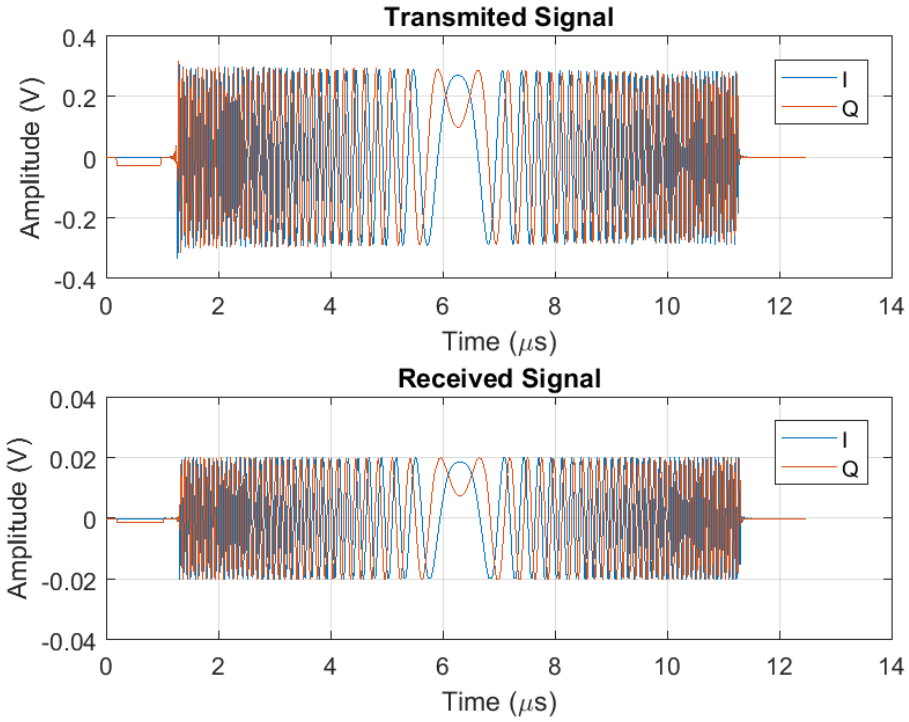

Figure 5.32: Transmitted and Received Waveforms

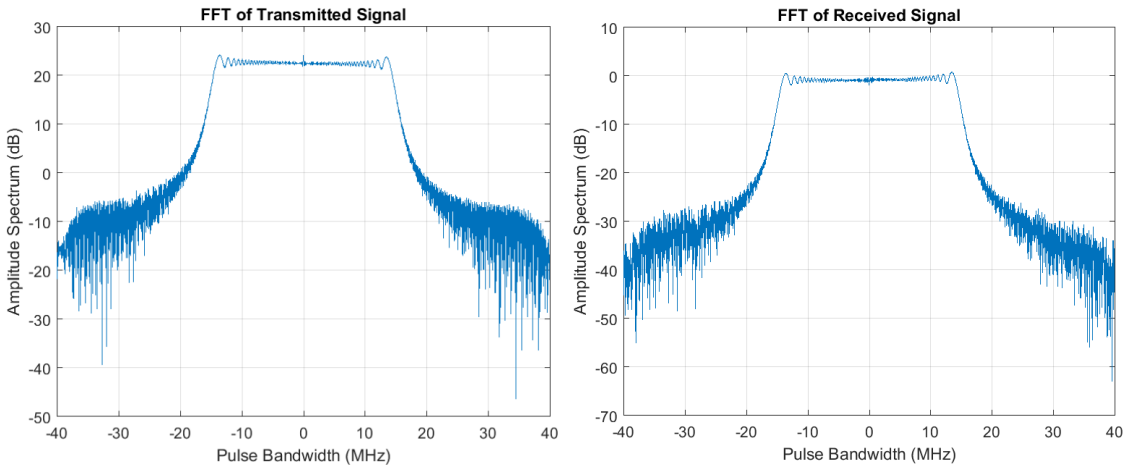

Figure 5.33: Frequency Spectrum of Transmitted and Received Waveforms

Figure 5.34 shows the range profiles of the scenario and shows two profiles, one for the reference echo and one for the false target.

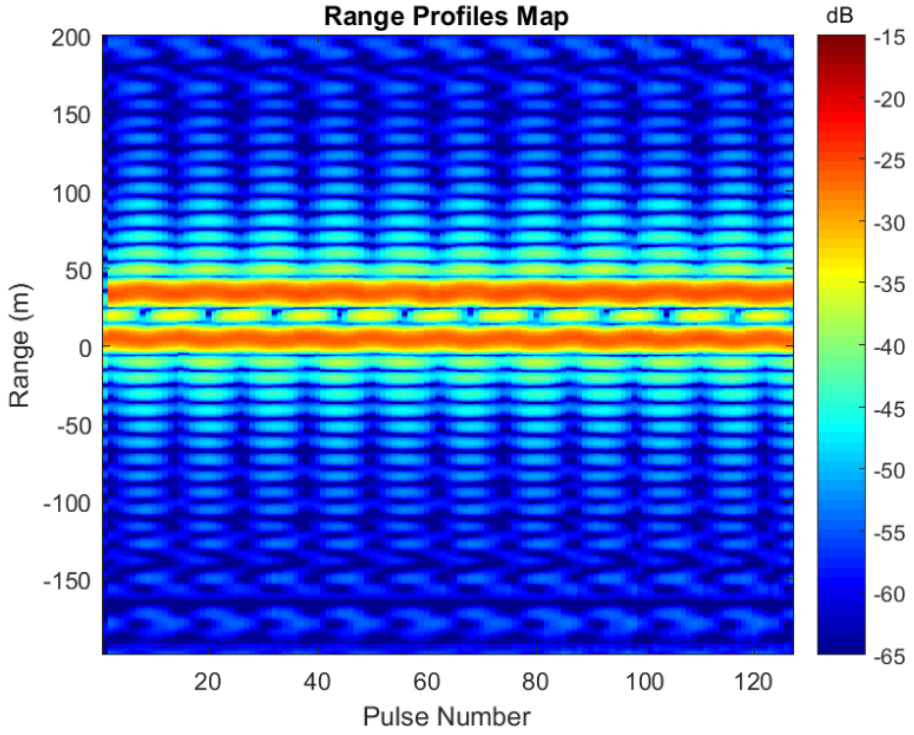

Figure 5.34: Range Profiles of 'Echo' and False Target

Figure 5.35 shows the range and cross-range (Doppler) profiles of the false target. The figures show the false target to have the correct range and cross-range positions of 35 m and 60 m, respectively.

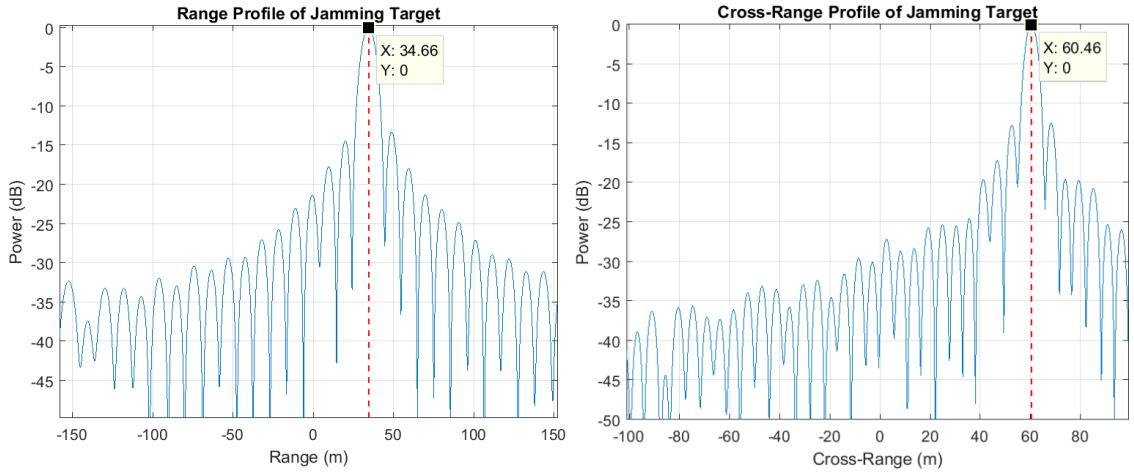

Figure 5.35: Range and Doppler Slices of 'Echo' and Jamming Target

The final result of the scenario is given in Figure 5.36 which shows a range-Doppler map and DBS image. The expected Doppler value for the false target in the range-Doppler

map is 2285.7 Hz which was remapped to give a cross-range position of 60 m in the DBS image. The 'echo' reference target was also remapped to be at the correct cross-range value of 2.65 m. These figures show clean false targets at the expected locations.

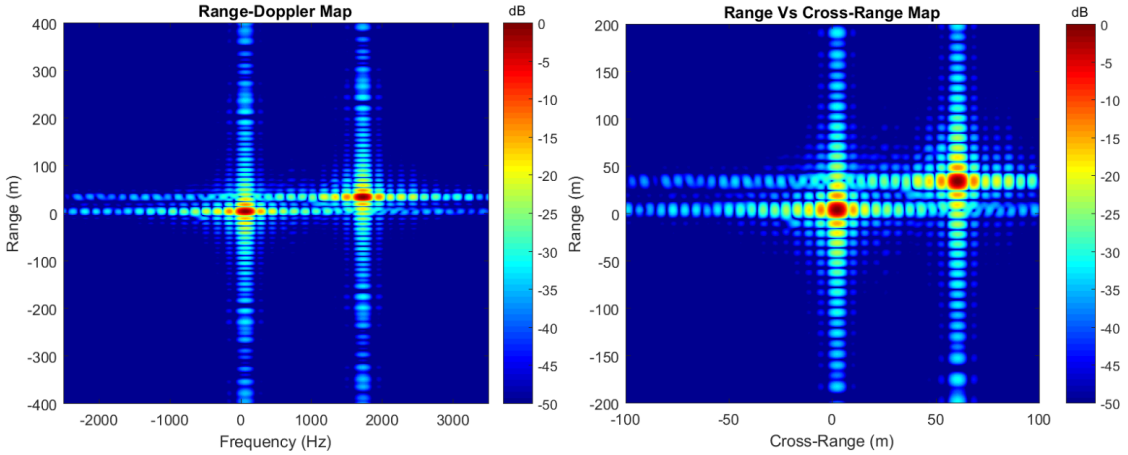

Figure 5.36: Range-Doppler Map and DBS Image of 'Echo' and Jamming Target

5.6 Conclusion

This chapter has presented two implementation methods to create false targets in the DBS image of a missile seeker. The first method was to repeat the waveforms of the seeker with an incremental delay. This was tested with simulations and shown to be effective in principle. The problem with this method, is that it requires incredibly precise timings (in the order of picoseconds) and is therefore difficult to realise in practice.

Building upon the first method, the second method repeats the waveforms of the seeker with a constant time delay and time varying additive Doppler shift, to create the false target. This technique will be easier to realise in practice against narrowband radars. The experimental results show that the second technique can place false targets at precise locations, if the trajectory of the missile is known.

The derived theory shows that the Doppler shift the jammer applies to the waveform of the seeker is dependant on three properties, velocity, cross-range and down-range. All of these parameters can be incorrectly estimated and will affect the position of the false targets in varying amounts. Chapter 6 will investigate the effect of using these parameters with incorrect values on the position of the false target and which parameters give the largest sources of error.

Chapter 6

Assessment of Errors in False Targets

6.1 Introduction

In this thesis, all of the methods of introducing false targets into DBS images rely on knowledge of the trajectory of the seeker, as well as the ability to create high fidelity copies of the received waveform. This is to be able to modify and transmit a perfect jamming waveform to create a perfect false target, in terms of location. This chapter explores the effects and implications to the position of the false targets when errors are systematically introduced and controlled.

The derived theory and experimental results will show that the largest cause of error in the position of the false target is the velocity estimation, followed by downrange and cross-range estimations when $R_0 >> x_0$. The theory also shows that the initial phase of the jamming frequency shift, does not affect the location of the false target.

6.2 Measurement Error Theory

In order for the jammer to correctly modify the waveforms, data from a tracking radar will need to be given to the jamming system. This would likely be from the on-board surveillance and tracking radars that military ships will use. To better understand the size and scale of the errors, parameters for a generic tracking radar have been used to calculate the expected magnitude of measurement errors (for a single pulse) that a radar could theoretically have. These parameters are shown in Table 6.1. A tracker could potentially improve on these errors, so the equations are used to gain an understanding of the magnitude of the respective errors, in a general case. These errors occur when taking various measurements about a target in the presence of Gaussian white noise. General equations for measurement errors for azimuth, range and Doppler, respectively, are listed as follows [Skolnik, 2001]:

$$\delta_x = \frac{Rsin(\theta_{3dB})}{\sqrt{2SNR}} \tag{6.1}$$

$$\delta_R = \frac{c}{2B\sqrt{2SNR}} \tag{6.2}$$

$$\delta_{fd} = \frac{\lambda}{\Delta t\sqrt{2SNR}} \tag{6.3}$$

where R is the target range, θ_{3dB} is the 3 dB beamwidth of the radar antenna, Δ_t is the dwell time on the target and SNR is the signal to noise ratio. With instantaneous bandwidths in the order of 100s of MHz, the range errors induced by poor a SNR are small (less than the resolution cell). With a bandwidth of 100 MHz, the range resolution is 1.5m. The expected errors in the measured Doppler shift with an SNR of 3 dB are in the order of 1% when the missile is travelling directly towards the tracking radar at 270 m/s. A low value for SNR was deliberately used to generate larger theoretical errors. Whilst the range and velocity measurement errors are small, relative to the range resolution of the

radar and velocity of the missile, these measurement errors can be significantly increased in the presence of jamming of the tracking radar (which provides tracking data to the DBS jammer).

Table 6.1: Generic Tracking Radar Parameters

Variable	Symbol	Value
Carrier Frequency	f_c	3 GHz
Bandwidth	B	100 MHz
Pulse Width	τ	10 μs
Pulse Repetition Frequency	PRF	20 kHz
3 dB Horizontal Beamwidth	θ	2°
Dwell Time	Δt	1 ms
Assumed Low SNR	SNR	3 dB
Range	R	20 km

6.2.1 Erroneous Trajectory Estimation

For the jammer to accurately place a false target at the desired location, it requires knowledge of the seeker position and velocity. The previous chapter described the jamming theory to create a perfect false target in the seeker DBS image. Eq (5.50) and Eq (5.51) showed the jamming waveform the seeker would receive and what a perfect jamming response would be, respectively. For convenience, they have been re-listed here. The seeker would receive

$$s_R(t) = \hat{\gamma}_R\, s\left(t - \frac{2R_0}{c} - \tau_j\right) \exp\left(-i2\pi f_c \frac{2\beta}{c} t\right) \exp\left(i2\pi f_c \alpha t\right) \tag{6.4}$$

and an ideal target located at $(x_0 + \delta_x, R_0 + \delta_R)$ would generate an echo signal of

$$s_R(t) = \gamma_R\, s\left(t - \frac{2(R_0 + \delta_R)}{c}\right) \exp\left(-i4\pi \frac{(R_0 + \delta_R)}{\lambda}\right) \exp\left(i2\pi \frac{2V(x_0 + \delta_x)t}{\lambda(R_0 + \delta_R)}\right) \tag{6.5}$$

Chapter 5 also derived the value of α in the jamming modification. The result of this derivation is re-listed here as

$$\alpha = \frac{2\beta}{c} - \frac{2\beta_J}{c} = \frac{2V(x_0 + \delta_x)}{c(R_0 + \delta_R)} - \frac{2Vx_0}{cR_0} \tag{6.6}$$

The variables V, x_0 and R_0 in Eq. (6.6) can be incorrectly estimated by varying amounts. Incorporating these errors into Eq. (6.6) results in the incorrect Doppler parameter of

$$\alpha_\varepsilon = \frac{2}{c}\left[\frac{V_\varepsilon V(x_\varepsilon x_0 + \delta_x)}{(R_\varepsilon R_0 + \delta_R)} - \frac{V_\varepsilon V x_\varepsilon x_0}{R_\varepsilon R_0}\right] \tag{6.7}$$

where the scalar variables x_ε, R_ε and V_ε are the numerical ratio between the estimated

value of the variable and the true value for cross-range, downrange and velocity respectively. For example, if the true velocity of the missile is 300 m/s but the jammer estimates it to be 360m/s, then $V_\varepsilon = \frac{V_j}{V} = 1.2$. Incorporating this into the waveform in Eq. (6.4), the resultant waveform would be

$$\begin{aligned} s_R(t) = \hat{\gamma}_R s\left(t - \frac{2R_0}{c} - \tau_j\right) \exp\left(-i2\pi f_c \frac{2\beta t}{c}\right) \\ \times \exp\left(i2\pi f_c t \frac{2}{c}\left[\frac{V_\varepsilon V(x_\varepsilon x_0 + \delta_x)}{(R_\varepsilon R_0 + \delta_R)} - \frac{V_\varepsilon V x_\varepsilon x_0}{R_\varepsilon R_0}\right]\right) \end{aligned} \tag{6.8}$$

with instantaneous frequency

$$f_d = \frac{2}{\lambda}\left(\frac{V_\varepsilon V(x_\varepsilon x_0 + \delta_x)}{(R_\varepsilon R_0 + \delta_R)} - \frac{V_\varepsilon V x_\varepsilon x_0}{R_\varepsilon R_0} + \frac{V x_0}{R_0}\right) \tag{6.9}$$

If there were no errors in the missile trajectory, Eq. 6.8 would simplify to Eq. (6.5). To obtain the cross-range position of the target, the seeker would then invert the Doppler equation to map for the cross-range position at the corresponding range bin of the target. Under the assumption that the jammer has perfectly shifted the false target in down-range, the cross-range position for the false target will be

$$\hat{x} = (R_0 + \delta_R)\left(\frac{V_\varepsilon(x_\varepsilon x_0 + \delta_x)}{(R_\varepsilon R_0 + \delta_R)} - \frac{V_\varepsilon x_\varepsilon x_0}{R_\varepsilon R_0} + \frac{x_0}{R_0}\right) \tag{6.10}$$

Figure 6.1 shows how the cross-range position of the false target will shift when x_ε, R_ε and V_ε from Eq. (6.11) are systematically varied for a seeker, where V = 270 m/s, R_0 = 14 km, x_0 = 0.5 km, δ_R = 200 m and δ_x = 300 m. For example, the plot for the velocity error uses

$$\alpha_\varepsilon = \frac{2}{c}\left[\frac{V_\varepsilon V(x_0 + \delta_x)}{(R_0 + \delta_R)} - \frac{V_\varepsilon V x_0}{R_0}\right] \tag{6.11}$$

The expected trajectories for the missile will generally be such that $R_0 >> x_0$ and as the

cross-range component of the trajectory will be small, relative to the down-range component, errors in cross-range position yield smaller errors than for down-range errors. A simulation of a typical scenario geometry, shown in Figure 6.1, demonstrates this principle and shows that an erroneous velocity estimation will yield the largest errors in the position of the false target.

The purpose of a military system jamming a missile is to avoid being hit by it or damaged by a close detonation. Therefore, it is likely to be more desirable to create a false target at a location further away than intended, than closer, to avoid being hit or damaged. Using this principle, Figure 6.1 shows it is better to underestimate the cross-range and down-range variables and overestimate the velocity magnitude variable. This is a general result, which will hold when $R_0 >> x_0$.

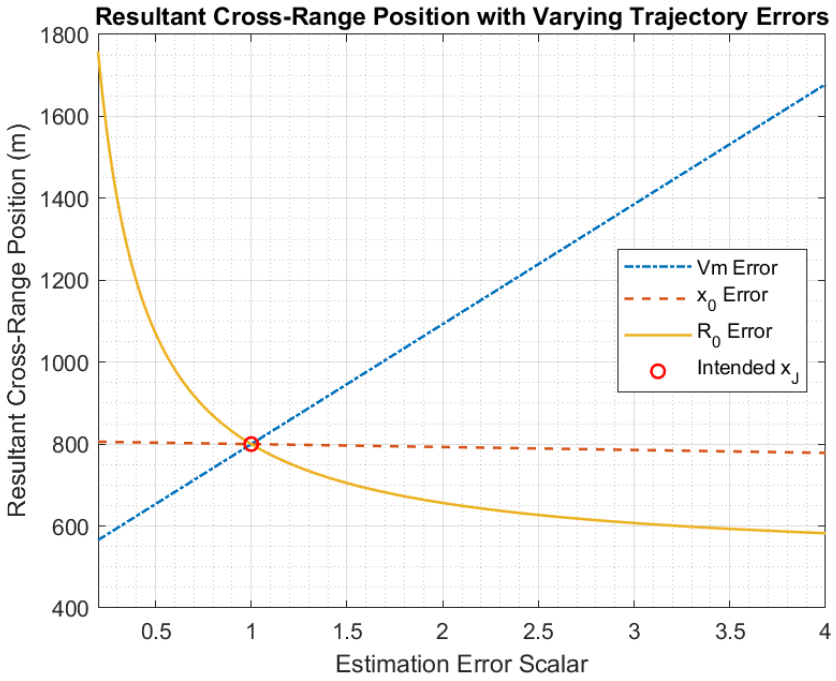

Figure 6.1: Resultant Cross-Range Position with Varying Errors when V = 270 m/s, R_0 = 14 km, x_0 = 0.5 km, δ_R = 200 m and δ_x = 300 m.

Using the same co-ordinates as those in Figure 6.1 (V = 270 m/s, R_0 = 14 km, x_0 = 0.5 km, δ_R = 200 m and δ_x = 300 m) and by using the signal variables detailed in Table 6.2, six simulations were carried out to validate the result obtained in Figure 6.1.

Table 6.2: Simulation Waveform Variables

Variable	Symbol	Value
Carrier Frequency	f_c	36 GHz
Bandwidth	B	40 MHz
Pulse Width	τ	3 μs
Pulse Repetition Frequency	PRF	10 kHz
Number of Pulses	M	64
Dwell Time	t_d	6.4 ms
Doppler Resolution	δ_f	156.25 Hz

Table 6.3 provides the results of the six simulations, with the actual plots of the results shown in Appendix B. The results show that Eq. (6.10) can be used to predict the cross-range error of the false target. All of the results should be at 0.8 km, but are incorrect due to the respective error scalars being applied to the jammer Eq. (6.11).

Table 6.3: Error Variables

Variable	Scalar	Simulated Result (m)
V_ε	0.8	741.5
	2	1093
R_ε	0.8	869.8
	2	656.5
x_ε	0.8	801.4
	2	792.9

6.2.2 Experimental results

Following the simulation in Figure 6.1, the next step was to take measurements in exactly the same way as Chapter 5, to compare the simulated results with experimental results. The experiments in Chapter 5 showed that a false target could be created, if the trajectory of the seeker is known. Figure 6.2 shows the schematic of the experimental setup.

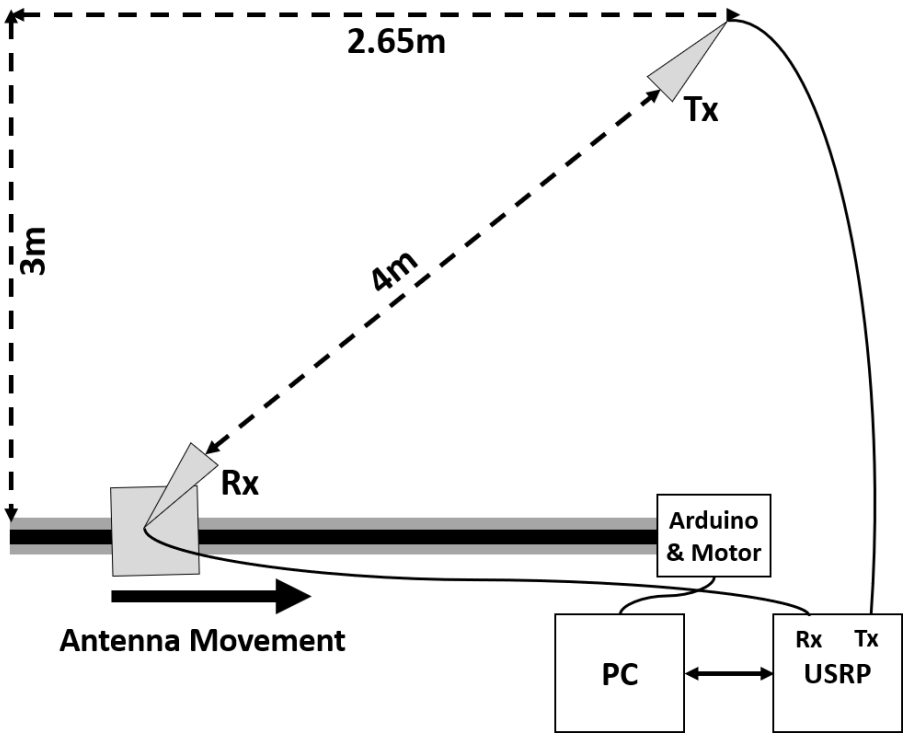

Figure 6.2: Experimental Layout

The method for creating the false target was almost identical to Chapter 5, except that deliberately incorrect values of α was used, with the notation α_ε. Following the same scheme used for a pulsed DBS system from the previous section and by using Eq. (5.59), the transmitted signal was

$$s_T(t_1,k) = \sum_{m=0}^{M-1} x\left(t_1+(m-k)PRI\right)\exp\left(i2\pi f_c(t_1+kPRI)\right)\exp\left(i2\pi f_c\alpha_\varepsilon(t_1+k\mathrm{PRI})\right) \tag{6.12}$$

and the received waveform after down-conversion was

$$s_R(t_1,k) = \gamma \sum_{m=0}^{M-1} x\left(t_1 - \frac{R_0}{c}\right) \exp\left(-i2\pi f_c \frac{R_0}{c}\right) \exp\left(-i2\pi f_c \frac{\beta}{c} t_1\right) \times \exp\left(-i2\pi f_c \frac{\beta}{c} k\text{PRI}\right) \exp\left(i2\pi f_c \alpha_\varepsilon t_1\right) \exp\left(i2\pi f_c \alpha_\varepsilon k\text{PRI}\right) \tag{6.13}$$

Following the same format in Chapter 5, for a fixed range bin, the phase terms containing t_1 will be constant from pulse to pulse. This therefore means they can be placed into the term $\hat{\gamma}_R$, which contains the other constant phase terms. This gives the final received signal as

$$s_R(t_1,k) = \hat{\gamma}_R \sum_{m=0}^{M-1} s\left(t_1 - \frac{R_0}{c}\right) \exp\left(-i2\pi f_c \frac{\beta}{c} k\text{PRI}\right) \exp\left(i2\pi f_c \alpha_\varepsilon k\text{PRI}\right) \tag{6.14}$$

For this measurement,

$$\alpha_\varepsilon = \frac{\beta_\varepsilon}{c} - \frac{2\beta_{J\varepsilon}}{c} \tag{6.15}$$

and

$$x(t) = e^{i\pi\gamma t^2} Rect\left(\frac{t}{\tau}\right) \tag{6.16}$$

where

$$Rect\left(\frac{t}{\tau}\right) = \begin{cases} 1, & -\frac{\tau}{2} < t < \frac{\tau}{2} \\ 0, & \text{Elsewhere} \end{cases} \tag{6.17}$$

α_ε was calculated from Eq. (6.7). By using Eq. (6.10) and the values in Table 6.4, Figure 6.3 shows how the cross-range position for the generated target will change with each error of velocity magnitude, cross-range and down-range. The desired position of the false target in cross-range was 60 m and this is represented by the red circle in the figure. This is the benchmark position and the false target would be at that location if all three error scalars (x_ε, R_ε and V_ε) are equal to 1. Each plot represents a single source

error. For example, the solid orange line varies R_ε between 0.5 and 4, when x_ε and V_ε are equal to 1, for every point on the line.

The method of generating Figures 6.1 and 6.3 is the same, but they are different due to using different geometries to simulate an example real-world scenario and the small-scale laboratory environment.

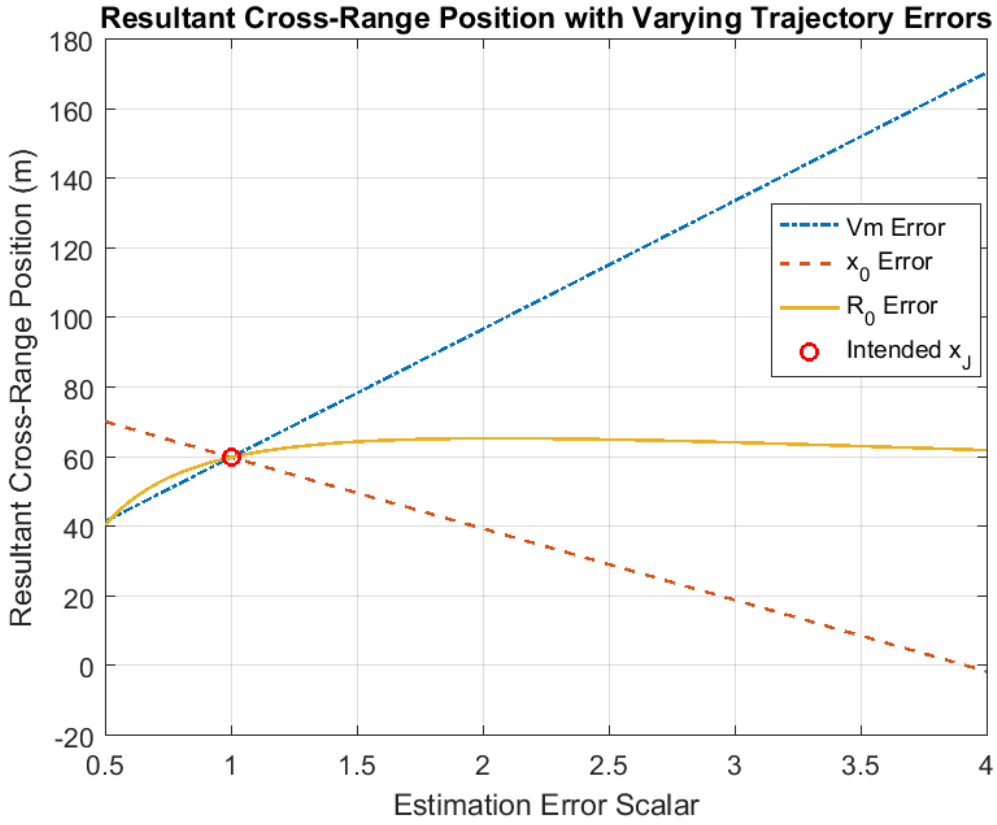

Figure 6.3: Simulated Resultant Cross-Range Position For Each Error Scalar when V = 60 m/s, R_0 =4m, x_0 = 2.65m, δ_R = 31m and δ_x = 57.35m.

To verify Figure 6.3, several more measurements were taken with the USRP, using the values in Table 6.4.

Errors were systematically introduced as shown in Table 6.5. The table details the resultant cross-range position should the jamming equation include errors from one particular error per measurement. For example, the top line of the Table states that the velocity scalar, V_ε has a value of 2. This means that if the jammer uses the same variables as detailed in Table 5.6, every other variable was assumed to be correct, but the jammer

Table 6.4: USRP Variables

Carrier Frequency	f_c	5 GHz
Bandwidth	B	30 MHz
Pulse Width	τ	10 μs
Sampling Rate	F_s	80 MHz
Assumed Missile Velocity	V	60 m/s
Pulse Repetition Interval	PRI	50 μs
Number of Pulses	M	128

modified the waveform to include a velocity of 120 m/s and not 60 m/s.

Table 6.5: Error Variables

Variable	Scalar	Experimental Result (m)	Simulated Result (m)	Difference (m)
V_ε	0.8	53.16	52.63	0.53
	2	97.52	96.85	0.67
R_ε	0.8	55.96	55.62	0.34
	2	66.09	65.42	0.67
x_ε	0.8	65.05	64.1	0.95
	4	-0.8539	-1.515	0.66

Following from Figure 6.1 and by using Eq. (6.10), Figure 6.4 shows how the cross-range position for the generated target will change with each error of velocity magnitude, cross-range and down-range. The experimental data points have been overlaid onto the simulated errors, to show that they match the expected values.

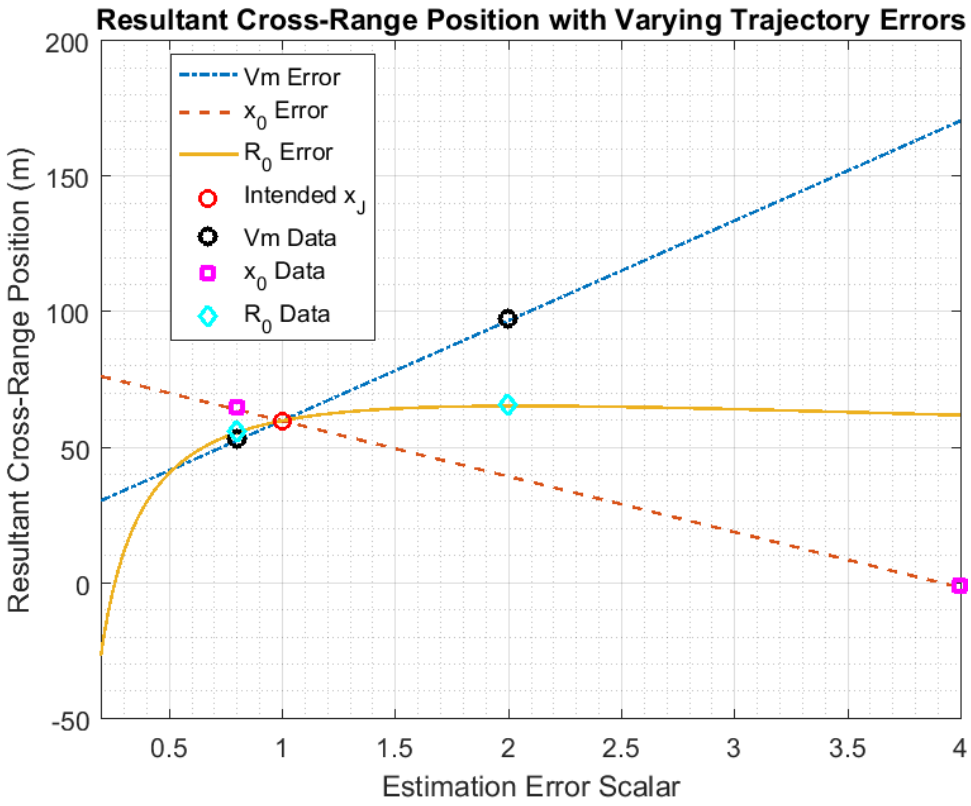

Figure 6.4: Resultant Cross-Range Position For Each Error Scalar

The cross-range (remapped Doppler) profiles for each of the measurements are shown in Figures 6.5, 6.7 and 6.6 respectively. For each of the plots, the intended cross-range position of the target (if there were no errors) was 60 m. Figure 6.5 shows the resultant cross-range position of the false target when x_ε is 0.8 and 4.0.

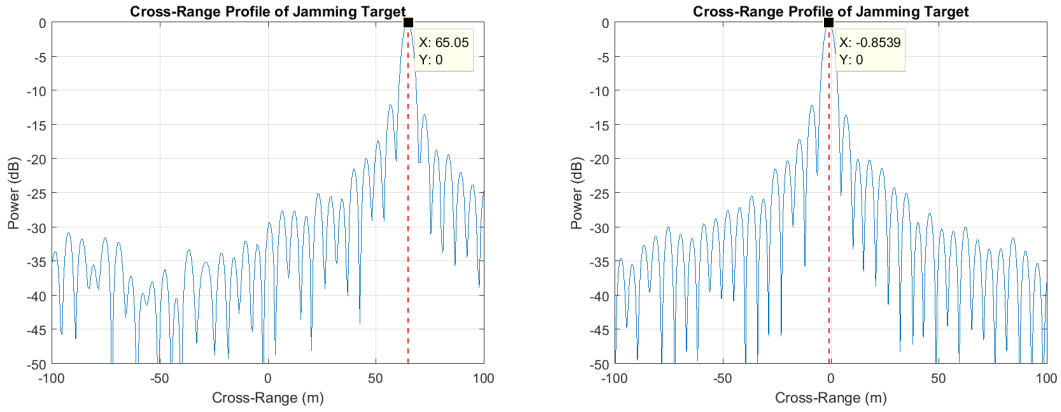

$x_\varepsilon = 0.8$ $x_\varepsilon = 4$

Figure 6.5: Cross-Range Position of False Target with Erroneous Initial Seeker Cross-Range Estimation

Figure 6.6 shows the resultant cross-range position of the false target when R_ε is 0.8 and 2.0.

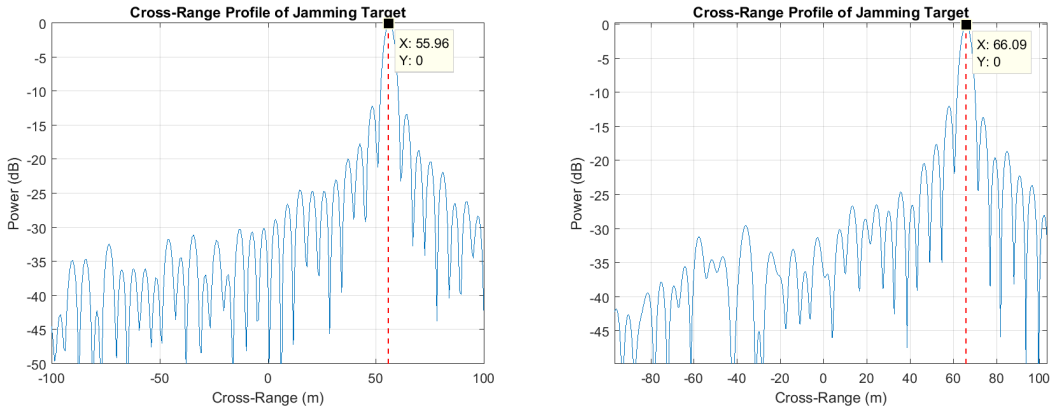

$R_\varepsilon = 0.8$ $R_\varepsilon = 2$

Figure 6.6: Cross-Range Position of False Target with Erroneous Initial Seeker Downrange Estimation

Figure 6.7 shows the resultant cross-range position of the false target when V_ε is 0.8 and 2.0.

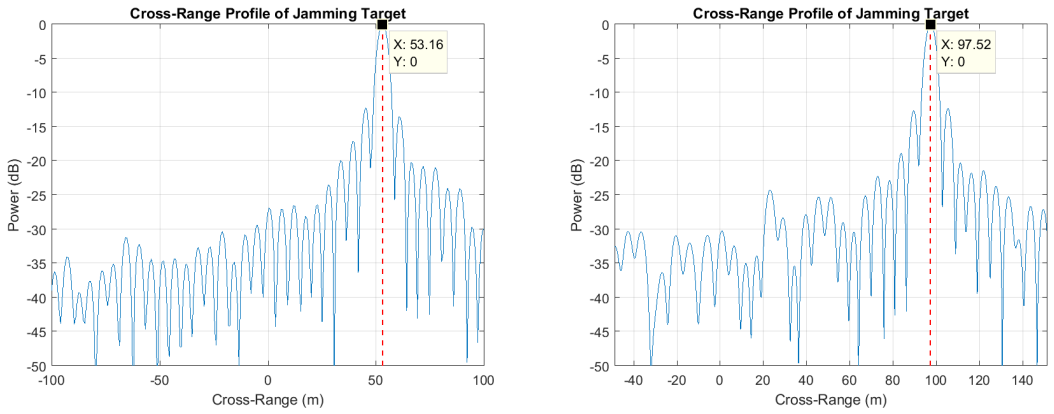

$V_\varepsilon = 0.8$ $V_\varepsilon = 2$

Figure 6.7: Cross-Range Position of False Target with Erroneous Initial Seeker Velocity Estimation

Figures 6.5, 6.7 and 6.6 show that the predictions in Figure 6.3 can be used to predict the resultant position of the false target in cross-range for the corresponding error scalars (x_ε, R_ε and V_ε).

6.3 Initial Phase of Jammer

From a DBS perspective, the intial phase of the jammer response will not effect the false target. From Eq. (6.18), if the jammer adds a Doppler shift with α and has an initial phase offset of ϕ, then the final result at the seeker would be

$$s_R(t) = \hat{\gamma}_R s\left(t - \frac{2R_0}{c} - \tau_j\right) \exp\left(-i2\pi f_c \frac{2\beta}{c} t\right) \exp\left(i2\pi f_c \alpha t + \phi\right) \tag{6.18}$$

Providing that the initial phase was not time varying, this will not affect the false target result at the seeker. Using the same co-ordinates as those in Figure 6.1 (V = 270 m/s, R_0 = 14 km, x_0 = 0.5 km, δ_R = 200 m and δ_x = 300 m) and the signal variables detailed in Table 6.2, a simulation was carried out to verify this. In the simulation, the value of ϕ was

nominally $\frac{\pi}{2}$ so that

$$s_R(t) = \hat{\gamma}_R\, s\left(t - \frac{2R_0}{c} - \tau_j\right) \exp\left(-i2\pi f_c \frac{2\beta}{c} t\right) \exp\left(i2\pi f_c \alpha t + \frac{\pi}{2}\right) \tag{6.19}$$

The results shown in Figure 6.8 show that the jamming target is exactly as intended and with clean profiles. This demonstrates that for DBS, the initial phase of the jamming Doppler shift will not affect the false target, providing that the phase offset is not time varying.

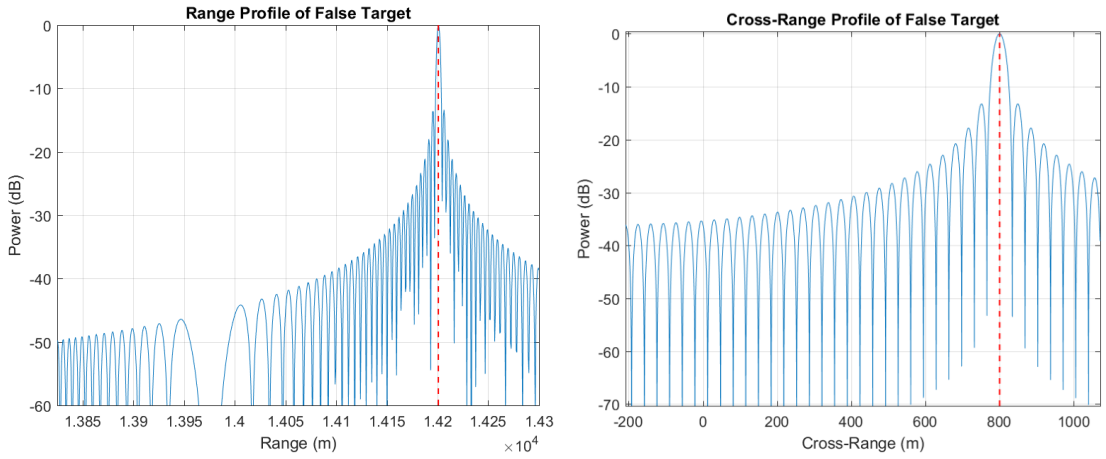

Figure 6.8: Range and Cross-Range Profiles of Target with Initial Jammer Phase Offset of $\frac{\pi}{2}$

6.4 Conclusion

The experimental results show that the jamming techniques detailed in Chapter 5 can be successful at creating a false target at a specific location. Without the presence of jamming, the theoretical errors of the tracking radar would result in small errors in the position of the false target. However, these errors could increase and become significant should the tracking performance be degraded with jamming or evasion manoeuvres which the missile might perform to evade detection or tracking. The tracking radar errors can also be increased when a salvo of missiles is fired, saturating the tracker or by co-operative or 'smart' missiles collaborating in a way to make it harder to identify and track them. This will be discussed further in the next chapter.

The expected trajectories for the missile will generally be such that $R_0 >> x_0$ and as the cross-range component of the trajectory will be small, relative to the down-range component, errors in cross-range position yield smaller errors than for down-range errors. The largest source of error in the false target position is that of the velocity parameter. As a general result, the experimental and simulated results therefore show it would be better to concentrate resources on estimating the velocity rather than down-range or cross-range parameters of the incoming missile.

The purpose of jamming a missile or tracking radar is to avoid being hit by the missile or tracked by the enemy. Therefore, it is likely to be more desirable to have a false target at a location further away than intended, than closer, to avoid being hit. Using this principle, it is better to underestimate the cross-range and down-range variables and overestimate the velocity magnitude variable. This is a general result, which will hold when $R_0 >> x_0$.

Chapter 7

General Conclusion and Future Work

7.1 General Conclusion

Chapter 4 of this thesis presented a low-cost experimental setup, capable of taking DBS images of stationary targets. The DBS images of a stationary target show DBS theory in action and how DBS can be used to resolve targets where a real beam cannot, by creating an aperture across the target being imaged. The overall result of the DBS system is that it can be used to test jamming schemes and waveforms to further understand and verify results obtained from simulations.

Chapter 5 presented two implementation methods to create false targets in the DBS image of a missile seeker. The first method was to repeat the waveforms of the seeker with an incremental time delay. This was tested with simulations and shown to be effective in principle. The problem with this method, is that it requires incredibly precise timings (in the order of picoseconds) and is therefore difficult to realise in practice.

Building upon the first method, the second method repeats the waveforms of the seeker with a constant time delay and a Doppler shift, to create the false target. This technique will be easier to realise in practice against narrowband radars. The experimental results show that the second technique can place false targets at precise locations, if the trajectory of the missile is known. The derived theory shows that the Doppler shift the jammer ap-

plies to the waveform of the seeker is dependant on three properties, velocity, cross-range and down-range. All of these parameters can be incorrectly estimated and will affect the position of the false targets in varying amounts.

The experimental results show that the jamming techniques detailed in Chapter 5 can be successful at creating a false target at a specific location. Without the presence of jamming, the theoretical errors a tracking radar would have result in small errors in the position of the false target. However, these errors could increase and become significant should the tracking performance be degraded with jamming or evasion manoeuvres which the missile might perform to evade detection or tracking. The tracking radar errors can also be increased when a salvo of missiles is fired, saturating the tracker or by co-operative or 'smart' missiles collaborating in a way to make it harder to identify and track them.

The expected trajectories for the missile will generally be such that $R_0 >> x_0$ and as the cross-range component of the trajectory will be small, relative to the down-range component, errors in cross-range position yield smaller errors than for down-range errors. The largest source of error in the false target position is that of the velocity parameter. As a general result, the experimental and simulated results therefore show it would be better to concentrate resources on estimating the velocity rather than down-range or cross-range parameters of the incoming missile.

The purpose of jamming a missile or tracking radar is to avoid being hit by the missile or tracked by the enemy. Therefore, it is likely to be more desirable to have a false target at a location further away than intended, than closer, to avoid being hit. Using this principle, it is better to underestimate the cross-range and down-range variables and overestimate the velocity magnitude variable. This is a general result, which will hold when $R_0 >> x_0$.

7.2 Summary of Contributions

This section is used to detail the main contributions presented in this thesis in a concise form. The main contributions are:

CH. 4 - Experimental Setup: Construction of a system capable of taking DBS images and demonstrating jamming techniques against DBS. This chapter formed part of the novel contributions of this thesis, as it was main experimental setup for the results obtained in Chapters 5 and 6.

CH. 5 - Inserting False Targets into a DBS Image: Two methods of implementation to insert false targets into DBS images are presented in this chapter. The first method proposes repeat jamming with a time-varying delay, the second details how to create false targets at a precise location within a seeker DBS image, by both delaying and adding a Doppler shift to received waveforms. The first method is tested with simulations and the second was tested with both simulations and measurements with the DBS system detailed in Chapter 4.

CH. 6 - Effects of Errors in Trajectory Estimation: Chapter 5 details the required parameters about the seeker trajectory to insert a false target into the seeker DBS image. This chapter describes the effects of tracking errors on the position of the false target. This is analysed analytically, with simulations and with experimental results. The results are used to assess the practical implementation of the second jamming scheme.

7.3 Future Work

7.3.1 'Chopping'

This thesis presented jamming against a DBS system which was using LFM waveforms. The jamming scheme repeats the entire waveform back towards the seeker with a modification. Using this method against a radar that is not using waveform agility or PRI jitter is feasible, since the DRFM can take a copy of the the victim seeker waveform, store for modification and resample periodically at set intervals. This also overcomes the problem of range because the jammer can transmit the jamming waveform at any time during the victim seeker PRI and not just when it receives the waveform of the seeker. For example, if a DRFM samples an entire pulse of 10 μs, that corresponds to a delayed range of approximately 1.5 km.

A method to overcome this problem is to sample only a portion of the received waveform, instead of the whole pulse. This method is also known as 'chopping', as detailed in [Abu El-Fadl et al., 2014]. Against an LFM waveform, this will result in waveform of a shorter pulse, with a lower bandwidth than the original waveform. When the seeker receives the shorter waveform, there will still be a correlation with the transmitted waveform as it is partially matched to it. This will result in a false target with a larger range resolution (due to the lower bandwidth) and will result in the false target being closer to the victim seeker than the jammer actually is, due to the mis-matched correlation. The second method of implementation detailed in Chapter 5 should be developed further and used with the 'chopping' method.

7.3.2 Detection of DBS

In order for the jammer to jam a seeker using the DBS mode, it needs to detect that it is using DBS and not a different type of mode. It is difficult to differentiate DBS from another type of mode from the waveform alone. For example, if the jammer receives an LFM waveform, there are many modes the seeker couild be using such as DBS, SAR, pulse-Doppler, etc. However, in order to perform DBS or SAR, there needs to be an offset angle between the target and the seeker. This means that the missile cannot be heading directly towards the target being imaged but instead must fly at an offset and turn head onto the target at a later time, once the target has been acquired.

As stated in the literature in Chapter 2, there is some unclassified research into optimising trajectories for DBS. It is thought that the simplest way to identify the use of the DBS mode is through the trajectory of the seeker. Further research could study typical trajectories of missiles using conventional monopulse radar seekers, infrared seekers and DBS or SAR seekers and develop algorithms to discriminate between the different modes and obtain confidence levels to be more certain as to which type of countermeasure should be used.

7.3.3 Low-Cost DRFM

The use of DRFMs throughout this thesis has been assumed. The jamming techniques described in Chapter 5 require the ability to create high fidelity copies of the waveform of the victim radar, which would be achieved through the use of a DRFM system. Testing the jamming with a DRFM will bring additional complexities to the experimental setup such as introducing waveform sampling errors, latencies and possible jittering effects.

As discussed in the literature survey in Chapter 2, there are a number of publications detailing the use of Commercial Off-The-Shelf (COTS) DRFM systems [Heagney, 2018, Zhang Peng, 2015, Min Xie et al., 2015]. Future research could aim to construct a relatively low-cost DRFM system and test the jamming schemes in real time against the

schemes derived in Chapter 5. The experiments presented in Chapter 4, 5 and 6 have all been undertaken in steps to remove the requirement to have instantaneous processing. By constructing a low-cost COTS DRFM system, more insight could be gained into jammer latency, modulations and glint, caused by hardware errors of the low-cost DRFM system.

7.3.4 False Target Credibility

The proposed jamming schemes in this thesis aim to produce false targets that would look like valid skin-returns by multiplying the seeker waveforms by the corresponding Doppler shifts that a target would have if it was at the location the jammer was trying to create. However, when trying to replicate complex targets (such as a ship) there are many more factors to include such as the sea state and glint caused by target motion, target velocities, jammer location with respect to the target it is trying to protect, jammer motion caused by sea state or gusts of wind if airborne/off-board and so forth. Future research should also seek to include realistic fluctuations caused by the factors mentioned above.

The probability of the seeker accepting or rejecting the false targets generated by the jammer is a complex subject and it would depend on the target scenes being imaged (e.g. ships on seas, tanks on ground) as well as the specific target classification algorithms employed by the missile seeker. Therefore, the research should also be continued to assess the probability of the seeker accepting or rejecting the false targets generated using the described algorithms.

7.3.5 Future Work Summary

This thesis has presented two implementation methods to create false targets in a DBS image, as well as an analysis of errors caused by incorrect tracking of the missile trajectory. The next steps to continue this work would be to first construct a low-cost DRFM system to implement the schemes in Chapter 5 as well as additional methods such as 'chopping'. The second continuation would then be to develop target classification algrorithms and test the jamming schemes with the DRFM system against these algorithms to better understand how they can be improved to maximise the probability of the seeker accepting the false targets as true target.

References

[Abu El-Fadl et al., 2014] Abu El-Fadl, A., Ahmed, F., A., M., & Asseesy, A. (2014). Simulation Study of the Effect of Chopping Jamming on LFM Pulse Compression Radar. In *The 9th International Conference on Electrical Engineering* (pp. 1–13). Cairo.

[Austin, 1995] Austin, B. (1995). Wireless in the Boer War. In *International Conference on 100 Years of Radio*, volume 1995 (pp. 44–50).: IET.

[Austin, 1999] Austin, B. A. (1999). Precursors to Radar — The Watson-Watt Memorandum and the Daventry Experiment. *International Journal of Electrical Engineering Education*, 36(4), 365–372.

[Balanis, 2015] Balanis, C. A. (2015). *Antenna theory : analysis and design*. Wiley.

[Balleri et al., 2009] Balleri, A., Woodbridge, K., Baker, C. J., & Holderied, M. W. (2009). Flower classification by bats: Radar comparisons. *IEEE Aerospace and Electronic Systems Magazine*, 24(5), 4–7.

[Barbier, 2007] Barbier, M. (2007). *D-day deception : Operation Fortitude and the Normandy invasion*. Praeger Security International.

[Bikkin, 2013] Bikkin, H. (2013). *Non-equilibrium thermodynamics and physical kinetics.* De Gruyter.

[Blake & Long, 2009a] Blake, L. V. & Long, M. W. (2009a). Antennas - Fundamentals, Design, Measurement (3rd Edition). In *Antennas - Fundamentals, Design, Measurement (3rd Edition)* (pp. 346–347). SciTech Publishing.

[Blake & Long, 2009b] Blake, L. V. & Long, M. W. (2009b). Antennas - Fundamentals, Design, Measurement (3rd Edition). In *Antennas - Fundamentals, Design, Measurement (3rd Edition)* chapter 5, (pp. 183–184). SciTech Publishing.

[Bo Lv, 2010] Bo Lv (2010). Simulation study of noise convolution jamming countering to SAR. In *2010 International Conference On Computer Design and Applications* (pp. 4–130). Qinhuangdao: IEEE.

[Bond & Robinson, 1988] Bond, C. F. & Robinson, M. (1988). The evolution of deception. *Journal of Nonverbal Behavior*, 12(4), 295–307.

[Brown, 1994] Brown, R. H. (1994). Robert Alexander Watson-Watt, the Father of Radar. *Engineering Science & Education Journal*, 3(1), 31–40.

[Connor, 1982] Connor, F. R. (1982). *Noise*. Edward Arnold.

[Corazza, 1998] Corazza, G. (1998). Marconi's history [radiocommunication]. *Proceedings of the IEEE*, 86(7), 1307–1311.

[Corcoran et al., 2010] Corcoran, A. J., Conner, W. E., & Barber, J. R. (2010). Anti-bat tiger moth sounds: Form and function. *Current Zoology*, 56(3), 358–369.

[Da-hai et al., 2007] Da-hai, D. A. I., Wu, F., Xue-song, W., & Shun-ping, X. (2007). Sar active-decoys jamming based on drfm. In *2007 IET International Conference on Radar Systems* (pp. 1–4). Edinburgh.

[Daniel et al., 2018] Daniel, L., Stove, A., Hoare, E., Phippen, D., Cherniakov, M., Mulgrew, B., & Gashinova, M. (2018). Application of Doppler beam sharpening for azimuth refinement in prospective low-THz automotive radars. *IET Radar, Sonar & Navigation*, 12(10), 1121–1130.

[De Martino, 2018] De Martino, A. (2018). *Introduction to modern EW systems*. Artech House Publishers, second edi edition.

[Department for Business, 2018] Department for Business, Energy & Industrial Strategy, U. G. (2018). Hinkley Point C. https://www.gov.uk/government/collections/hinkley-point-c.

[du Plessis, 2012] du Plessis, W. (2012). Practical Implications of Recent Cross-Eye Jamming Research. *O Simpósio de Aplicações Operacionais em Áreas de Defesa (SIGE)*, 2, 167–174.

[du Plessis, 2019] du Plessis, W. P. (2019). Statistical Skin-Return Results for Retrodirective Cross-Eye Jamming. *IEEE Transactions on Aerospace and Electronic Systems*.

[du Plessis et al., 2009] du Plessis, W. P., Odendaal, J. W., & Joubert, J. (2009). Extended analysis of retrodirective cross-eye jamming. *IEEE Transactions on Antennas and Propagation*, 57(9), 2803–2806.

[Eurofighter, 2016] Eurofighter (2016). Eurofighter Typhoon — Flights trials of E-Scan radar begin on Eurofighter Typhoon jet. https://www.eurofighter.com/news-and-events/2016/07/flights-trials-of-e-scan-radar-begin-on-eurofighter-typhoon-jet.

[Falk, 2007] Falk, L. (2007). Cross-eye jamming of monopulse radar. In *2007 International Waveform Diversity and Design Conference* (pp. 209–213). Pisa: IEEE.

[Farooq & Limebeer, 2007] Farooq, A. & Limebeer, D. J. N. (2007). Optimal trajectory tracking for missiles with Doppler Beam Sharpening radars. In *2007 European Control Conference (ECC)* (pp. 3985–3992). Kos, Greece: IEEE.

[Farooq & N. Limebeer, 2002] Farooq, A. & N. Limebeer, D. J. (2002). Trajectory Optimization for Air-to-Surface Missiles with Imaging Radars. *Journal of Guidance, Control, and Dynamics*, 25(5), 876–887.

[Flower, 2011] Flower, T. (2011). Fork-tailed drongos use deceptive mimicked alarm calls to steal food. *Proceedings. Biological sciences*, 278(1711), 1548–55.

[Frazer et al., 2017] Frazer, G., Balleri, A., & Jacob, G. (2017). Simulations of Repeat Jamming against Anti-Ship Missile Seekers Which Use Doppler Beam Sharpening Modes. In *2017 Sensor Signal Processing for Defence Conference (SSPD)* (pp. 1–5). London: IEEE.

[Frazer et al., 2020] Frazer, G., Balleri, A., & Jacob, G. (2020). Deception Jamming Against Doppler Beam Sharpening Radars. *IEEE Access*, 8, 32792–32801.

[Frazer et al., 2019] Frazer, G., Balleri, A., & Jacob, G. S. (2019). Deception Jamming Against Doppler Beam Sharpening Radars. In *2019 IEEE Radar Conference (RadarConf)* (pp. 1–6). Boston: IEEE.

[G. Pietrzyk et al., 2004] G. Pietrzyk, P. Samczynski, A. Gorzelanczyk, & K. Kulpa (2004). Real-time implementation of doppler beam sharpening technique with simple motion estimation. In *Radar Conference, 2004. EURAD. First European* (pp. 340). Amsterdam: Horizon House.

[Gebhard, 1979] Gebhard, L. A. (1979). Evolution of Naval Radio-Electronics and Contributions of the Naval Research Laboratory. Revision.

[Griffiths, 2014] Griffiths, H. (2014). The Würzburg radar equipment from the Bruneval raid. *IEEE Aerospace and Electronic Systems Magazine*, 29(4), 14–19.

[Griffiths, 2015] Griffiths, H. (2015). The D-day deception operations TAXABLE and GLIMMER. *IEEE Aerospace and Electronic Systems Magazine*, 30(3), 12–20.

[Griffiths, 2016] Griffiths, H. (2016). Early history of bistatic radar. In *2016 European Radar Conference (EuRAD)* London: IEEE.

[Griffiths, 2017] Griffiths, H. (2017). Klein Heidelberg: new information and further insight. *IET Radar, Sonar & Navigation*, 11(6), 903–908.

[Griffiths et al., 2019] Griffiths, H., Knott, P., & Koch, W. (2019). Christian Hülsmeyer: Invention and Demonstration of Radar, 1904. *IEEE Aerospace and Electronic Systems Magazine*, 34(9), 56–60.

[Harness & Budge, 2014] Harness, R. S. & Budge, M. C. (2014). A study on SAR noise jamming and false target insertion. In *IEEE SOUTHEASTCON 2014* (pp. 1–8).: IEEE.

[Haykin & Moher, 2009] Haykin, S. S. & Moher, M. (2009). *Communication systems*. Wiley.

[He et al., 2014] He, X., Zhu, J., Wang, J., Du, D., & Tang, B. (2014). False Target Deceptive Jamming for Countering Missile-Borne SAR. In *2014 IEEE 17th International Conference on Computational Science and Engineering* (pp. 1974–1978). Chengdu: IEEE.

[Heagney, 2018] Heagney, C. P. (2018). Digital radio frequency memory synthetic instrument enhancing US navy automated test equipment mission. *IEEE Instrumentation & Measurement Magazine*, 21(4), 41–63.

[Hodgson & Lee, 2003] Hodgson, J. & Lee, D. (2003). Terminal Guidance Using a Doppler Beam Sharpening Radar. In *AIAA Guidance, Navigation, and Control Conference and Exhibit* Reston, Virigina: American Institute of Aeronautics and Astronautics.

[Hong-xu et al., 2010] Hong-xu, H., Yi-yu, Z., Wen-li, J., & Zhi-tao, H. (2010). A new time-delay echo jamming style to SAR. In *2010 2nd International Conference on Signal Processing Systems* (pp. 3–14). Dalian: IEEE.

[Huang et al., 2015] Huang, L., Dong, C., Shen, Z., & Zhao, G. (2015). The influence of Rebound Jamming on SAR GMTI. *IEEE Geoscience and Remote Sensing Letters*, 12(2), 399–403.

[Institution of Civil Engineers (Great Britain), 1914] Institution of Civil Engineers (Great Britain) (1914). OBITUARY. SIR WILLIAM HENRY PREECE, KCB, FRS, 1834-1913. In *Minutes of Proceedings of the Institution of Civil Engineers Volume: 196 Issue 1914 (1914)*: ICE Publishing.

[James, 1989] James, R. (1989). A history of radar. *IEE Review*, 35(9), 343.

[Kim et al., 2011] Kim, K. H., Kim, S. G., & Yi, J. W. (2011). Detection of Ship Targets Near Coastline by Using Doppler Beam Sharpening Technique. In *2011 3rd International Asia-Pacific Conference on Synthetic Aperture Radar (APSAR)*, number 1 (pp. 774–777). Seoul: IEEE.

[Lacomme et al., 2001] Lacomme, P., Hardange, J.-P., Marchais, J.-C., & Normant, E. (2001). Chapter 15 - Synthetic Aperture Radar. In *Air and Spaceborne Radar Systems - An Introduction* (pp. 260–261). William Andrew Publishing/Noyes.

[Laribi et al., 2018] Laribi, A., Hahn, M., Dickmann, J., & Waldschmidt, C. (2018). Vertical Doppler beam sharpening goes self parking. In *2018 IEEE Radar Conference (RadarConf18)* (pp. 0383–0388). Oklahoma City: IEEE.

[LEONARDO, 2017] LEONARDO (2017). BRITECLOUD - Expendable Active Decoy Brochure.

[Liu et al., 2015] Liu, S. Y., Dong, C. X., Xu, J., Zhao, G. Q., & Zhu, Y. T. (2015). Analysis of Rotating Cross-Eye Jamming. *IEEE Antennas and Wireless Propagation Letters*, 14, 939–942.

[Lockheed Martin, 2017] Lockheed Martin (2017). Nulka Anti-Ship Missile Self Defense System Brochure.

[Marincic & Budimir, 2008] Marincic, A. & Budimir, D. (2008). Tesla's multi-frequency wireless radio controlled vessel. In *2008 IEEE History of Telecommunications Conference* (pp. 24–27). Paris: IEEE.

[Martin, 1988] Martin, D. (1988). Radar 1935–45: ten years that changed the face of war. *Journal of the Institution of Electronic and Radio Engineers*, 58(2), 67.

[MBDA, 2018] MBDA (2018). PRESS RELEASE: MBDA's Sea Venom-ANL missile marks further trials milestone.

[Min Xie et al., 2015] Min Xie, M. X., Jiazhi Huang, J. H., Yuansong Jiang, Y. J., & Xiongjun Fu, X. F. (2015). Design and realization of DRFM system based on FPGA and DSP. In *IET International Radar Conference 2015*: Institution of Engineering and Technology.

[Mitchell & Thompson, 1986] Mitchell, R. W. & Thompson, N. S. (1986). *Deception, perspectives on human and nonhuman deceit*. SUNY series in animal behavior. State University of New York Press.

[Navy, 2017] Navy, R. (2017). Type 45 Destroyer — Royal Navy.

[Neri, 2001a] Neri, F. (2001a). Anti-monopulse jamming techniques. In *Proceedings of the 2001 SBMO/IEEE MTT-S International Microwave and Optoelectronics Conference. (Cat. No.01TH8568)*, volume 2 (pp. 45–50). Belem, Brazil: IEEE.

[Neri, 2001b] Neri, F. (2001b). *Introduction to electronic defense systems*. London Artech House, 2nd edition.

[Neri, 2006] Neri, F. (2006). SAR Performances. In *Introduction to Electronic Defense Systems (2nd Edition)* chapter 2, (pp. 134 – 136). SciTech Publishing.

[Newcombe & Balleri, 2014] Newcombe, C. & Balleri, A. (2014). Simulations of Waveform Diversity for Doppler Beam Sharpening techniques. In *2014 International Radar Conference, Radar 2014* Lille: IEEE.

[Northrop Grumman Corporation, 2018] Northrop Grumman Corporation (2018). Northrop Grumman Receives $3.6 Billion IDIQ Contract for Infrared Countermeasures Systems.

[Nyquist, 1928] Nyquist, H. (1928). Thermal Agitation of Electric Charge in Conductors. *Physical Review*, 32(1), 110–113.

[Paik et al., 2014] Paik, H., Sastry, N., & SantiPrabha, I. (2014). Effectiveness of noise jamming with White Gaussian Noise and phase noise in amplitude comparison monopulse radar receivers. In *2014 IEEE International Conference on Electronics, Computing and Communication Technologies (CONECCT)* Bangalore: IEEE.

[Paik et al., 2015] Paik, H., Sastry, N., & SantiPrabha, I. (2015). Effectiveness of Repeat Jamming using Linear FM Interference Signal in Monopulse receivers. *3rd International Conference on Recent Trends in Computing 2015 (ICRTC-2015)*, 57, 296–304.

[Paik et al., 2016] Paik, H., Sastry, N., & SantiPrabha, I. (2016). Estimation of break-lock in PLL synthesizers for monopulse radar applications: Experimental and simulation approach. *Engineering Science and Technology, an International Journal*, 19(1), 22–30.

[Pan et al., 2014] Pan, X., Wang, W., Feng, D., Liu, Y., Fu, Q., & Wang, G. (2014). On deception jamming for countering bistatic ISAR based on sub-Nyquist sampling. *IET Radar, Sonar and Navigation*, 8(3), 173–179.

[Piccirillo, 1997] Piccirillo, A. (1997). The origins of the anti-ship guided missile. In *1997 World Aviation Congress* Reston, Virigina: American Institute of Aeronautics and Astronautics.

[R. Schroer, 2003] R. Schroer (2003). Electronic warfare. [A century of powered flight: 1903-2003]. *IEEE AES Systems Magazine*.

[Rollason et al., 2003] Rollason, M., Salmond, D., & Evans, M. (2003). Parameter Estimation for Terminal Guidance Using a Doppler Beam Sharpening Radar. In *AIAA Guidance, Navigation, and Control Conference and Exhibit* Austin, Texas: American Institute of Aeronautics and Astronautics.

[Royal Air Force, 2019] Royal Air Force (2019). Typhoon FGR4 - Royal Air Force. https://www.raf.mod.uk/aircraft/typhoon-fgr4/.

[Saxon, 2003] Saxon, T. (2003). Kehl : The German use of guided weapons against naval targets 1943–44. *Defence Studies*, 3(1), 1–16.

[Skolnik, 2001] Skolnik, M. I. M. I. (2001). *Introduction to radar systems*. McGraw Hill, 3rd ed. edition.

[Skolnik, 2008] Skolnik, M. I. M. I. (2008). *Radar Handbook*. McGraw-Hill Education, 3rd ed. edition.

[Soumekh, 2006] Soumekh, M. (2006). SAR-ECCM using phase-perturbed LFM chirp signals and DRFM repeat jammer penalization. *IEEE Transactions on Aerospace and Electronic Systems*, 42(1), 191–205.

[Stansfield, 2016] Stansfield, N. (2016). A Missile Seeker and Guidance Method.

[Stimson, 1998] Stimson (1998). *Introduction to Airborne Radar*. Institution of Engineering and Technology.

[Stimson et al., 2014] Stimson, G. W., Griffiths, H. H., Baker, C., & Adamy, D. (2014). *Stimson's Introduction to Airborne Radar*. SciTech Publishing, 3rd ed. edition.

[Sun et al., 2014] Sun, Q., Shu, T., Zhou, S., Tang, B., & Yu, W. (2014). A novel jamming signal generation method for deceptive SAR jammer. In *2014 IEEE Radar Conference* (pp. 1174–1178). Cincinnati: IEEE.

[Sunzi & Clavell, 1981] Sunzi, a. t. c. B. & Clavell, J. (1981). *The art of war*. Hodder and Stoughton.

[Swords, 1986] Swords, S. S. (1986). *Technical history of the beginnings of radar*. P. Peregrinus on behalf of the Institution of Electrical Engineers.

[Van Trees, 2001] Van Trees, H. L. (2001). Detection, Estimation, and Modulation Theory, Part III. In *Detection, Estimation, and Modulation Theory, Part III* (pp. 241). New York, USA: John Wiley & Sons, Inc.

[Wang & Cai, 2007] Wang, W. & Cai, J. (2007). A Technique for Jamming Bi- and Multistatic SAR Systems. *IEEE Geoscience and Remote Sensing Letters*, 4(1), 80–82.

[Wang et al., 2014] Wang, W., Pan, X. Y., Liu, Y. C., Feng, D. J., & Fu, Q. X. (2014). Sub-Nyquist sampling jamming against ISAR with compressive sensing. *IEEE Sensors Journal*, 14(9), 3131–3136.

[Wei et al., 2016] Wei, L., Xiaopeng, Y., Chao, Z., Shuai, L., & Liyue, N. (2016). DRFM range false target cancellation method based on slope-varying LFM chirp signal. In *2016 IEEE 13th International Conference on Signal Processing (ICSP)* (pp. 1629–1632). Chengdu: IEEE.

[Wiley, 1985] Wiley, C. (1985). Synthetic Aperture Radars. *IEEE Transactions on Aerospace and Electronic Systems*, AES-21(3), 440–443.

[Xilinx, 2019] Xilinx (2019). Xilinx Virtex-7 FPGA VC707 Evaluation Kit. https://www.xilinx.com/products/boards-and-kits/ek-v7-vc707-g.html#documentation.

[Zhang Peng, 2015] Zhang Peng, Z. P. (2015). Realization of DRFM radar target simulator based on general instruments. In *IET International Radar Conference 2015*, volume 2015: Institution of Engineering and Technology.

[Zheng Shenghua, 2004] Zheng Shenghua, X. D. (2004). A study on active jamming to synthetic aperture radar. In *Proceedings. ICCEA 2004. 2004 3rd International Conference on Computational Electromagnetics and Its Applications, 2004.* (pp. 403–406). Beijing: IEEE.

Appendix A

Rail Accuracy Verification

1 - LEFT CW - mm

	1	2	3	4	5
1	2.86	3.29	2.97	3.26	3.07
2	3.01	3.09	3.16	3.01	3.28
3	3.16	3.10	2.91	2.88	3.12
4	3.06	3.14	3.06	2.91	3.09
5	3.14	2.92	3.17	2.92	3.20
6	3.16	3.14	3.11	3.20	2.95

2 - MIDDLE CW- mm

	1	2	3	4	5
1	2.62	3.13	3.03	3.14	3.08
2	3.18	3.19	3.07	3.20	3.23
3	3.11	2.98	3.20	3.05	2.99
4	3.17	3.33	3.08	3.23	3.16
5	3.17	2.98	3.18	3.12	3.12
6	3.13	3.28	3.11	3.21	3.11

3 - RIGHT CW- mm

	1	2	3	4	5
1	2.90	2.93	3.14	3.06	3.04
2	2.83	2.94	3.18	3.17	3.23
3	2.86	3.03	2.99	3.18	3.00
4	2.64	3.16	3.31	3.10	3.27
5	2.95	3.14	3.01	3.15	3.13
6	2.94	3.14	3.25	3.22	3.18

4 - LEFT CCW- mm

	1	2	3	4	5
1	2.78	3.10	3.09	3.27	3.02
2	3.07	3.21	3.17	3.00	3.23
3	3.14	2.99	3.21	3.15	3.12
4	3.05	2.92	2.89	3.09	2.72
5	3.13	3.08	3.20	3.01	3.23
6	3.08	3.27	3.18	3.18	2.81

5 - MIDDLE CCW- mm

	1	2	3	4	5
1	3.06	3.08	3.18	3.24	3.11
2	2.98	2.89	3.02	3.11	3.19
3	3.16	3.06	3.25	3.27	3.12
4	3.03	3.09	2.96	3.03	3.01
5	3.04	3.27	2.95	3.08	3.26
6	3.09	3.14	3.18	2.98	3.15

6 - RIGHT CCW- mm

	1	2	3	4	5
1	2.99	2.81	2.88	3.06	3.01
2	3.02	2.81	3.15	3.17	3.02
3	3.06	2.70	3.16	3.20	3.12
4	3.01	3.18	3.12	3.14	3.32
5	2.99	2.97	3.09	2.94	3.06
6	3.07	3.22	3.27	2.94	3.08

Figure A.1: Movement Values for Each Pulse

Appendix B

Cross-Range Errors - Simulated Results

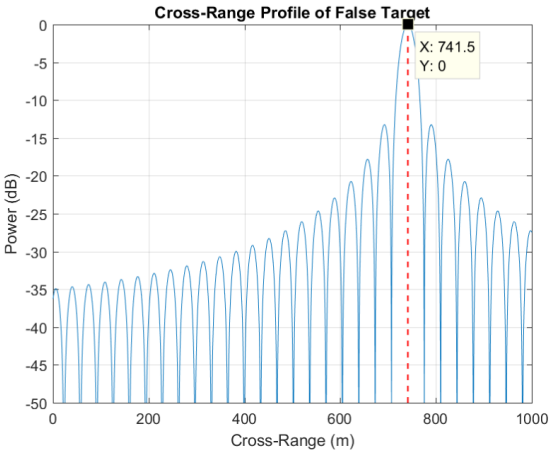

Figure B.1: $V_\varepsilon = 0.8$

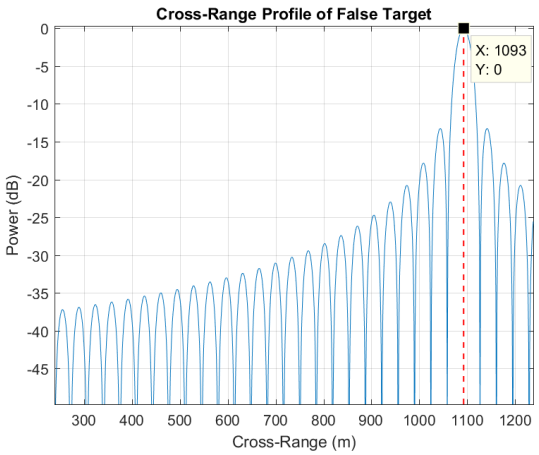

Figure B.2: $V_\varepsilon = 2$

Resultant Cross-Range Positions with Varying Velocity Error

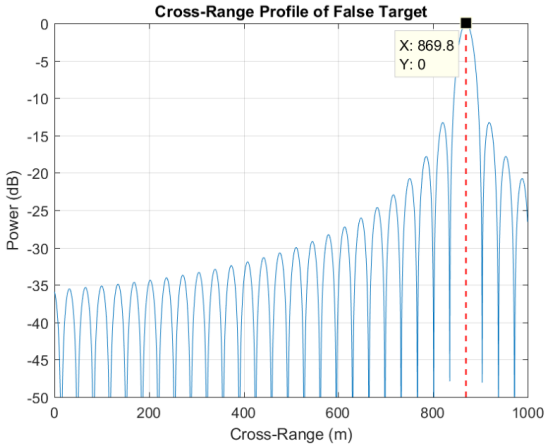

Figure B.3: $R_{d\varepsilon} = 0.8$

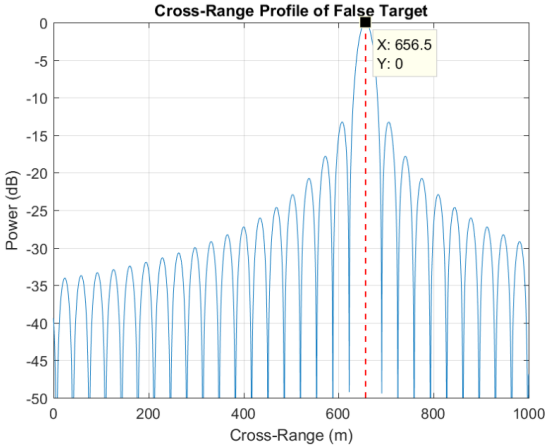

Figure B.4: $R_{d\varepsilon} = 2$

Resultant Cross-Range Positions with Varying Down-Range Error

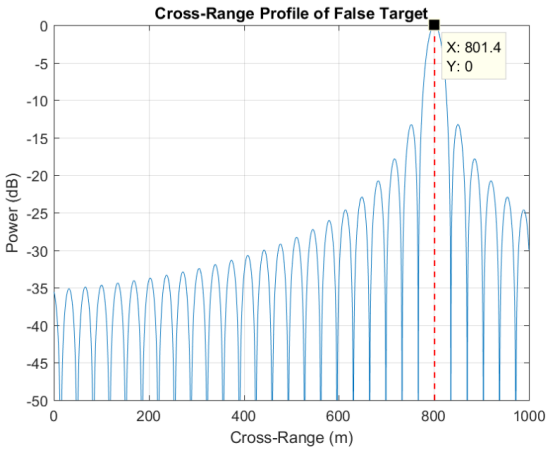

Figure B.5: $x_{0\varepsilon} = 0.8$

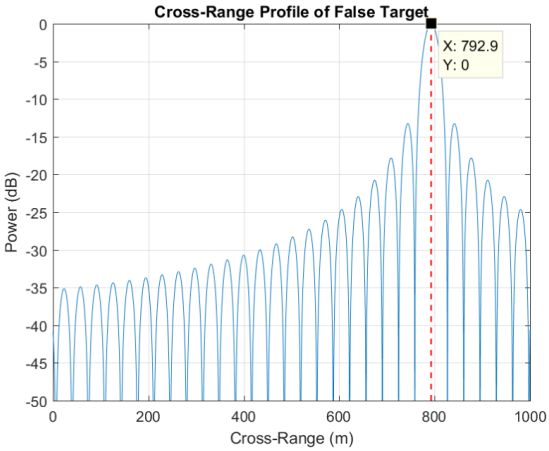

Figure B.6: $x_{0\varepsilon} = 2$

Resultant Cross-Range Positions with Varying Cross-Range Error